

**2D KINETIC STUDY OF PD-1 INTERACTION AND ITS
INHIBITION OF T-CELL ANTIGEN RECOGNITION**

A Dissertation
Presented to
The Academic Faculty

by

Kaitao Li

In Partial Fulfillment
of the Requirements for the Degree
Doctor of Philosophy in the
School of Biomedical Engineering

Georgia Institute of Technology
August of 2016

COPYRIGHT 2016 BY KAITAO LI

**2D KINETIC STUDY OF PD-1 INTERACTION AND ITS
INHIBITION OF T-CELL ANTIGEN RECOGNITION**

Approved by:

Dr. Cheng Zhu, Advisor
Department of Biomedical Engineering
Georgia Institute of Technology

Dr. Melissa L. Kemp
Department of Biomedical Engineering
Georgia Institute of Technology

Dr. Simon J. Davis
Weatherall Institute of Molecular Medicine
The University of Oxford

Dr. Susan Thomas
Department of Mechanical Engineering
Georgia Institute of Technology

Dr. Arash Grakoui
Emory vaccine center
Emory University

Date Approved: July 11, 2016

ACKNOWLEDGEMENTS

This is the most difficult part of my thesis writing. Because there are so many people I am grateful over these years, and because it's always a mix of feelings to have those wonderful memories flying through my mind again and again, and because their meaning to me are far beyond what I could concisely express here.

I would like fist of all to express my deepest gratitude to my advisor, Dr. Cheng Zhu, for his guidance, inspiration, support, and most importantly his dedication to science – all greatly influenced and shaped me into who I am today. Sincere thanks also go to my committee members Drs. Simon Davis, Arash Grakoui, Melissa Kemp, and Susan Thomas for their support and helpful suggestions of my thesis work.

Special thanks to my collaborators, Drs. Simon Davis, Xiaoxiao Cheng, Rafi Ahmed, Eunseon Ahn, Matthew Torres, Arash Grakoui, and Chris Ibegbu. Their generous support and helpful suggestions made this thesis possible. Learning from them also proves to be an invaluable part of my training.

I thank all Zhu lab members, from the “old pals” to the “new blood”. All of you have been my teachers. Your merits make it such a wonderful environment for working together. I specially thank Ms. Larissa Doudy. She had been a wonderful lab manager and always ready to help.

I also want to thank the IBB and EBB core facilities, the BME academic office, and the NIH tetramer core facility.

Finally, I would like to thank my family for all their love, support, and constant encouragement over the years.

TABLE OF CONTENTS

	Page
ACKNOWLEDGEMENTS	iv
LIST OF TABLES	vii
LIST OF FIGURES	viii
LIST OF SYMBOLS AND ABBREVIATIONS	x
SUMMARY	xiii
 <u>CHAPTER</u>	
1 INTRODUCTION	1
2 BACKGROUND	4
2.1 T cell receptor and CD8	4
2.2 Programmed death-1	6
2.3 CD222	12
3 METATERIALS AND METHODS	15
3.1 Cells	15
3.2 Proteins, antibodies, and chemicals	16
3.3 Flow cytometry and fluorescent imaging	18
3.4 2D and 3D kinetic assays	20
3.5 Biochemical assays	25
3.6 Statistical analysis	28
4 2D KINETIC ANALYSIS OF PD-1, PD-LIGANDS, AND B7-1 INTERACTIONS	29
4.1 Introduction	29
4.2 Results	30

4.3 Discussion	37
5 PD-1 SUPPRESSES T-CELL ANTIGEN RECOGNITION BY DISRUPTING THE TCR-CD8 COOPERATIVE BINDING TO COGNATE PMHC	41
5.1 Introduction	41
5.2 Results	43
5.3 Discussion	54
6 IDENTIFICATION OF CD222 AS A NOVEL BINDING PARTNER FOR HUMAN PD-L1	58
6.1 Introduction	58
6.2 Results	59
6.3 Discussion	77
7 CONCLUSIONS AND FUTURE DIRECTIONS	82
7.1 Conclusion	82
7.2 In the near future	83
7.3 In the far future	85
REFERENCES	87

LIST OF TABLES

	Page
Table 4.1: Summary of 2D kinetic parameters.	36

LIST OF FIGURES

	Page
Figure 2.1: Mechanisms of PD-1 inhibition of TCR signaling and T cell effector functions.	9
Figure 3.1: 2D kinetic analysis using adhesion frequency assay.	22
Figure 3.2: Force-clamp assay using biomembrane force probe.	22
Figure 4.1: Comparison of 2D and 3D kinetics of human PD-1 ligand interactions.	31
Figure 4.2: Comparison of 2D and 3D kinetics of murine PD-1 ligand interactions.	32
Figure 4.3: Comparison of 2D and 3D kinetics of human and murine B7-1–PD-L1 interactions.	34
Figure 4.4: Comparison of 2D and 3D kinetics of human B7-1–CD28 and B7-1–CTLA-4 interactions.	35
Figure 4.5: Comparison of 3D and 2D affinities reveals differential enhancement of 2D affinities by the cellular environment.	40
Figure 5.1: 2D kinetic analysis reveals reduced bond number with the co-engagement of TCR–CD8 and PD-1 in the OT-I/OVA system	44
Figure 5.2: 2D kinetic analysis reveals reduced bond number with the co-engagement of TCR–CD8 and PD-1 in the P14/gp33 system	45
Figure 5.3: The TCR–CD8 and PD-1 negative cooperativity depends on PD-1.	46
Figure 5.4: The TCR–CD8 and PD-1 negative cooperativity is mediated by SHP-2 not SHP-1.	47
Figure 5.5: TCR–CD8 binding to pMHC and PD-1 binding to PD-L1 were not affected by SHP-1 or SHP-2 inhibition.	48
Figure 5.6: The TCR–CD8 and PD-1 negative cooperativity depends on Lck activity.	49
Figure 5.7: The negative cooperativity is eliminated when CD8–pMHC interaction is abolished.	50
Figure 5.8: Force spectroscopy reveals distinct force-lifetime responses of TCR–pMHC, TCR–CD8–pMHC and PD-1–PD-L1 bonds of the P14/gp33 system.	51

Figure 5.9: The average bond lifetime is reduced when PD-L1 is co-engaged with WT H2-Db:gp33 not the α 3A2 mutant.	52
Figure 6.1: Specific binding between hPD-L1 and Jurkat cells is independent of PD-1 or B7-1.	59
Figure 6.2: hPD-L1 tetramer positively stains Jurkat, THP-1, but not Raji B cells.	60
Figure 6.3: hPD-L1 tetramer staining does not depend on fluorophore.	61
Figure 6.4 The effect of temperature on hPD-L1 tetramer staining.	61
Figure 6.5: hPD-L1 tetramer positively stains CD14 ⁺ cells in human peripheral blood.	62
Figure 6.6 Pulldown from Jurkat membrane lysate using hPD-L1/hPD-L2 coupled SA beads.	63
Figure 6.7: Mass spectrometry analysis identified CD222 as a tentative binding partner for hPD-L1.	64
Figure 6.8: CD222 surface expression correlates with hPD-L1 tetramer staining.	65
Figure 6.9: hPD-L1 tetramer staining was blocked by recombinant CD222 D1-9.	66
Figure 6.10: hPD-L1 binds to CD222-GFP transfected CHO cells.	66
Figure 6.11: 3D and 2D kinetics of hPD-L1–CD222 interaction.	67
Figure 6.12 Binding site mapping with anti-PD-L1 monoclonal antibodies.	68
Figure 6.13 Competitive binding of CD222 and PD-1 to hPD-L1.	69
Figure 6.14: hPD-L1 binding to CD222 is largely influenced by its N-glycans.	70
Figure 6.15: Dual binding site model for hPD-L1-CD222 interaction.	72
Figure 6.16: Screening of anti-CD222 monoclonal antibodies.	73
Figure 6.17: Effect of NaM6P on hPD-L1 and MEM-138 binding to CD222.	73
Figure 6.18: Expression of CD222 on activated T cell surface.	75
Figure 6.19: hPD-L1-CD222 failed to modulate ERK phosphorylation in Jurkat E6.1 cells.	76

LIST OF SYMBOLS AND ABBREVIATIONS

2D	Two Dimensional
3D	Three Dimensional
AA	Amino Acid
ABC	Ammonium Bicarbonate
Ac	Contact Area
A_cK_a	Effective 2D affinity
A_cK_{on}	2D on-rate
BCR	B Cell Receptor
CD-MPR	Cation-Dependent Mannose 6-Phosphate Receptor
CHO	Chinese Hamster Ovary
CI-MPR	Cation-Independent Mannose 6-Phosphate Receptor
CTLA-4	Cytotoxic T-Lymphocyte-Associated Protein 4
ERK	Extracellular Signal-Regulated Kinase
GM-CSF	Granulocyte Macrophage Colony-Stimulating Factor
HFE	Human Hemochromatosis Protein
ICAM-1	Intercellular Adhesion Molecule 1
IFN- γ	Interferon γ
IgC	Immunoglobulin Domain C-Set
IGF1R	Insulin-Like Growth Factor-I Receptor
IGF2R	Insulin-Like Growth Factor-II Receptor
IGF-I	Insulin-Like Growth Factor-I
IgV	Immunoglobulin Domain V-Set
IL-3	Interleukin 3

IL-4	Interleukin 4
ITAM	Immunoreceptor Tyrosine-Based Activation Motif
ITIM	Immunoreceptor Tyrosine-Based Inhibitory Motif
ITSM	Immunoreceptor Tyrosine-Based Switch Motif
k_{off}	off-rate
Lck	Lymphocyte-Specific Protein Tyrosine Kinase
LFA-1	Lymphocyte Function-Associated Antigen 1
LIF	Leukemia Inhibitory Factor
LmOVA	Listeria monocytogenes expressing OVA
LPS	Lipopolysaccharide
M6P	Mannose-6 Phosphate
MEK	Mitogen-Activated Protein Kinase Kinase
m_l	Receptor density
m_r	Ligand density
$\langle n \rangle$	Average number of bonds per contact
NK	Natural Killer
NKT	Natural Killer T
P_a	Probability of adhesion
PBMC	Peripheral Blood Mononuclear Cell
PD-1	Programmed Death-1
PD-L1	PD-1 Ligand-1
PD-L2	PD-1 Ligand-2
PI3K	Phosphatidylinositol-4,5-bisphosphate 3-Kinase
PLC γ 1	Phospholipase C, γ 1
(p)MHC	(peptide) Major Histocompatibility Complex

PSGL-1	P-Selectin Glycoprotein Ligand-1
PTEN	Phosphatase And Tensin Homolog
RA	Retinoic Acid
RGMb	Repulsive Guidance Molecule b
SA	Streptavidin
SHP-1	Src Homology region 2 domain-containing Phosphatase-1
SHP-2	Src Homology region 2 domain-containing Phosphatase-2
SPR	Surface Plasma Resonance
$\langle t \rangle$	Average bond lifetime
t_c	Contact duration
TCR	T Cell Receptor
TGF- β 1	Transforming Growth Factor β 1
TGN	<i>Trans</i> -Golgi Network
uPAR	Urokinase receptor
ZAP-70	Zeta-chain-Associated Protein kinase 70

SUMMARY

Programmed death-1 (PD-1) is an immune-checkpoint receptor with its primary function to maintain peripheral tolerance of the adaptive immune responses. The importance of PD-1 is evidenced by its deficiency leading to autoimmune disorders, its central role in the identification and restoration of the exhausted phenotypes of antigen-specific T cells, and the great success in targeting this pathway for cancer immunotherapy. To better understand the fundamental question as how PD-1 achieves the potent but well-controlled inhibition, we applied kinetic approaches focusing on its *in situ* ligand binding characteristics, and the early impact on antigen recognition by the T cell receptor (TCR) and coreceptor CD8. Different from the weak three-dimensional (3D) affinities measured in solution using purified PD-1 and ligands, the two-dimensional (2D) affinities of ligand binding to mouse and human PD-1 expressed on cell membrane span a range from middle to strong, whereas PD-L1–B7-1 binding is much weaker. Comparison of 2D and 3D affinities of PD-1 with B7-1–CD28 and B7-1–cytotoxic T-lymphocyte-associated protein 4 (CTLA-4) as well as others reveals distinct kinetic mechanisms underlying the inhibition of PD-1 and CTLA-4, and differential enhancement of *in situ* ligand binding for various receptors by the cellular environment.

By integrating the 2D kinetic analysis of PD-1 with TCR and CD8, we probed an apparent “negative cooperativity” between these two axis, manifested as reduced molecular bond number and bond lifetime when respective ligands were co-presented. Examination with force spectroscopy suggested the “negative cooperativity” to be the net outcome of suppressed “positive cooperativity” between TCR and CD8. Moreover, the dependence of

this suppression on Src homology region 2 domain-containing phosphatase-2 (SHP-2) and lymphocyte-specific protein tyrosine kinase (Lck) further identified it as a “binding-signaling-binding” feedback mechanism representing fine-tuning of antigen recognition by costimulatory/coinhibitory receptors via targeting the TCR–CD8 machinery.

In situ kinetic analysis also indicated the existence of a novel binding partner for human PD-L1, which was identified and validated to be CD222. The hPD-L1–CD222 interaction consists of both protein-protein and lectin-carbohydrate binding components, and is stronger than hPD-L1–PD-1 according to its higher 3D and 2D affinity/avidity. Most importantly, CD222 is upregulated on the plasma membrane of activated T cells and competes with PD-1 for hPD-L1, suggesting potentially significant functions on T cells at least in part by perturbing the hPD-L1–PD-1 interaction.

Overall, our results provide an in depth understanding of the *in situ* interaction and function of PD-1, and uncover a novel interaction of hPD-L1–CD222, highlighting the complexity and significance of costimulatory/coinhibitory molecules in modulating T cell responses.

CHAPTER 1

INTRODUCTION

致中和，天地位焉，万物育焉。（To cultivate centrality and harmony with thoroughness is the way to bring heaven and earth to their proper place and all things their proper nourishment [1].)

—— Confucius

“One general law, leading to the advancement of all organic beings, namely, multiply, vary, let the strongest live and the weakest die.[2]” Evolution is perhaps not simply the natural selection of the strongest, but rather a process of trying to strike a balance with confined resource of nourishment. Into this process we have stumbled and thrive, if not exactly by accident, but under the nature we think we dominate there lies the centrality everywhere, from the level of species, to individuals, and further down to organs, cells, and molecules. With this, “strong” and “weak” are nothing but the abstraction of centrality from all levels below, yet collectively constituting the centrality above. Then, along with the progression of the unreachable equilibrium driven by constitutive disruptive forces, all things evolve, and more precisely, co-evolve.

Also evolving is our understanding of such centrality itself. Reviewing the history of immunology, we have long been honoring how capable the immune system fights against pathogens, but did not come to realize until around 1950 that keeping it quiescent is equally if not more important. An understanding of the immunological balance on T lymphocytes was first attempted in a “self” vs “non-self” model following the clonal

selection theory, the discovery of MHC restriction, and the cloning of TCR genes. Centering around this model, which is still under in-depth mechanistic investigation, there added the “two-signal” elaboration for T-cell activation along with the discovery of the B7–CD28 costimulatory pathway. Then CTLA-4 as the first identified T-cell coinhibitory receptor further advanced the concept that the balance of T-cell activation does not come from passive unresponsiveness of TCR alone, but involves active suppression from co-signals as well. This understanding matured over the past two decades with the expanding list of costimulatory/coinhibitory molecules, the identification of new cell subsets and cytokines conferring regulatory roles, the signaling components involved, and most importantly, the clinical benefits from targeting these pathways as therapeutics for immune-related diseases. The coinhibitory receptor of interest to this study, PD-1, is one of the critical discoveries driving the evolution of this concept, and has also proved to be a promising target for the novel tumor immunotherapy. But much is still left to know about the fundamental mechanisms as how it contributes to achieving the desired T-cell responses at the proper time and location, with the optimal magnitude and duration.

As biomedical engineers, we attempted to tackle the unknowns from biophysical perspectives starting with depicting how ligand binding occurs for PD-1 expressed on the native cell membrane – a basic kinetic problem with more complexity and significance imposed by the cellular environment remains to be answered (Chapter 4). We then extended the *in situ* kinetic analysis to include TCR and CD8 to resolve the PD-1 coinhibition at the level of antigen recognition (Chapter 5). In Chapter 6 we will present the discovery of a novel binding partner for human PD-L1, the function of which requires

broad investigations in the future. In the end (Chapter 7), we summarize the contribution of this study and discuss the important questions to continue from this point.

CHAPTER 2

BACKGROUND

2.1 T cell receptor and CD8

2.1.1 Structure of TCR and CD8

The recognition of pathogenic antigens by T lymphocytes is central to the adaptive immune responses and is initiated by the binding of TCR with pMHC. The α/β TCR consists of two disulfide-bonded chains each containing an N-terminal IgV domain, an IgC domain, a transmembrane region, and a cytoplasmic tail at the C-terminus. There is no signaling motif in the cytoplasmic tail of either chain, but instead the signaling is mediated by its in complex with CD3 $\zeta\zeta$ homodimer and $\epsilon\delta$, $\epsilon\gamma$ heterodimers, which encode 6, 2, and 2 Immunoreceptor Tyrosine-Based Activation Motifs (ITAMs), respectively. As a result of thymocyte selection, binding between TCR and pMHC occurs in a restricted manner for peripheral T cells, with CD8⁺ T cells expressing TCRs that recognized peptide bound to class I MHC, whereas CD4⁺ T cells recognizing peptide presented by class II MHC. Antigen recognition for CD8⁺ T cells is largely mediated by the binding of TCR V α /V β loops to that of the opposing MHC $\alpha 1\alpha 2$ domains with peptide (8-9aa) bound to its peptide binding groove [3].

CD8 exists in forms of a covalent $\alpha\alpha$ homodimer or $\alpha\beta$ heterodimer with either chain containing a single IgV domain, a 40-50aa stalk and a short cytoplasmic tail that is able to associate with p56^{Lck}. CD8 interacts primarily with the $\alpha 3$ domain of MHC that is distal from the TCR–MHC interface [4]. CD8–MHC binding is thought to enhance TCR

antigen recognition at least in two ways: 1) to stabilize TCR–pMHC interaction, and 2) to bring Lck in close proximity of TCR–CD3 and thereby facilitate signaling.

2.1.2 Cooperative binding of TCR and CD8 to pMHC

The antigen-specific recognition between TCR and pMHC and the non-specific interaction between CD8 and MHC raises the question as how the three molecule coordinate to enhance the sensitivity for antigen while still being confined by the antigen specificity? Part of the answer comes from the affinity and kinetic measurements of these interactions. The 3D affinity of CD8–H2-K^b is 20-fold lower than that of OT-I TCR interacting with H2-K^b:OVA [5, 6]. An even larger difference (~3-log) was observed between CD8–H2-D^b and P14 TCR interacting with H2-D^b:gp33 [7, 8]. Such dramatic affinity differences were also confirmed by 2D kinetic analysis using naïve CD8⁺ T cells expressing native TCR and CD8 [9, 10]. This then suggests that antigen recognition is highly unlikely to be initiated by CD8, but is dominated by the TCR–pMHC engagement. In line with this model, TCR stimulation of CD8⁺ T cells was found to activate CD8 binding to class I MHC, suggesting a sequential mode of operation [11]. More detailed studies using 2D kinetic approaches confirmed the sequential binding model and demonstrated the cooperative binding of TCR and CD8 to pMHC [12, 13]. The cooperativity (tendency in forming TCR–CD8–pMHC trimolecular bond) reflects a signaling dependent binding enhancement for CD8, as it depends on the ligand engagement of TCR and was abolish by PP2, a Src family kinase inhibitor [12]. The underlying mechanism of such enhancement, although remains unclear, might be related to the TCR-triggered association of CD8 and CD3 ζ , since disruption of CD8–Lck interaction eliminated both CD8–CD3 ζ interaction and the TCR–CD8 cooperative binding [14, 15].

2.2 Programmed death-1

2.2.1 Structure and expression of PD-1 and its ligands

PD-1 (CD279) was identified by Tasuku Honjo's group in 1992 [16]. Using subtractive hybridization, they isolated murine PD-1 gene from stimulated 2B4.11 T cell hybridoma and Interleukin-3 (IL-3) deprived LyD9 hematopoietic progenitor cells that undergo apoptosis. Activation of this gene was thought to be involved in the classical type of programmed cell death, and therefore it was conferred the name "Programmed Death-1". Sequence analysis of PD-1 reveals a 50-55-kDa type I transmembrane glycoprotein consisting of an IgV domain, followed by a ~20 amino acid (AA) stalk connecting to the transmembrane domain, and the cytoplasmic tail containing two tyrosine-based signaling motifs: a N-terminal Immunoreceptor Tyrosine-Based Inhibitory Motif (ITIM) and a C-terminal Immunoreceptor Tyrosine-Based Switch Motif (ITSM) [16, 17]. The IgV domain of PD-1 shares ~23% homology to CD28 in sequence but structurally is more close to antigen receptors (TCR and BCR) and CD8 [18-21]. Expression of PD-1 was first identified in double-negative thymocytes and peripheral T and B cells upon activation [22, 23]. Later on, a broader expression profile also included Natural Killer (NK) cells, Natural Killer T (NKT) cells, monocytes, and even subpopulations of melanoma cells [24-28]. The complex and dynamic expression pattern is regulated collectively by 10 transcription factors, and on T cells the expression level is dominated by the strength of antigen stimulation [29-31]. Therefore, while transient PD-1 upregulation on antigen-specific T cells is usually associated with acute infections, cases with persistent antigen stimulations such as chronic viral infections and cancer usually induce constitutively high PD-1 expression [32, 33].

The first ligand for PD-1, PD-1 ligand 1 (PD-L1, B7-H1, CD274), was discovered independently by two groups in 1999 and 2000, both involving genetic database searches for B7 homologs [34, 35]. Like other B7 family members, there is an IgV domain and an IgC domain in the extracellular region of PD-L1, sharing ~25% identity with B7-1. The cytoplasmic tail is ~30 AA in length, with no signaling motif identified [21]. PD-L1 is expressed in both hematopoietic and non-hematopoietic cells in resting states. Depending on the cell type expressed, its expression is further upregulated generally by pro-inflammatory cues, such as antigen stimulation of T cells, and lipopolysaccharide (LPS), Interferon γ (IFN- γ), Granulocyte Macrophage Colony-Stimulating Factor (GM-CSF), or Interleukin 4 (IL-4) stimulation of macrophages [36]. Increased PD-L1 expression is also found on many types of cancer cells, which may be partially attributed to reduced expression or activity of Phosphatase And Tensin Homolog (PTEN) [24, 33, 37].

Searching for PD-L1 homologs in GENBANK lead to the discovery of PD-1 ligand 2 (PD-L2, B7-DC, CD273), which shares 38% identity with PD-L1 [38]. The same molecule was identified independently as B7-DC in a subtractive analysis of cDNA libraries of DC and activated macrophage [39]. PD-L2 has similar structural arrangement as PD-L1 and is 23% identical to B7-1. In contrast to the universal expression of PD-L1, PD-L2 expression is restricted to professional antigen presenting cells. It is also expressed by a subset of resting peritoneal B1 cells, and induced on macrophages and DCs upon stimulation with IFN- γ , GM-CSF, or IL-4 [24, 36].

2.2.2 Function and signaling of PD-1

Although PD-1 was discovered to be associated with apoptosis, overexpression of PD-1 alone failed to induce cell apoptosis [22]. The immunosuppressive role of PD-1 to

maintain peripheral tolerance was first evidenced by the autoimmune symptoms developed by PD-1 knockout mice [40, 41]. Polymorphisms of gene *PDCDI* in human is also associated with various autoimmune diseases including SLE, rheumatoid arthritis, Type I diabetes, etc, among different populations [42]. Although costimulation of T cell function by PD-L1 and PD-L2 was reported, increasing evidences consolidated the inhibition of T cell function by PD-1, whereas the costimulation observed might originate from the interactions with additional receptors on T cell surface [43-49]. In addition to maintaining immune quiescence, PD-1 also limits antigen-specific T cell responses during bacterial or viral infections. The outcome is the formation of memory T cells with undetectable PD-1 expression after pathogen clearance in an acute infection, or the chronic co-existence of pathogen and exhausted antigen-specific T cells with persistent high expression of PD-1 [30, 50-55]. The exhaustion is manifested phenotypically as gradual loss of proliferative potential, cytokine production, and kill capacity, and transcriptionally and epigenetically a state different from effector and memory cells [56, 57]. While many state it as a mechanism hijacked by pathogens to escape the immune response, a more neutral perception considers the benefits of avoiding immunopathology and deletion of high-affinity T cell clones due to over activation, and thereby extends the current paradigm of immune response to multiple modes, just like different strategies in a 100-m race vs. in a marathon. Nevertheless, antibody blockade of the PD-1 pathway is able to partially restore effector functions of exhausted CD8⁺ T cells and promote viral clearance [30, 53]. Moreover, the upregulation of PD-L1 on multiple tumors, the exhaustion of tumor antigen-specific CD8⁺ T cells, and the enhanced anti-tumor immunity following PD-1/PD-L1 blockade together drove PD-1/PD-L1 based therapeutics from bench to bedside [33, 58]. The high response

rates (alone or combined with other therapies) to multiple cancer types and the mild adverse effects make it a promising target of tumor immunotherapy with monoclonal antibody drugs nivolumab and pembrolizumab on market now and more coming out of the pipe line [42, 59]. The benefits of such blockade are attributed to the improved functions of intratumoral CD8⁺ T cells and also the enhancement by the interaction of the antibodies with Fcγ receptors [60, 61]. In addition to the general inhibitory effects on conventional T cells, the more complex functions of PD-1 are reflected by its important role in the generation and function of induced regulatory T cells [62-64], its high expression on follicular helper CD4⁺ T cells [65], the improved cognitive performance in an Alzheimer's mouse model with PD-1 blockade [66], and even its expression on and promoting growth of certain tumor cells [28].

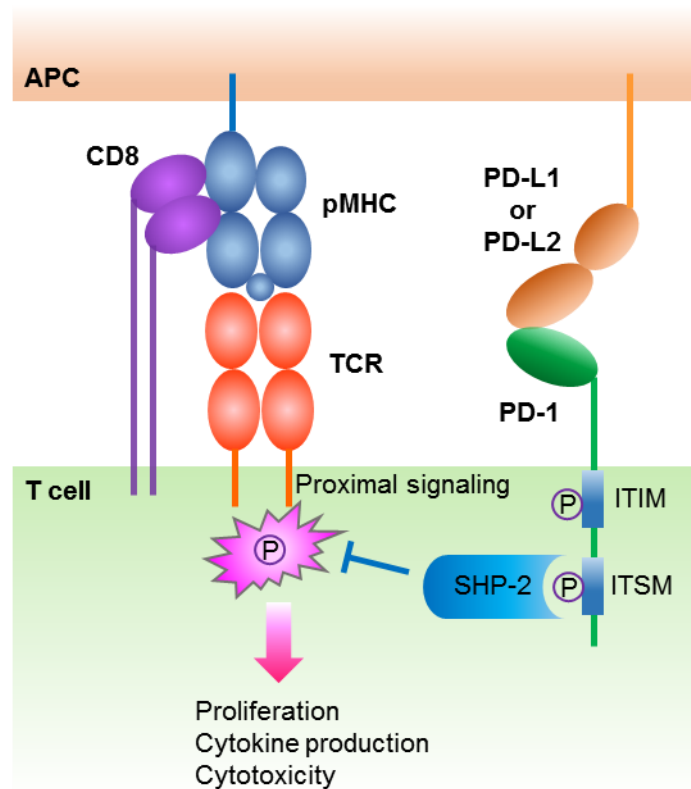


Figure 2.1: Mechanisms of PD-1 inhibition of TCR signaling and T cell effector functions.

Different from the functional role of ITIM in other inhibitory receptors, the PD-1 ITIM seems to be dispensable for the inhibitory function. Instead, mutation of the Try in ITSM abolishes PD-1 inhibition in both T and B cells [41, 67]. Immunoprecipitation identified the association of SHP-2 with ITSM in several models: (1) co-ligation of BCR and Fc γ R-PD-1 chimeric receptor in a B lymphoma cell line [41], 2) pervanadate stimulation of CD4⁺ T cells expressing mCD28–hPD-1 chimeric receptor or wild-type Jurkat cells [67, 68], and 3) MCC₈₈₋₁₀₃ pulsed DC-1 stimulation of AND TCR hybridomas expressing PD-1 [69]. Recruitment of SHP-1 by ITSM remains controversial as it was only detected in (2), maybe due to the nonphysiological responses to pervanadate stimulation. The recruitment of phosphatase(s) then leads to reduced phosphorylation of molecules in TCR and CD28 pathways from as upstream as CD3 and ZAP-70 to downstream PI3K–Akt and PLC γ 1–Ras–MEK–ERK axis [68-71]. The direct interference with early TCR/CD28 signaling endows PD-1 the potent inhibitory effect to a broad cell functions, from cell arrest with “stop signals” to cell cycle progression, metabolism conversion, and cytokine production, etc (Figure 2.1) [71-75].

2.2.3 Interactions of PD-1 with its ligands

Crystal structures of murine PD-1 in complex with human PD-L1 or murine PD-L2 show a 1:1 receptor-ligand stoichiometry, as suggested also by the monomeric forms of PD-1 and ligands in solution and on cell membrane [18-20, 76]. Interestingly, the complex manifest the interactions of variable domains from antigen receptors (V_H/V_L for BCR and V α /V β for TCR) by using their A'GFCC'C'' β -sheets to interact with each other while leaving the loops exposed [18-20]. This is quite different from the B7-1 binding to CD28 and CTLA-4, a monomeric interaction for the former and a dimeric interaction for the

latter. Besides, B7-1–CTLA-4 binding occurs at their GFCC' β -sheets with an orthogonal docking [77].

Binding of murine PD-1 to either hPD-L1 or mPD-L2 induces modest conformational changes in the FG loop. On the ligand side, conformation change of found in CC' loop of mPD-L2 but not hPD-L1. Moreover, structural comparison of hPD-1 with mPD-1 in forms of Apo or in-complex reveals significant differences. Apo-hPD-1 displays different positioning of the FG loop and BC loop, and the absence of C'' strand makes a long C'D loop [18]. hPD-L1 binding to hPD-1 changes the hPD-1 CC' loop from open to closed conformation, whereas the CC' loop in apo-mPD-1 is already closed [78]. These structural differences suggest the binding properties of PD-1 to vary by ligands and species.

Several groups reported the affinity and kinetics of human and murine PD-1 ligand interactions measured using surface plasma resonance (SPR). Most of them used Ig fusion protein constructs giving K_d values with large discrepancies (0.01 - 0.77 μ M) [79-82]. More accurate results were obtained using monomeric PD-1 and PD-1 ligands compiling K_d values of 8.2, 2.3, 29.8, and 38.4 μ M for hPD-1–hPD-L1, hPD-1–hPD-L2, mPD-1–mPD-L1, mPD-1–mPD-L2, respectively [18]. Comparing with the strong interactions between B7-1 and CTLA-4 ($K_d = 0.4 \mu$ M), human hPD-1 ligand interactions are weaker and similar to B7-1–CD28 ($K_d = 4.3 \mu$ M) [83].

2.2.4 Additional interactions for PD-1 ligands

Additional binding partners have been identified for PD-L1 and PD-L2. PD-L1 is able to bind B7-1 with slightly lower affinity than to PD-1 and induce bi-directional inhibitory signaling in the absence of CD28 and CTLA-4 [80, 82]. In vivo administration of antibody that specifically blocks PD-L1–B7-1 but not PD-L1–PD-1 suggest a role for

this interaction in the induction and maintenance of periphery tolerance [84, 85]. PD-L2 is recently reported to bind Repulsive Guidance Molecule b (RGMb) with similar affinity to PD-1 and promote respiratory tolerance [86]. These new interactions bring more complexity to the PD-1 system with the outcome determined by the cell type, the expression level of these molecules, their binding properties, and signaling capacities.

2.3 CD222

CD222 is a ~300 kDa type-I transmembrane protein belonging to the p-type lectin family typically known as Cation-Independent Mannose 6-Phosphate Receptor (CI-MPR) or Insulin-Like Growth Factor-II Receptor (IGF2R). Independent studies of CI-MPR and IGF2R converged at the point that they are the same protein [87]. The extracellular domain of human CD222 consists of 15 homologous repeats with each of 134 - 167aa and can form non-covalent dimer via interactions presumably across the whole length of the ectodomain [88, 89]. The 164aa cytoplasmic tail contains one palmitoylation site, two phosphorylation sites (Ser), and multiple binding sites for transport proteins [90]. CD222 is universally expressed in various mammalian cell types with a major distribution to intracellular compartments [91].

One major function of CD222 is to transport newly synthesized lysosome enzymes from *trans*-Golgi network (TGN) to endosomes. This is achieved through the recognition of the M6P moieties on these cargos by the M6P binding sites mapped to domain 3 and domain 9, a similar mechanism adopted by Cation-Dependent Mannose 6-Phosphate Receptor (CD-MPR), the other member of the family [92]. The same mechanism was also used to recycle extracellular lysosome enzymes by CD222 on the plasma membrane. Mutations affecting this pathway can cause diseases of lysosomal dysfunction [93].

Another line of research focuses on the binding of CD222 to IGF-II, which depends on domain 11 and 13 without involving M6P recognition [94]. This interaction is thought to mainly control the level of soluble IGF-II for IGF1R binding, as suggested by the rescue of fetal lethal phenotype of CD222 knockout mice by inactivation of either IGF-II or IGF1R [95]. A series of studies also suggest that IGF-II binding induces direct association and activation of various G proteins by CD222 cytoplasmic tail, a model still remains elusive due to conflicting observations [96-100].

In addition to the two types of ligands above, a panel of proteins have been found to interact with CD222 and lead to various functions depending on the cell type and the ligand engaged. For example, CD222 binds to Transforming Growth Factor β 1 (TGF- β 1) precursor (via M6P), Urokinase Receptor (uPAR), and plasminogen to activate TGF- β 1 from its latent form [101, 102]. Binding to proliferin by CD222 induced endothelial-cell migration and angiogenesis [103]. Retinoic Acid (RA) can bind to CD222 and cause growth inhibition and induction of apoptosis [104-106]. There are also interactions detected with *in vivo* functions not clearly defined, such as the binding to Leukemia Inhibitory Factor (LIF) and Human Hemochromatosis Protein (HFE). Of note, CD222 is also found on T cell surface after activation and plays multiple roles in regulating normal T cell function. CD222 is able to bind Lck and transport intracellular Lck to cell membrane to maintain normal TCR signaling [107]. It is also suggested to enhance T cell activation by internalizing CD26 via M6P binding [108]. During the contraction phase of CD8⁺ T cells in mice infected with *Listeria monocytogenes* expressing OVA (LmOVA), CD222^{high} CD8⁺ effector T cells are more likely to internalize granzyme B and undergo apoptosis,

whereas CD222^{low} CD8⁺ effectors preferentially survive and seed the memory T cell pool [109], the same mechanism that was involved in enhanced killing of target cells [110].

CHAPTER 3

MATERIALS AND METHODS

3.1 Cells

3.1.1 Cell lines

Chinese hamster ovary (CHO) cells, Jurkat cells clone E6.1, and Raji B cells were purchased from American Type Culture Collection (ATCC). CHO cells expressing mB7-1 were a generous gift of Dr. Periasamy Selvaraj (Emory University, Atlanta, GA). Jurkat E6.1 cells expressing hPD-1 were a generous gift of Dr. Simon Davis (The University of Oxford, London, UK). THP-1 cells were a generous gift of Dr. Arash Grakoui (Emory University, Atlanta, GA). All the cells above were cultured at 37 °C with 5% CO₂ in R10 medium: RPMI 1640 (Cellgro) supplemented with 10% FBS (Cellgro), 100 U/mL penicillin (Cellgro), 100 µg/mL streptavidin (Cellgro), 2 mM L-glutamine (Cellgro), and 20 mM HEPES (Cellgro). mB7-1 CHO cells were cultured with the addition of 0.4 mg/ml G418 (Cellgro).

3.1.2 Primary Cells

OT-I transgenic, P14 transgenic, and PD-1 knockout P14 transgenic mice were housed at the Emory University Department of Animal Resources facility following protocol approved by the Institutional Animal Care and Use Committee of Emory University. Total splenocytes were prepared by mechanical grinding of the spleen followed by RBC lysis (eBiosciences) according to the manufacturer's instructions. OT-I or P14 splenocytes were incubated at a density of 2 million/ml for 2 hr at 37 °C with 1 nM OVA₂₅₇₋₂₆₄ (SIINFEKL) or 10 nM LCMV gp₃₃₋₄₁ (KAVYNFATM), respectively. Cells were then

washed with HBSS, resuspended in R10 medium and cultured at 4 million/3 ml/well in 12-well plate at 37 °C with 5% CO₂. CD8⁺ T cells were purified on Day 2 or Day 3 post activation via Ficoll gradient separation followed by CD8 negative purification with magnetic beads (Miltenyi Biotec).

Whole blood of healthy donors were acquired according to a protocol approved by the Institutional Review Board of the Georgia Institute of Technology [9, 10, 12]. RBCs and PBMCs were separated via Ficoll gradient centrifugation.

3.1.3 Generation of stable transfectants

cDNAs of hPD-1 (BC074740), mPD-1 (BC120602), and hB7-1 (NM_005191.3) were subcloned into pcDNA3.1 (+) mammalian expression vector (Life Technologies). hCD222 (NM_000876.1) cDNA vector was purchased from Origene, and subcloned into pDEST-47 vector for expression of GFP fusion protein.

CHO cells were transfected with the expression vectors above using nucleofection (Lonza) kit T following the instructions provided. To generate stable cell lines, transfected cells were subjected to G418 selection (0.4 mg/ml) and multiple rounds of FACS sorting for uniform surface receptor expression labeled by respective antibodies conjugated with PE/APC (or GFP signals for hCD222-GFP CHO).

3.2 Proteins, antibodies, and chemicals

3.2.1 Proteins

His₆-tagged hPD-L1, hPD-L2, mPD-L1, and mPD-L2 with BirA sequence, as well as His₆-tagged hPD-1, hCD28, and hCTLA-4 fused with mIgG1 Fc were produced in CHO cells by Dr. Simon Davis lab (Oxford University, London, UK) using approaches described

previously [83, 111, 112]. Biotinylation was performed in vitro using the BirA biotin-protein ligase kit (Avidity). His₆-tagged hCD222 AA43-1365 produced in CHO cells and His₆-tagged hCD222 AA1510-2108 produced in mouse myeloma cells were purchased from R&D Systems. Wide type and α 3A2 mutant of H2-K^b: OVA₂₅₇₋₂₆₄ and H2-D^b: gp33-₄₁ were made by the National Institutes of Health Tetramer Core Facility at Emory University.

3.2.2 Antibodies and labeling reagents

anti-hPD-1-PE (MIH4), anti-hPD-1-APC (MIH4), anti-hPD-L1-PE (MIH1), anti-hPD-L2-PE (MIH18), anti-mPD-1-PE (J43), anti-mB7-1-PE (1G10/B7), anti-hCD28 (CD28.2), anti-hCTLA-4 (BNI3), anti-mTCR V α 2 (B20.1), anti-mCD8 α -PE (53-6.7), anti-hCD14-FITC (M5E2), isotype mIgG1, κ -PE (MOPC-21), isotype RatIgG2a, λ -PE (B39-4), isotype RatIgG2a, κ -PE (A95-1), and isotype American hamster IgG2, κ -PE (B81-3) were from BD Pharmingen. Anti-mPD-L1-PE (MIH5), anti-mPD-L2-PE (TY25), anti-hB7-1-PE (2D10.4), anti-H2K^b:SIINFEKL-PE (25-D1.16), anti-hCD3-APC (OKT3), and isotype RatIgG2a, κ -PE (eBR2a) were from eBiosciences. Anti-H2D^b-PE (KH95), anti-hB7-1-APC (2D10), anti-hCD3-FITC (UCHT1), anti-hCD8 α -PerCP (HIT8a), anti-hCD20-PerCP-Cy5.5 (2H7), anti-hCD56-PE-Cy7 (HCD56), isotype mIgG2a, κ -PE (MOPC-173), isotype mIgG2b, κ -PE (MPC-11), isotype RatIgG1, κ -PE (RTK2071), and CFSE were from Biolegend. Anti-hCD222-PE (MEM-238), anti-hCD222-APC (MEM-238), isotype mIgG1, κ -PE, isotype mIgG1, κ -APC, Streptavidin-PE, streptavidin-APC, and Live/Dead NIR were from Life Technologies. Anti-pERK-PE (197G2) and isotype Rabbit IgG-PE (DA1E) were from Cell Signaling. Biotin-anti-PentaHis was from Qiagen.

3.2.3 Blocking reagents

The following antibodies were used for blocking the binding of the respective molecules: anti-hPD-1 clone EH12.2H7 (Biolegend), anti-mPD-1 clone J43 (BD Pharmingen), anti-hPD-L1 clones MIH1 (BD Pharmingen), MIH2 (Abcam), 29E.2A3 (Biolegend), 1B12 (Abcam). anti-hPD-L2 clone MIH18 (Biolegend), anti-hB7-1 clone 2D10 (Biolegend), anti-mB7-1 clone 16-10A1 (eBiosciences), anti-hCD222 clones MEM-238 (Abcam), NEM-239 (Creative Diagnostics), NFN-349 (Creative Diagnostics), and 2G11 (Thermo Scientific). The antibodies were used at a concentration of 10 µg/ml unless noted otherwise. NaM6P (Sigma Aldrich) was used to block the M6P binding sites of CD222 at concentrations as noted.

The following chemicals were used to inhibit the activities of signaling molecules: PTP inhibitor I (Santa Cruz) for SHP-1, NSC87877 (Santa Cruz) for SHP-1 and SHP-2, and 7-Cyclopentyl-5-(4-phenoxyphenyl)-7H-pyrrolo[2,3-d]pyrimidin-4-ylamine (Sigma Aldrich) for Lck.

3.3 Flow cytometry and fluorescent imaging

3.3.1 General surface staining with antibodies

Samples were pre-blocked with blocking reagent for 15 min at 4 °C as needed, and then without washing stained for 30 min at 4 °C in 100 µl of FACS buffer (PBS without Ca²⁺ or Mg²⁺, 5 mM EDTA, 2% FBS) containing 10 µg/ml (or as suggested by the product instruction) of antibodies of interest. Fluorescent tetramers were made by mixing biotinylated proteins with SA-PE or SA-APC following the instructions of National Institutes of Health Tetramer Core Facility. Tetramers were added at an equivalent monomer concentration of 2 µg/ml. Isotype Igs and SA-PE/APC controls were added at

an amount equal to that in respective samples. Samples were washed twice with 2 ml of FACS buffer, fixed with 200 μ l of 1% PFA for 15 min at 4 °C, washed once with 2 ml of FACS buffer, and then resuspended in 300 μ l of FACS buffer for analysis under LSR II flow cytometer (BD Biosciences). Flow cytometric data were analyzed using FACS DIVA (BD Biosciences) and FlowJo (TreeStar).

3.3.2 Intracellular staining of pERK

0.5 million Jurkat E6.1 cells were pre-blocked on ice with the blocking reagents (e.g. NaM6P) as needed, and then mixed with ice-cold R10 containing soluble proteins (e.g. anti-CD3, hPD-ligand tetramers, and their mixture) or functionalized SA beads. Stimulation was enabled by transferring the mixture into 37 °C water bath. For beads stimulation, the mixture was centrifuged at 1,200 rpm for 1 min at 0 °C before transferring into 37 °C. Reaction was stopped at the indicated time points by transferring the samples back on ice, followed by addition of 200 μ l of 4% PFA. Samples were then incubated on ice for 30 min, washed with 200 μ l of FACS buffer, and then incubated with 200 μ l of 90% methanol for 30 min on ice. Permeabilized samples were washed 2x with 200 μ l of FACS buffer, resuspended in 100 μ l of FACS buffer containing 2 μ l of anti-pERK-PE or rabbit-IgG-PE, and incubated at room temperature for 1 hr. Samples were then washed 2x with 200 μ l of FACS buffer before analyzing by flow cytometer.

3.3.3 CFSE staining of human PBMCs

10 million peripheral blood mononuclear cells (PBMCs) were incubated in 2 ml of PBS with 5 μ M CFSE at 37 °C for 10 min. Staining was quenched with 44 ml of cold R10 medium, and washed again with 15 ml cold R10 medium. Cells were resuspended in warm R10 at 1 million/ml and seeded at 500 μ l/well in 24-well plate coated with anti-CD3

(OKT3, 1 $\mu\text{g/ml} \times 500 \mu\text{l}$, 4 °C, overnight) or control Ig. Cells were harvested at the time points indicated and stained first with Live/Dead NIR according to the manufacturer's instructions, followed by staining using anti-CD3-PE along with anti-PD-1-APC, anti-B7-1-APC, anti-CD222-APC or mIgG1, κ -APC at 4 °C for 30 min. Samples were then washed, fixed, and analyzed following the general staining protocol as stated in 3.3.1.

3.3.3 Confocal imaging

CD222-GFP CHO cells were detached with 5 mM EDTA/PBS, washed and resuspended in HBSS and added to cover slide. Cells were imaged under LSM 510 confocal microscope (ZEISS) equipped with a Plan-Apochromat 100x/1.40 oil objective using x,y scanning mode. Cells were excited with 488 nm laser with the emission collected at 525 nm.

3.4 2D and 3D kinetic assays

3.4.1 Micropipette adhesion frequency assay

The theoretical framework and detailed procedures have been reported previously [10, 113, 114]. In brief, binding events of cells expressing the receptor of interest were analyzed against human red blood cells (RBCs) coated with controlled densities of respective ligand for well-defined contact durations. Human RBCs of healthy donors were biotinylated, functionalized with saturating amount of streptavidin (SA) and washed [10]. SA-coated RBCs were then incubated with biotinylated recombinant proteins and washed prior to adhesion frequency assay or flow cytometric analysis. As an example, a CHO expressing PD-1 and a RBC coated with PD-1 ligand were repetitively brought in contact for a well-defined duration (t_c) with a constant contact area (A_c). Adhesion frequency (P_a)

was calculated over scoring 50 contact cycles, with each giving 1 for adhesion or 0 for no adhesion based on the deflection of the RBC membrane upon separation. The adhesion frequency curve (P_a vs t_c), which monotonically increases then plateaus (Figure 3.1A), reflects the kinetic nature of the molecular bond formation and dissociation at the cellular interface and can be well-fitted to the following equations assuming a single step first order reaction [113]

$$P_a = 1 - \exp(-\langle n \rangle) \quad (1)$$

$$\text{and } \langle n \rangle = m_r m_l A_c K_a [1 - \exp(-k_{off} t_c)]. \quad (2)$$

Here $\langle n \rangle$ is the average number of bonds per contact, m_r and m_l are the respective densities of the receptor (e.g. hPD-1) on the CHO cell and the ligand (e.g. hPD-L1) on the RBC that can be measured using PE-labeled monoclonal antibody together with QuantiBRITE PE standard beads (BD Biosciences), A_c is the contact area, K_a is the 2D affinity (in μm^2), and k_{off} is the off-rate (s^{-1}). Since A_c and K_a cannot be separated in curve fitting, they are lumped together as the effective 2D affinity $A_c K_a$. Together with 2D off-rate (k_{off}) they were determined from least-mean-square fitting. 2D on-rate was further calculated as

$$A_c k_{on} = A_c K_a \times k_{off}. \quad (3)$$

The adhesion frequency assay was confirmed to have single-bond sensitivity yet remains highly specific. For CHO cells expressing 128 hPD-1 molecules per μm^2 , RBCs coated with hPD-L1 (16.4 / μm^2) or hPD-L2 (5.3 / μm^2) generated P_a of 0.62 or 0.6, respectively, whereas RBCs coated with SA alone (ligand-free) gave $P_a < 0.1$ (Figure 3.1B). The P_a was also reduced to background level when hPD-1 was blocked using a monoclonal antibody (clone EH12.2H7) or using WT CHO cells without PD-1 expression,

further confirming the detected bond formation are specific to the receptor-ligand pair being analyzed.

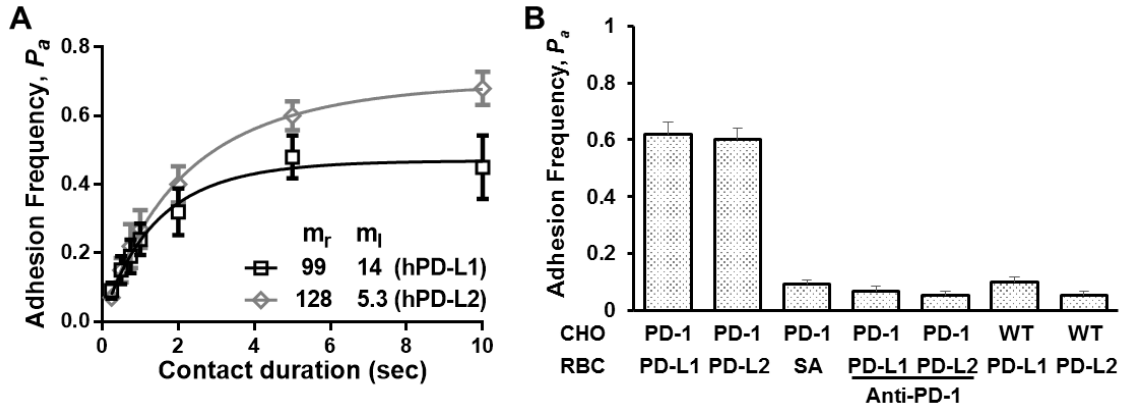


Figure 3.1: 2D kinetic analysis using adhesion frequency assay. A) Adhesion frequency curves for hPD-1–hPD-ligand interactions. Each point represents mean \pm SEM of 3-5 cell pairs tested for the corresponding contact duration. B) Representative specificity controls of adhesion events for hPD-1 ligand interactions including ligand-free RBCs, receptor-free WT CHO cells, or PD-1 CHO cells with anti-PD-1 blocking.

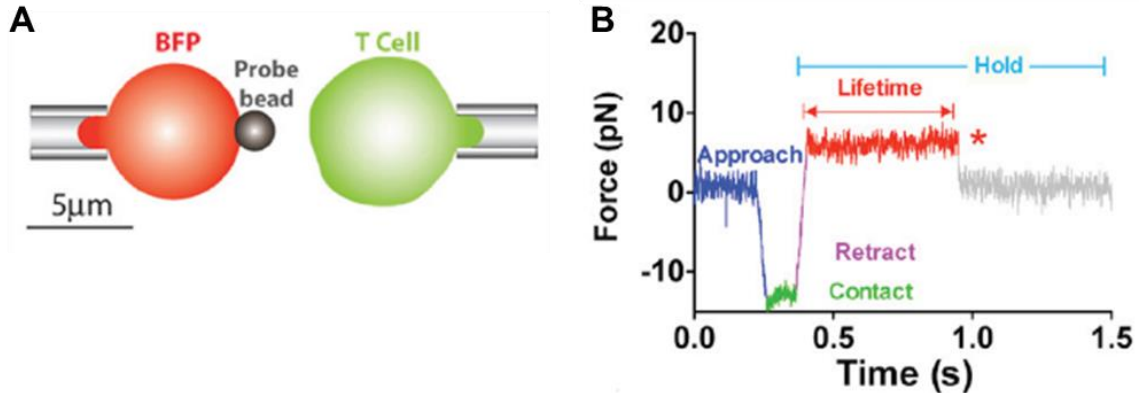


Figure 3.2: Force-clamp assay using biomembrane force probe. A) Schematics of the BFP setup. The probe bead was coated with biotinylated ligand through SA coupling and attached to the biotinylated RBC aspirated by the micropipette (Left). B) Representative force trace showing a measurement cycle with bond lifetime detected at the set force level. (Adapted from Liu, B., et al. (2014). Cell 157(2): 357-368.)

3.4.2 Biomembrane force probe force-clamp assay

Biomembrane force probe (BFP) measurement of single bond lifetime in response to force has been described previously [115]. In brief, a T cell is repetitively brought into contact with a ligand coated glass bead attached to a micropipette aspirated RBC, then

retracted and held at a distance corresponding to the set force level (Figure 3.2). The displacement of the bead is tracked at 1000 fps with sub-nanometer precision. The displacement trace is then translated into force trace with a preset RBC spring constant to 0.3 pN/nm (Figure 3.2B). Molecular bond formed between the ligand on the bead and the receptor on the T cell pulls the bead away from its original position during T cell retraction, as reflected by the increase in force applied on the bond in the force trace (Figure 3.2B). The force (bead displacement) sustains until the bond ruptures, with the total duration defining the bond lifetime under the clamped force level (Figure 3.2B). Repeated measurement cycles at multiple force levels generated a pool of such events, which are usually presented in the form of average bond lifetime $\langle t \rangle$ vs average force by automatically or manually binning the events based on force. Cumulative histogram of lifetime events for each bin can also be calculated as the number of events with lifetime greater than t .

3.4.3 Cooperativity analysis of bond number and bond lifetime

Micropipette adhesion frequency-based cooperativity analysis of total bond number consisting of dual receptor-ligand species has been described previously [12, 116, 117]. For the molecular systems in this study, the average bond numbers for RBCs coated with individual or mixed ligands were calculated as following:

$$\langle n \rangle_{pMHC} = -\ln(1 - P_{a_pMHC}), \quad (4)$$

$$\langle n \rangle_{PD-L1} = -\ln(1 - P_{a_PD-L1}), \quad (5)$$

$$\text{and } \langle n \rangle_{mix} = -\ln(1 - P_{a_mix}). \quad (6)$$

When $\alpha 3A2$ mutant pMHC were used, $\langle n \rangle_{pMHC}$ is equivalent to $\langle n \rangle_{TCR-pMHC}$ alone. With WT pMHC, $\langle n \rangle_{pMHC}$ is the lumped sum of three types of molecular bonds:

TCR–pMHC, CD8–pMHC, and TCR–CD8–pMHC, where CD8–pMHC is negligible according to its 2-log to 3-log lower affinities than that of TCR–pMHC in this study. Assuming concurrent and independent interactions of pMHC and PD-L1 with their respective binding partners on T cells, the predicted total bond number would be the simple addition of individual ones [116, 117]

$$\langle n \rangle_{total} = \langle n \rangle_{pMHC} + \langle n \rangle_{PD-L1}. \quad (7)$$

The net cooperativity is then calculated as the difference between predicted total bond number and that measured in the mixture coating condition

$$\Delta \langle n \rangle = \langle n \rangle_{mix} - \langle n \rangle_{total}. \quad (8)$$

We name it apparent “positive cooperativity” or “negative cooperativity” in the case $\Delta \langle n \rangle > 0$ or $\Delta \langle n \rangle < 0$, respectively. The percentage of changes in bond number is then defined as $\Delta \langle n \rangle / \langle n \rangle_{total}$. To reduce cell-cell variation among groups with different coating, we improved the protocol by testing the same T cell randomly against three RBCs with individual coating or mixture coating, which allowed for analyzing cooperativity with paired single-cell readout.

For cooperativity analysis of bond lifetime, the concept is similar except that the readout now is the lifetime of single bonds from all possible interactions involved. By binning the events based on their clamping force, we calculated the average bond lifetime for each coating conditions: $\langle t \rangle_{pMHC}$, $\langle t \rangle_{PD-L1}$, and $\langle t \rangle_{mix}$. Again, $\langle t \rangle_{pMHC}$ is equivalent to $\langle n \rangle_{TCR-pMHC}$ alone when using $\alpha 3A2$ mutant pMHC, whereas with WT pMHC, $\langle n \rangle_{pMHC}$ is the weighted sum of lifetime from three types of molecular bonds: TCR–pMHC, CD8–pMHC, and TCR–CD8–pMHC, where the weight components represent the normalized fractions as in average bond numbers. Also, the assumption of concurrent and independent

binding predicts that the fractions of the molecular bonds (f) are determined by their 2D affinity/avidity and their respective receptor and ligand densities, with the predicted average bond lifetime defined as

$$\langle t \rangle_{total} = f_{pMHC} \langle t \rangle_{pMHC} + f_{PD-L1} \langle t \rangle_{PD-L1}. \quad (9)$$

The difference between predicted and measured average bond lifetime then defines the cooperativity in lifetime

$$\Delta \langle t \rangle = \langle t \rangle_{mix} - \langle t \rangle_{total}. \quad (10)$$

Since $\langle t \rangle_{pMHC}$ is much longer than $\langle t \rangle_{PD-L1}$ at low force level, the reduced fractions of bonds observed in bond number cooperativity analysis could then be further resolved, with reduced $\langle n \rangle_{pMHC}$ giving $\Delta \langle t \rangle < 0$, while missing $\langle n \rangle_{PD-L1}$ giving $\Delta \langle t \rangle > 0$. The same principle was also applied to analyze the histogram of lifetime within a certain force bin, where the averaged bond lifetime $\langle t \rangle$ is replaced with the lifetime distribution.

3.4.4 Surface plasma resonance

The SPR experiments were performed on a Biacore T200 (GE Healthcare) at 25 °C or 37 °C as stated. Biotinylated hPD-L1, hPD-L2, and control protein (LILRA2) were immobilized to SA sensor chip to ~2000 RU. For affinity measurement, serial dilutions of soluble CD222 D1-9 were injected in HBS-EP buffer (0.01 M HEPES pH 7.4, 0.15 M NaCl, 3 mM EDTA, 0.005% v/v Surfactant P20) at 10 μ l/min for 1 min, and allowed to dissociate for 2 min before regeneration by a 10-s injection of 1 mM HCl. Sensorgrams were analyzed using Biaevaluation software and fitted using the curve fitting tools to derive the affinity and kinetic parameters.

3.5 Biochemical assays

3.5.1 Receptor pulldown from Jurkat

150 million Jurkat E6.1 cells were harvested and washed with cold PBS. Cells were resuspended in 2 ml of cold hypotonic lysis buffer (10 mM HEPES, pH 7.4, 42 mM KCl, 5 mM MgCl₂, 1 x Halt protease inhibitor cocktail) and swelled on ice for 20 min. Cells were lysed by sonication (power 3.0, 8 sec × 3 cycles) on ice using ultrasound sonicator (Misonix), and clarified by two rounds of centrifugation at 15,000 g for 10 min each. Membrane pellet was collected by centrifuging clarified cell lysate at 140,000 g for 35 min. Membrane was washed with 2 ml of hypotonic lysis buffer and centrifuged again at 140,000 g for 10 min. Membrane was then dissolved in 1.6 ml of NP40 lysis buffer containing 1 x Halt protease inhibitor cocktail for 1.5 hr on ice. Undissolved fraction was eliminated by centrifugation at 120,000 g for 10 min. All the centrifugation step mentioned above were performed at 4 °C. Membrane lysate was then further clarified with 100 µl of SA beads (Dynabeads, SA-280) at 4 °C for 2.5 hr and were ready to use.

The total membrane lysate was split into two, and incubated overnight at 4 °C with 40 µl of SA beads coated with 2 µg of biotin-hPD-L1 or biotin-hPD-L2. Beads were then washed 3 x with NP40 lysis buffer containing 1 x Halt protease inhibitor cocktail, and subjected to the 1st elution with 20 µl of 0.2 M glycine buffer (3 min) and the 2nd elution with 40 µl of laemmli buffer at 99 °C for 10 min. Eluates from the 1st elution were quickly neutralized by adding 2 µl of Tris·HCl (pH 8.0). All eluates were subjected to 4% -15% SDS-PAGE analysis and displayed using Sypro Ruby staining (Life Technologies).

3.5.2 Mass spectrometry

Mass spectrometry samples were prepared from target gel sections via in-gel trypsin digestion. Briefly, gel pieces were destained with 1:1 mixture of acetonitrile and 50

mM ammonium bicarbonate (ABC), and dehydrated with acetonitrile till white and hard, followed by vacuum dry in Centrivap without heat. Reduction and alkylation were then performed by sequentially incubate gel pieces in 10 mM DTT (30 min) and 55 mM iodoacetamide (45 min in dark) at room temperature. After that, gel pieces were wash with 50 mM ABC and dehydrated with acetonitrile, followed by incubation with Trypsin (Promega) on ice for 30 min. Trypsin solution were then removed and replaced with 50 mM ABC for overnight incubation at 37 °C. Digested peptides were extracted by dehydration using acetonitrile, and then vacuum dried and frozen at -80 °C.

Peptide extracts were reconstituted in HPLC grade water, and analyzed with LTQ Orbitrap XL ETD hybrid linear ion trap/orbitrap tandem mass spectrometer with a mass accuracy of less than 2 ppm. Mass files were searched against both non-redundant and human databases using Mascot (Matrix Science) for peptide mass fingerprint matches with a peptide mass tolerance of 10 ppm and a MS/MS mass tolerance of 1.2 Da.

3.5.3 PNGase F treatment

For deglycosylation of native hPD-L1, 2 µg hPD-L1 in 10 µl of HBS (0.01 M HEPES, 150 mM NaCl, pH 7.4) was mixed with 2 µl (1,000U) of PNGase F (NEB) and incubated at 37 °C for 6 hr, and stored at 4 °C. hPD-L1 treated with the same process but without PNGase F was included as a negative control. For positive control of complete removal of N-glycans, 0.5 µg hPD-L1 in 2.5 µl HBS was mixed with 1 µl of denature buffer (NEB), 6.5 µl of H₂O, and boiled at 100 °C for 10 min. Denatured hPD-L1 was then mixed with 1.5 µl of glycoprotein buffer (NEB), 1.5 µl of NP40, 1 µl (500U) of PNGase F, 1 µl of H₂O, and incubated at 37 °C for 1 hr. All samples were separated by 4% - 15% SDS-PAGE followed by coomassie blue (Bio-Rad) staining.

3.6 Statistical analysis

Data from single group/point were presented in mean \pm SEM unless box-whisker plot was used. For box-whisker plot, the center line labels median, the box contains the two middle quantiles, and the whiskers mark the min and the max. Comparison of two groups were based on Mann-Whitney test unless student's t-test or paired t-test was noted.

CHAPTER 4

2D KINETIC ANALYSIS OF PD-1, PD-LIGAND, AND B7-1 INTERACTIONS

4.1 Introduction

The great therapeutic potential of PD-1 and its critical role in T-cell and B-cell biology demand a better understanding of the interactions within the complex PD-1/PD-ligands/B7-1 system. Extensive efforts have been made to interrogate these interactions using structural, mutagenesis, and SPR approaches, establishing our current knowledge pool with binding interface resolved, hotspot residuals and potentially distinct binding modes identified, and 3D binding properties measured [18-20, 48, 76, 79-81]. However, most of the kinetic studies used different dimeric protein constructs and reported kinetic parameters with large discrepancies. Recently, Cheng et al. characterized in detail the monomeric binding properties of purified PD-1, PD-1 ligands, and B7-1 proteins in conjunction with structural investigation and reported relatively weak affinities of PD-1 ligand interactions, and even lower values for the B7-1–PD-L1 interactions [18]. We and others have shown that, in contrast to 3D measurements, 2D kinetic parameters measured *in situ* with molecules expressed on the native cell membrane display different characteristics that reflect effective binding properties integrating both the physical and chemical determination of the binding interface and structural and/or organizational regulation by the cellular environment [118]. In addition, a better correlation with downstream cellular functions has been shown for 2D kinetics of TCR–pMHC interactions than 3D parameters [10, 13, 119-121]. Here we report a systematic 2D kinetic analysis of the PD-1/PD-ligand/B7-1 system in both human and murine species. The 2D parameters

follow the same trend as the 3D ones in general, but identify PD-1 ligand interactions in the middle to strong range. In contrast, 2D B7-1–PD-L1 interaction is much weaker than PD-1–PD-L1 for both human and murine. Finally, comparison of 2D vs 3D affinities for multiple molecular interactions reveals differential enhancement of ligand binding by the cellular environment.

4.2 Results

4.2.1 2D interactions of human PD-1

We performed micropipette adhesion frequency assay using CHO cells expressing human PD-1 (hPD-1) and RBCs coated with human PD-1 ligands to study their 2D interactions. All P_a vs t_c curves were well fitted to Eqs. 1 and 2 with three combinations of hPD-1 and ligand densities for each ligand (Figure 4.1A & B), indicating that the previously reported monomeric binding model in solution also applies to binding on the cell surface. The effective 2D affinity ($A_c K_a$) and 2D off-rate (k_{off}) were extracted from the curve fitting and used to derive the effective 2D on-rate using Eq. 3 (Table 4.1). Comparing the 2D kinetic parameters (Figure 4.1C-E, open columns) with their 3D counterparts (Figure 4.1C-E, solid columns) measured using SPR [18], the effective 2D affinities follow the same rank order as the 3D affinities, but show a greater difference between the two ligands, with the $A_c K_a$ for hPD-1–hPD-L2 3.75 fold higher than that of hPD-1–hPD-L1 interaction (Figure 4.1C). The 2D $A_c K_a$ values, $4.74 \pm 0.30 \times 10^{-4}$ and $2.12 \pm 0.56 \times 10^{-3} \mu\text{m}^4$ for hPD-L1 and hPD-L2, respectively, are similar or higher than that of TCR interacting with potent cognate pMHC ($2.4 \pm 0.2 \times 10^{-4} \mu\text{m}^4$ for OT-I TCR–H2-K^b:OVA

[10]) or strong interactions between high affinity LFA-1 and ICAM-1 ($3.30 \pm 0.62 \times 10^{-3} \mu\text{m}^4$) [122].

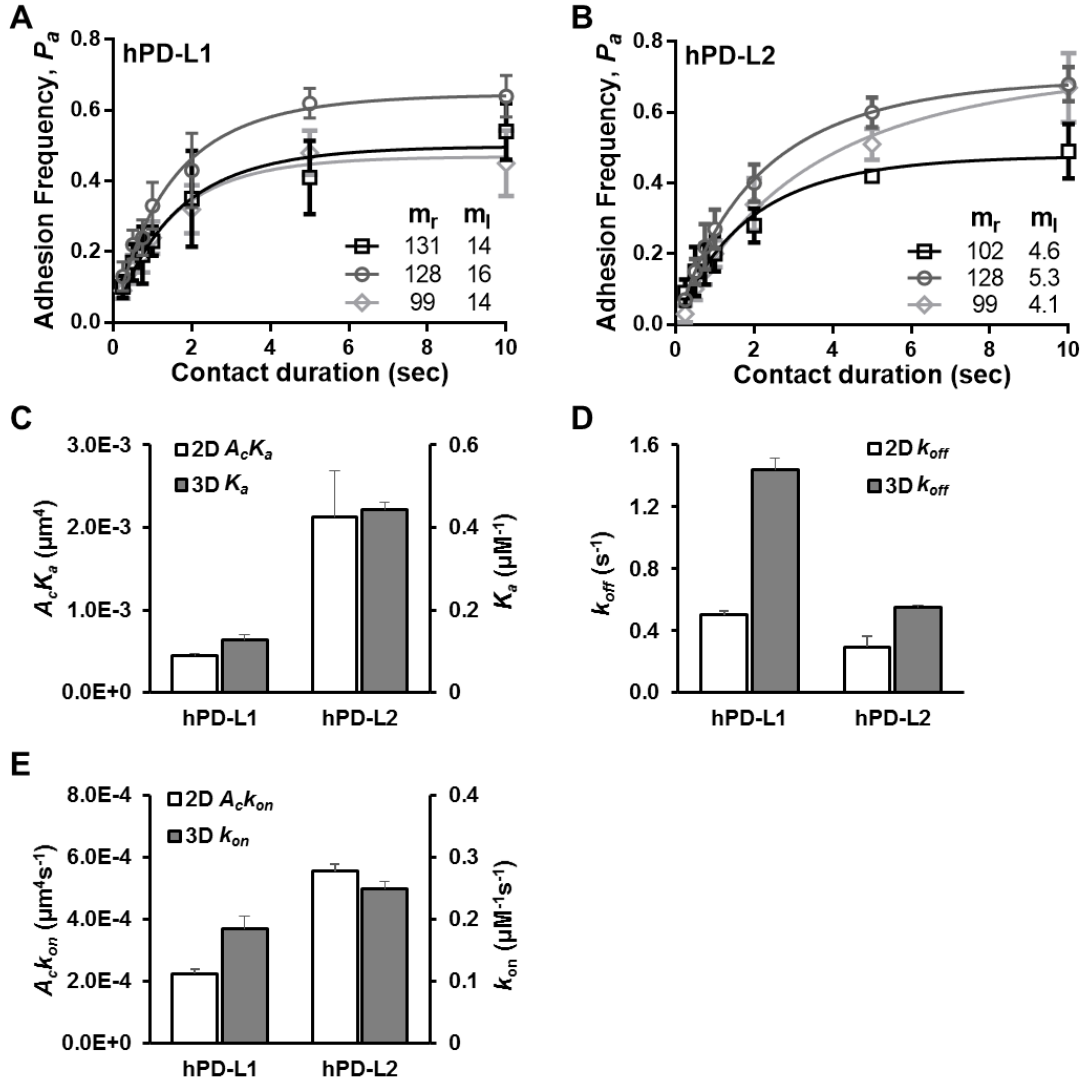


Figure 4.1: Comparison of 2D and 3D kinetics of human PD-1 ligand interactions. A) – B) Adhesion frequency curves of CHO cells expressing hPD-1 tested against RBCs coated with hPD-L1 (A) or hPD-L2 (B). Each curve represents an independent measurement with different receptor and ligand densities. **C) – E)** 2D effective affinity ($A_c K_a$, C), 2D off-rate (k_{off} , D) and 2D on-rate ($A_c k_{on}$, E) were derived from data shown in A) and B) using Eqs. 1, 2 and 3. The corresponding 3D kinetics were replotted based on the previous study using the same protein constructs [18]. Data represent mean \pm SEM.

The higher 2D affinity of PD-L2 than PD-L1 is caused by a slower 2D off-rate (0.30 ± 0.07 vs $0.50 \pm 0.03 \text{ s}^{-1}$, Figure 4.1D) and a faster 2D on-rate ($5.55 \pm 0.23 \times 10^{-4}$ vs $2.24 \pm 0.17 \times 10^{-4} \mu\text{m}^4 \text{s}^{-1}$, Figure 4.1E), both of which have the same rank order as their respective 3D

counterparts [18]. The 2D on-rate is on a similar scale as those of P-selectin glycoprotein ligand-1 (PSGL-1) interacting with P-selectin or L-selection, where the fast on-rates facilitates the capture and rolling of trafficking leukocytes on inflamed endothelial cells [123]. These 2D kinetic parameters indicate stronger ligand binding for PD-1 on the cell surface with slower off-rates and faster on-rates than previously appreciated based on 3D measurements using cell-free systems. Our results may account, at least in part, for PD-1's potent inhibition of TCR signaling.

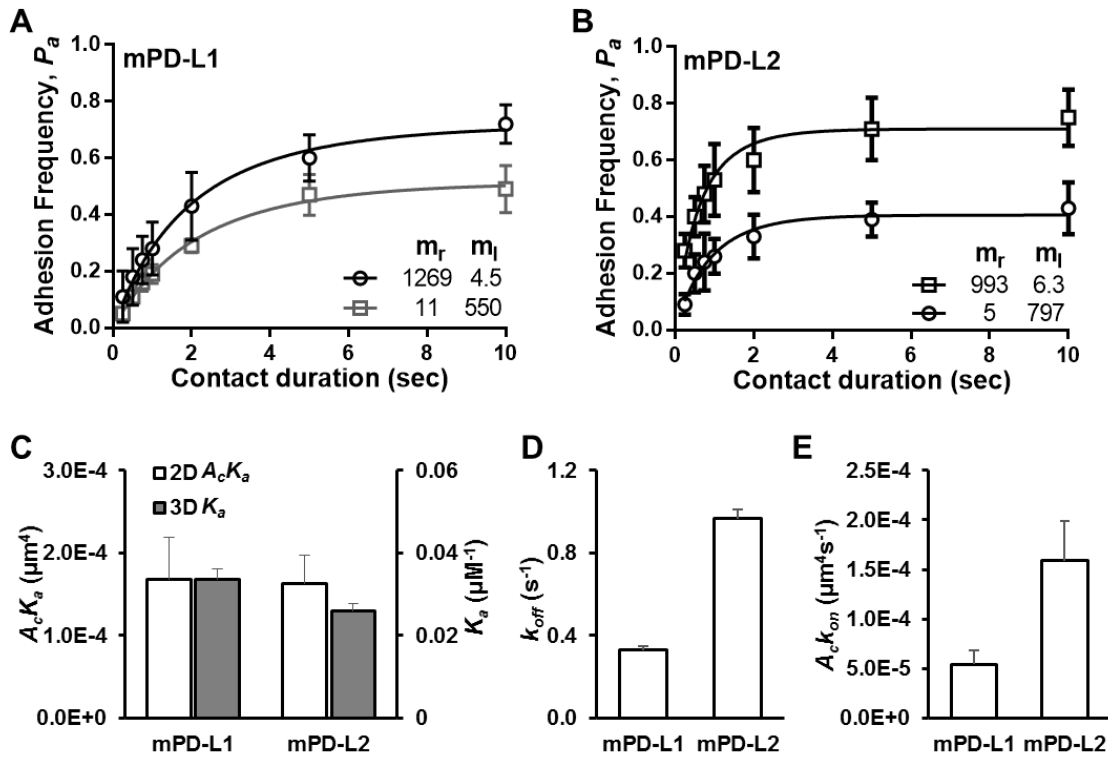


Figure 4.2: Comparison of 2D and 3D kinetics of murine PD-1 ligand interactions. A) – B) Adhesion frequency curves of CHO cells expressing mPD-1 tested against RBCs coated with mPD-L1 (A) or mPD-L2 (B). Each curve represents an independent measurement with different receptor and ligand densities. **C) – E)** 2D effective affinity ($A_c K_a$, C), 2D off-rate (k_{off} , D) and 2D on-rate ($A_c k_{on}$, E) were derived from data shown in A) and B) using Eqs. 1, 2 and 3. The corresponding 3D kinetics were replotted based on the previous study using the same protein constructs [18]. Data represent mean \pm SEM.

4.2.2 2D interactions of murine PD-1

We also characterized the 2D interactions of murine PD-1 (mPD-1) expressed on CHO cell surface with ligands coated on RBCs (Figure 4.2A & B, Table 4.1). Different from hPD-1, mPD-1 binds to both ligands with the same 2D affinities: $1.69 \pm 0.51 \times 10^{-4}$ and $1.63 \pm 0.34 \times 10^{-4} \mu\text{m}^4$ for mPD-L1 and mPD-L2, respectively (Figure 4.2C). However, the equal $A_c K_a$ was resulted from distinct kinetic rates: mPD-1 binds to mPD-L2 with a 3-fold $A_c k_{on}$, and dissociates ~ 3 -fold faster than mPD-L1 (Figure 4.2D & E). Both 2D and 3D measurements report lower ligand binding affinities for mPD-1 than hPD-1 (Figure 4.1 & Figure 4.2) [18]. The difference in 2D $A_c K_a$ is 2.65 fold for PD-1–PD-L1 but 13 fold for PD-1–PD-L2 interactions (Figure 4.1C & Figure 4.2C). The lower 2D affinities of mPD-1 are largely due to the slower 2D on-rate for mPD-L1 ($5.46 \pm 1.33 \times 10^{-5}$ vs $2.24 \pm 0.17 \times 10^{-4} \mu\text{m}^4\text{s}^{-1}$), and to both the slower 2D on-rate ($1.59 \pm 0.40 \times 10^{-4}$ vs $5.55 \pm 0.23 \times 10^{-4} \mu\text{m}^4\text{s}^{-1}$) and faster 2D off-rate (0.97 ± 0.05 sec vs 0.30 ± 0.07 sec) for mPD-L2.

4.2.3 2D interactions of PD-L1 with B7-1

PD-L1 has been reported to interact with B7-1 and deliver inhibitory signals bidirectionally [80, 82]. However, it remains controversial as how strong this interaction is comparing with PD-1–PD-L1 [18, 80]. To compare their interactions on the cell surface, we expressed hB7-1 or mB7-1 in CHO cells and tested their binding to PD-L1-coated RBCs. B7-1 has been shown to form non-covalent dimers on the cell surface [124, 125]. For both human and murine cases, however, the monomeric binding model (Eqs. 1 and 2) was able to simultaneously fit two adhesion frequency curves generated using two sets of molecular densities of B7-1 and PD-L1 (Figure 4.3A & B), suggesting that dimeric binding was not supported under our experimental conditions [126].

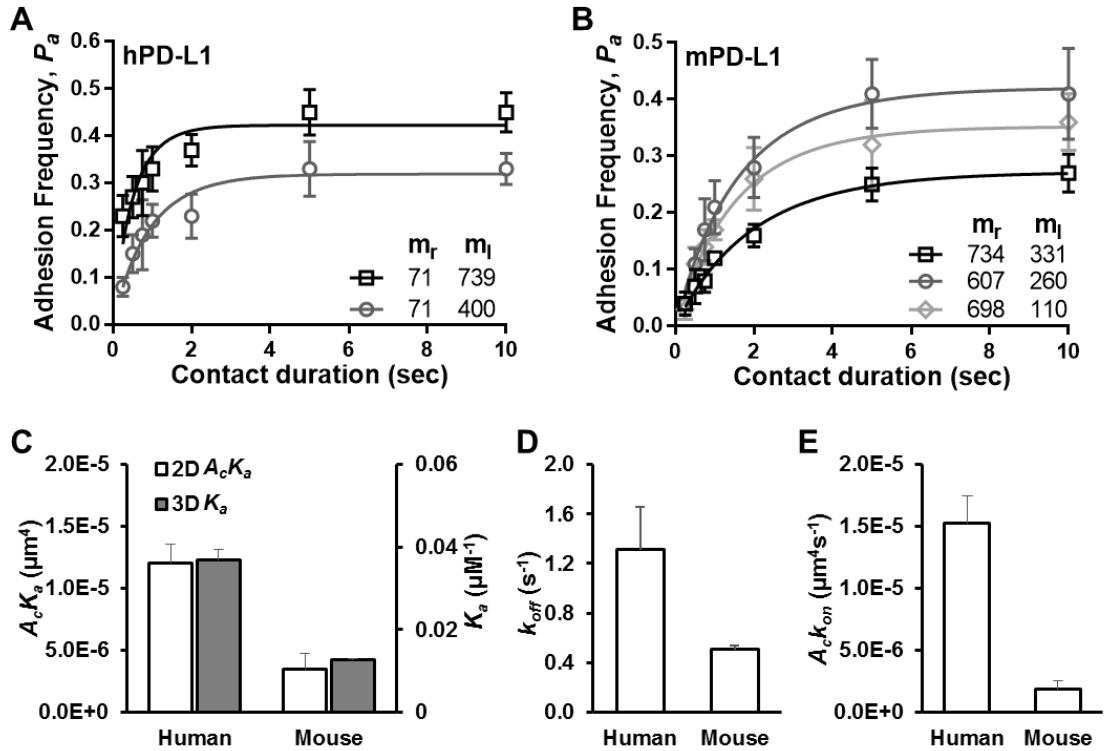


Figure 4.3: Comparison of 2D and 3D kinetics of human and murine B7-1-PD-L1 interactions. **A) – B)** Adhesion frequency curves of CHO cells expressing hB7-1 (A) or mB7-1 (B) tested against RBCs coated with hPD-L1 or mPD-L1, respectively. Each curve represents an independent measurement with different receptor and ligand densities. **C) - E)** 2D effective affinity ($A_c K_a$, **C**), 2D off-rate (k_{off} , **D**) and 2D on-rate ($A_c k_{on}$, **E**) were derived from data shown in A) and B) using Eqs. 1, 2 and 3. The corresponding 3D kinetics were replotted based on the previous study using the same protein constructs [18]. Data represent mean \pm SEM.

The 2D affinities are $1.21 \pm 0.16 \times 10^{-5} \mu\text{m}^4$ for human and $3.47 \pm 1.25 \times 10^{-6} \mu\text{m}^4$ for murine following the same trend as the 3D affinities (Figure 4.3C, Table 4.1). The higher $A_c K_a$ for hB7-1-hPD-L1 is largely driven by its 8.3 fold faster 2D on-rate, although its dissociation is more rapid as well (Figure 4.3D & E). Interestingly, B7-1-PD-L1 interactions are much weaker than PD-1-PD-L1 interactions, with a 37- and 49-fold $A_c K_a$ differences for human and murine, respectively. The differences in 2D parameters are much more profound than those previously estimated by SPR experiment [18], suggesting B7-1-PD-L1 interactions are not favored in the native cellular environment. Consistent

with this, mPD-L1-coated RBCs generated an adhesion frequency of above 50% when tested against activated CD8⁺ T cells from WT P14 mice, whereas negligible level of binding to cells from PD-1 KO P14 mice, despite the significant level of B7-1 expressed by both cells.

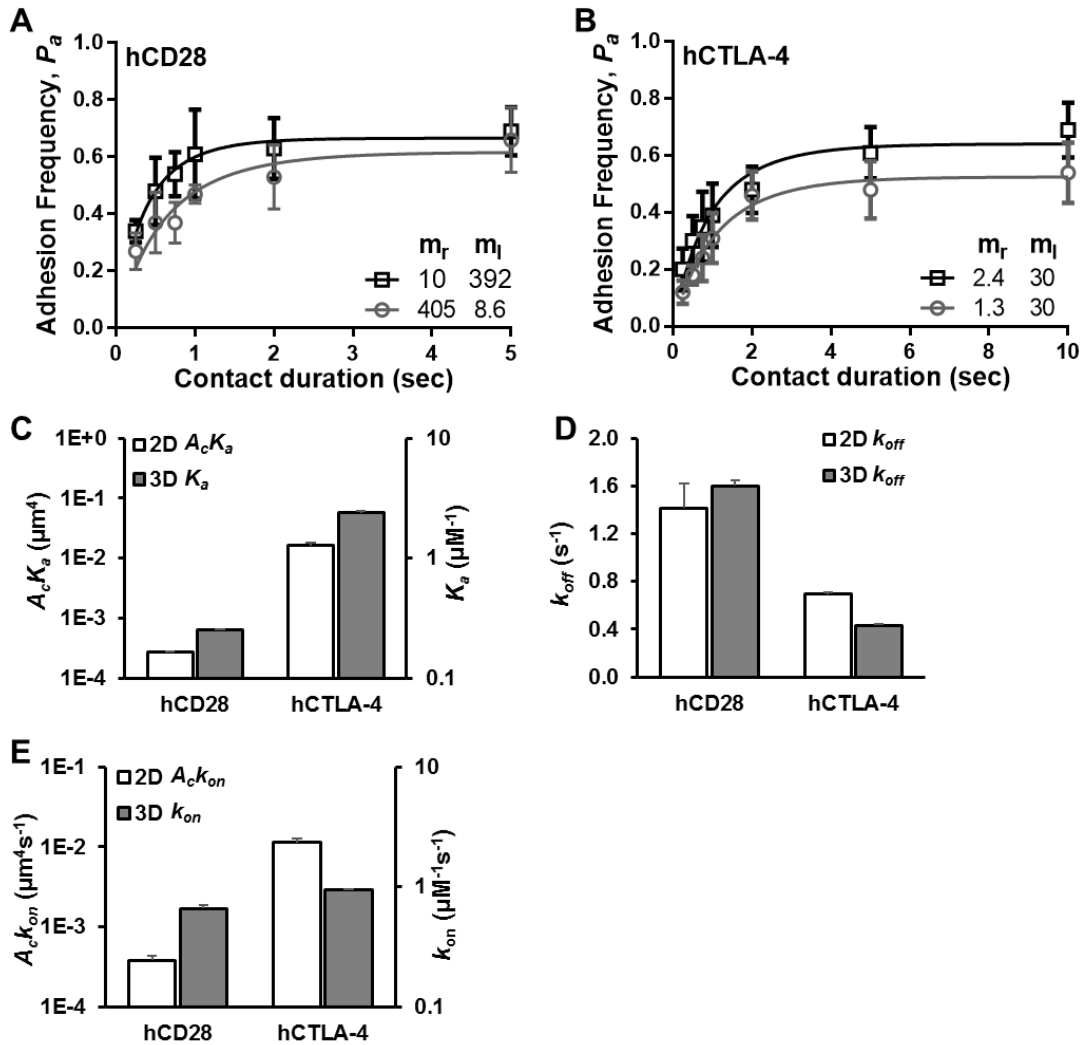


Figure 4.4: Comparison of 2D and 3D kinetics of human B7-1-CD28 and B7-1-CTLA-4 interactions. A) – B) Adhesion frequency curves of CHO cells expressing hB7-1 tested against RBCs coated with hCD28-Fc (A) or hCTLA-4-Fc (B). Each curve represents an independent measurement with different receptor and ligand densities. C) – E) 2D effective affinity ($A_c K_a$, C), 2D off-rate (k_{off} , D) and 2D on-rate ($A_c k_{on}$, E) were derived from data shown in A) and B) using Eqs. 1, 2 and 3. The corresponding 3D kinetics were replotted based on the previous study using the same protein constructs [83]. Data represent mean \pm SEM.

Table 4.1: Summary of 2D kinetic parameters.

CHO	Purified	2D A_cK_a (μm^4)	k_{off} (s^{-1})	2D A_cK_{on} ($\mu\text{m}^4\text{s}^{-1}$)
hPD-1	hPD-L1	$4.74 \pm 0.30 \times 10^{-4}$	0.50 ± 0.03	$2.24 \pm 0.17 \times 10^{-4}$
hPD-1	hPD-L2	$2.12 \pm 0.56 \times 10^{-3}$	0.30 ± 0.07	$5.55 \pm 0.23 \times 10^{-4}$
hB7-1	hPD-L1	$1.21 \pm 0.16 \times 10^{-5}$	1.31 ± 0.35	$1.52 \pm 0.22 \times 10^{-5}$
hB7-1	hCD28-Fc	$2.68 \pm 0.05 \times 10^{-4}$	1.41 ± 0.20	$3.78 \pm 0.53 \times 10^{-4}$
hB7-1	hCTLA-4-Fc	$1.63 \pm 0.21 \times 10^{-2}$	0.70 ± 0.02	$1.13 \pm 0.001 \times 10^{-2}$
mPD-1	mPD-L1	$1.69 \pm 0.51 \times 10^{-4}$	0.33 ± 0.02	$5.46 \pm 1.33 \times 10^{-5}$
mPD-1	mPD-L2	$1.63 \pm 0.34 \times 10^{-4}$	0.97 ± 0.05	$1.59 \pm 0.40 \times 10^{-4}$
mB7-1	mPD-L1	$3.47 \pm 1.25 \times 10^{-6}$	0.51 ± 0.03	$1.84 \pm 0.74 \times 10^{-6}$

4.2.4 2D interactions of human B7-1 with CD28 and CTLA-4

To better orient the 2D kinetics of the PD-1 ligand interactions, we analyzed the 2D interactions of hB7-1 with CD28 and CTLA-4, the most well studied interactions in the B7–CD28 family (Figure 4.4). One of the key mechanisms of CTLA-4 inhibiting T cell activation and function is via competing with CD28 in ligand binding and even depleting the ligand via trans-endocytosis [25]. The kinetic basis is manifested as the 10-fold higher 3D affinity for B7-1–CTLA-4 [83], which is further enhanced by the dimeric binding on the cell membrane [77, 127]. The 2D affinities follow the same trend, but display a 2-log difference ($2.68 \pm 0.05 \times 10^{-4}$ vs $1.63 \pm 0.21 \times 10^{-2} \mu\text{m}^4$). Given that low densities of B7-1 were used to reduce dimerization on membrane, the much larger difference in 2D affinity vs 3D affinity suggests the 2D binding of these two interactions are differentially regulated by the cellular environment. While the difference in 3D affinity was largely attributed to the smaller k_{off} of B7-1–CTLA-4, the 2D off-rates are different by only 2-fold. Instead, the 2D on-rate of B7-1–CTLA-4 is 50-fold higher than that of that of B7-1–CD28 (1.13 ± 0.001

$\times 10^{-2}$ vs $3.78 \pm 0.53 \times 10^{-4} \mu\text{m}^4\text{s}^{-1}$), accounting for the 2-log higher 2D affinity of CTLA-4.

4.3 Discussion

The critical role of PD-1 in maintaining peripheral T-cell tolerance and its key suppressive effect on exhausted T cells have made it a promising therapeutic targets for restoring T cell functions in a wide range of cancer and infectious diseases. To better understand the biological and biophysical mechanism underlying PD-1 or PD-L1 blockade, a spatiotemporal map of the molecular interactions involved is needed with particular focus on their kinetic properties in the cellular context, which have not been reported previously. We and others have shown in multiple molecular systems dramatic differences in binding kinetics measured in solution (3D) comparing with those of molecules expressed on the native cell membrane. For example, the 2D kinetics of TCR–pMHC spread a much wider dynamic range than 3D kinetics and correlate better with the functional potency of the pMHCs [10, 13, 119-121]. They are also sensitive to perturbations of the cellular environment such as inhibition of actin polymerization with Latrunculin A or disruption of membrane microdomains with cholesterol oxidase [10, 118]. Interestingly, we found in this study a fair agreement in trend between 2D and 3D kinetic parameters in comparing the two ligands interacting with PD-1 for both human and murine species. This is possibly due to the relatively simple structures – the PD-1 ectodomain consists of a single IgV domain and the ligands of an IgV and an IgC domain. In contrast, the TCR is a heterodimer of two immunoglobulin chains with non-covalent coupling to CD3 subunits through multiple interfaces, and thus its ligand-binding would be presumably more susceptible to regulations on the whole complex.

The 3D measurements of the dimeric PD-1–PD-ligand interactions using SPR display K_d values ranging from 0.01 μM to 0.8 μM [79-82], whereas the K_d for monomeric interactions were reported to be 2-8 μM [18]. Different from the weak binding properties revealed by the 3D measurements, our results identify PD-1–PD-ligand interactions in the middle if not the strong category. The overall effective 2D affinities of the four interactions (two ligands and two species) are comparable to that of TCR interacting with agonist pMHC, and that of strong interactions between LFA-1 and ICAM-1 (Figure 4.5). The relatively high 2D affinities are largely attributed to the fast on-rates, which lie in the similar tier of fast interactions like PSGL-1 with P-selectin or L-selection that facilitates leucocyte capture and rolling on vascular surface. Such enhanced 2D interactions provide a better kinetic basis for the potent inhibitory signaling these interactions trigger.

Interestingly, we found distinct binding kinetics for human vs murine interactions, as well as for PD-L1 vs PD-L2 of both species, which were also revealed by 3D studies [18, 79, 81]. These differential binding properties might be related to the structural differences reported earlier. Human PD-1 has a different positioning of the FG loop and also replaces the C'' stand with a flexible loop - both regions contribute to ligand binding as shown by NMR structure [18]. The recent structure of hPD-1–hPD-L1 complex further shows significant plasticity associate with the ligand binding of hPD-1 – the CC' loop that adopts an open conformation in apo-hPD-1 closes upon binding to hPD-L1, while the CC' loop of apo-mPD-1 already displays a close conformation [78]. Also, the two ligands may bind to the same receptor with distinct physical basis. Thermodynamic analysis reveal an entropically driven process for hPD-1–hPD-L1 binding, whereas a large enthalpic term for hPD-1–hPD-L2 interaction [18]. In addition to the distinct expression patterns of the two

ligands, the differences in binding kinetics provide another regulatory mechanism for their differential functions *in vivo*.

The discovery of B7-1–PD-L1 interaction further complicated the efforts to delineate the biophysical interactions and the biological functions of all the molecules involved, as both PD-L1 and B7-1 are found to be expressed on activated T cells as well as the opposing antigen-presenting cells. It has been shown functionally that B7-1–PD-L1 engagement triggers bidirectional inhibitory signaling and limits potentially pathogenic self-reactive T cell responses in a diabetic mouse model [82, 85]. The biophysical nature of this interaction remains controversial: early studies using dimeric proteins reporting similar binding avidity to that of PD-1–PD-L1 binding, whereas monomeric affinity was measured much lower [18, 80, 82]. Here our results show that the 2D A_cK_a of B7-1–PD-L1 binding is about 37-49 fold, 20-fold, or 3-log lower than that of PD-1–PD-L1 binding, B7-1–CD28 binding, or B7-1–CTLA-4 binding, respectively. The weak 2D affinity presumably partially accounts for its mild function *in vivo*.

Comparing the 2D vs 3D affinities of the PD-1/PD-L1 ligands/B7-1 system in this study also reveals the differential regulation of 2D interactions for various molecules by the cellular environment. Figure 4.5 summarizes the corresponding 2D and 3D affinities with the dotted line representing the transformation between 2D and 3D with certain confinement region σ according to the Bell model [128]. A smaller confinement region indicates more enhancement in 2D binding. Interestingly, all four PD-1 ligand interactions lie along the line of $\sigma = 3 \mu\text{m}$, suggesting a consistent level of enhancement of 2D binding. In contrast, there's more enhancement for B7-1–CTLA-4 than B7-1–CD28 ($\sigma < 3 \mu\text{m}$ vs $\sigma > 10 \mu\text{m}$), further strengthening the kinetic basis of CTLA-4 inhibition via ligand

competition. Finally, the B7-1–PD-L1 interactions show the least enhancement with much lower 2D affinity on the list, again implying less favorable interactions in vivo.

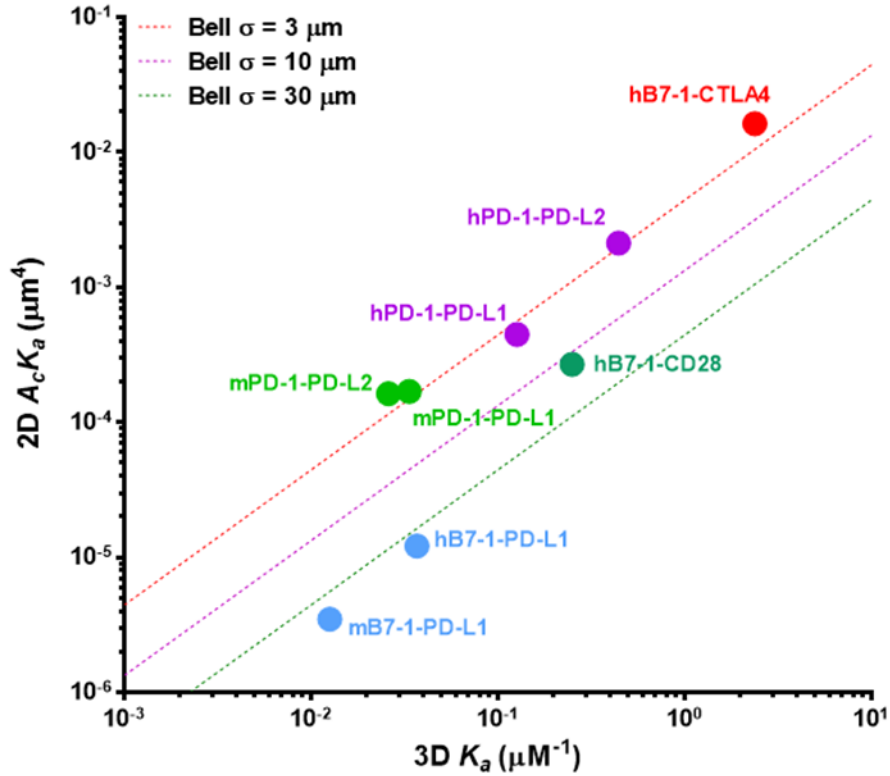


Figure 4.5: Comparison of 2D and 3D affinities reveals differential enhancement of 2D affinities by the cellular environment. Dotted lines represent the transformation between 2D and 3D affinities according to Bell model: $2D K_d = \sigma \times 3D K_d$, assuming $A_c = 8 \mu\text{m}^2$.

CHAPTER 5

PD-1 SUPPRESSES T-CELL ANTIGEN RECOGNITION BY DISRUPTING THE TCR-CD8 COOPERATIVE BINDING TO COGNATE PMHC

5.1 Introduction

Despite the success of targeting PD-1 in modulating T cell functions, the mechanism of how PD-1 suppresses antigen-specific T cell responses is not fully resolved. The major part of our current understanding includes the phosphorylation of the ITIM and ITSM when PD-1 and TCR are co-engaged with their respective ligands, the subsequent recruitment of SHP-1 and/or SHP-2, and the dephosphorylation of a panel of signaling molecules downstream of TCR and CD28 [41, 67-70]. The inhibition is suggested to be fast and early: SHP-2 recruitment to PD-1 was detected in AND T hybridomas within 8 sec following stimulation by MCC₈₈₋₁₀₃ pulsed DC-1 cells [69]; PD-1 inhibits the phosphorylation of CD3 ζ and ZAP-70 [68, 69], one of the immediate steps following TCR triggering. Yet, it remains unknown whether PD-1 negative signaling could perturb the first layer of the activating signal – antigen recognition.

Antigen recognition by the TCR initiates the signaling cascades leading to T cell activation and its effector functions, a process that depends on the two-dimensional (2D) kinetics of TCR–pMHC interactions, as well as the bond dynamics under force [10, 13, 115, 119, 120]. Such 2D interactions are subjected to the regulation of cellular environment, providing the first layer of regulation of antigen recognition [10, 118, 120]. Moreover, enhancement brought by co-receptor engagement with pMHC is required for

the full-strength interaction and function [15, 129]. In particular, whereas CD8–pMHC alone displays a weak 2D affinity [9], the contribution of TCR–CD8–pMHC trimolecular interaction through cooperation between TCR and CD8 is significant and is correlated with the enhancement in cytokine production [12, 13]. More importantly, such cooperative binding is induced by the initial TCR signaling and Lck [12, 14], suggesting it as an adjustable process susceptible to perturbations of the TCR proximal signaling components involved.

Here using activated T cells, we confirmed the TCR–CD8 cooperative binding-induced enhancement of bond number and bond lifetime, which was eliminated when CD8 binding to MHC was abolished or Lck was inhibited. When TCR–CD8 and PD-1 were co-engaged with their respective ligands, we observed fewer molecular bonds than predicted from independent binding of the two groups, a phenomenon similar to “negative cooperativity”. The reduction in bond number is associated with more occurrence of short-lived than long-lived bond lifetime events, corresponding to the distinct force-lifetime response of PD-1 and TCR–CD8–pMHC, respectively, as revealed by force spectroscopy. Moreover, the negative cooperativity shown in bond number and bond lifetime became absent without CD8 binding or with Lck inhibition, suggesting that the negative cooperativity represents the suppression of the positive cooperative binding of TCR and CD8 to cognate pMHC. Furthermore, perturbing the signaling components downstream of PD-1 demonstrated that the suppression depends on SHP-2 activity. These data reveal a new mechanism of fine-tuning antigen recognition by PD-1 via a “binding-signaling-binding” process targeting the enhancement by CD8.

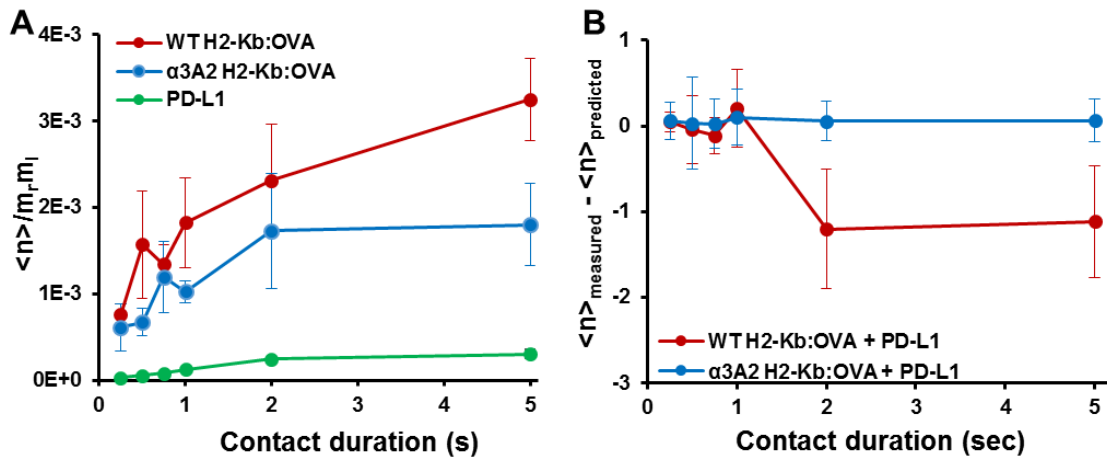
5.2 Results

5.2.1 Reduced formation of molecular bonds (negative cooperativity) with co-engagement of TCR, CD8 and PD-1

Previous work from our lab has demonstrated the cooperative binding of TCR and CD8 to cognate pMHC in naïve T cells, which manifests as a step increase in binding of OT-I T cells to H2-K^b:OVA coated RBCs at contact duration of 1 sec and longer [12]. The gain of binding corresponds to the formation of TCR–CD8–pMHC trimolecular bond, and depends on the initial triggering of TCR as well as Src family kinase, Lck and/or Fyn [12]. To analyze the potential interplay between activating (TCR–CD8–pMHC) and inhibitory (PD-1–PD-L1) interactions on activated T cells, we started from characterizing the 2D interactions of single species and comparing their capacity of bond formation, which is the total bond number normalized by the product of receptor and ligand densities representing the approximate of 2D affinity/avidity at plateau. Using activated OT-I T cells, we observed more bonds formed with wild type H2-K^b:OVA than with α 3A2 H2-K^b:OVA, a mutant with its α 3 domain replaced by that of HLA-A2 and thus abolishes CD8 binding (Figure 5.1A). Moreover, unlike TCR–pMHC binding alone (α 3A2 H2-K^b:OVA) that plateaus at $t_c > 2$ sec, that with CD8 binding (WT H2-K^b:OVA) continues to increase with prolonged contact duration, suggesting further enhancement on the TCR–CD8–pMHC bond formation on activated T cells. In contrast, the 2D affinity of PD-1–PD-L1 is 7-fold lower than that of OT-I TCR interacting with α 3A2 H2-K^b:OVA on activated OT-I T cells (Figure 5.1A), which is similar as that was measured using PD-1 expressed by CHO cells.

We then analyzed binding cooperativity by coating RBCs with a mixture of pMHC and PD-L1. The predicted total bond number is the simple sum of bonds formed by each

species, assuming the two interactions are independent and concurrent [116, 117]. For the mixture of $\alpha 3A2$ H2-K^b:OVA and PD-L1, the actually measured bond number agrees well with the prediction at both short and long contact durations, suggesting no interplay between the TCR–pMHC and PD-1–PD-L1 at the level of receptor–ligand binding (Figure 5.1B). Similarly, co-presenting WT H2-K^b:OVA and PD-L1 at contact duration of 1 sec or shorter also shows no significant difference in total bond number between predicted and measured. In contrast, the measured bond number is smaller than predicted at $t_c = 2$ sec and

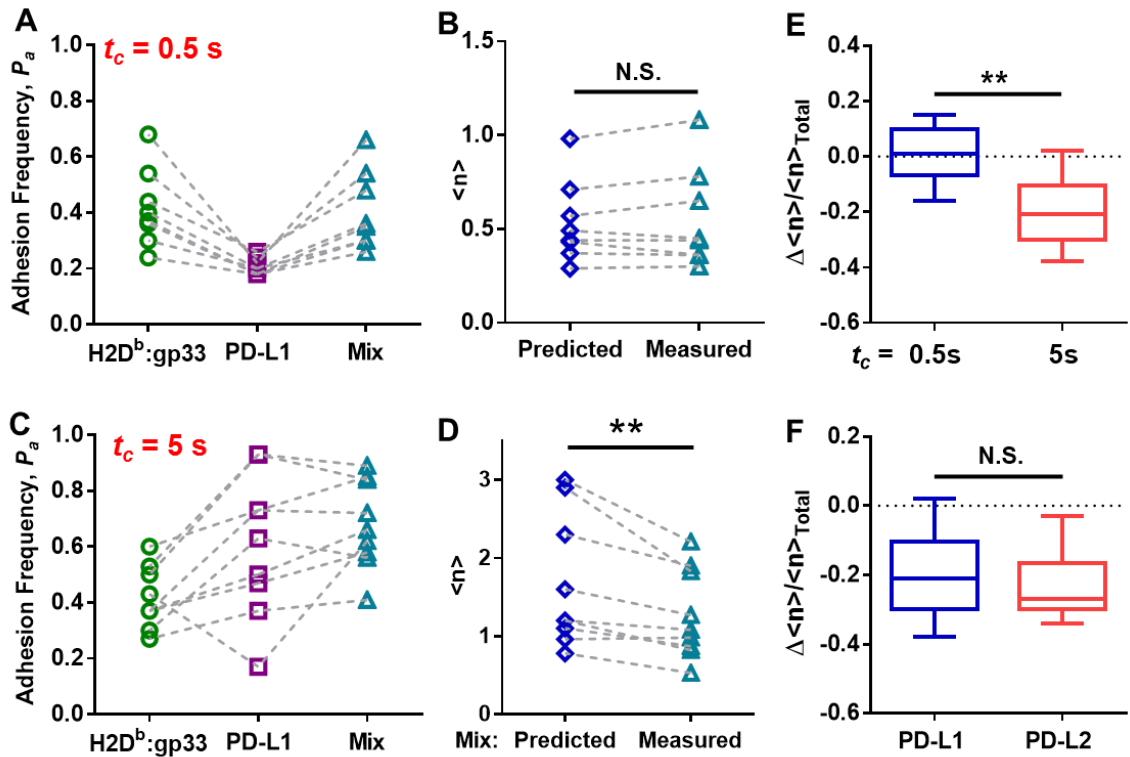


5 sec, a “negative cooperativity” indicating reduced bond formation (Figure 5.1B).

Figure 5.1: 2D kinetic analysis reveals reduced bond number with the co-engagement of TCR–CD8 and PD-1 in the OT-I/OVA system. **A)** Total bond number normalized by molecular densities tested using activated OT-I CD8⁺ T cells against RBCs coated with WT H2-K^b:OVA (red), $\alpha 3A2$ H2-K^b:OVA (blue), or PD-L1 (green) with various contact durations (t_c). **B)** Differences in average bond number between predicted and measured for 2D cooperative binding analysis using a mixture of WT H2-K^b:OVA (red) and PD-L1, or $\alpha 3A2$ H2-K^b:OVA and PD-L1 (blue).

To test if the same negative cooperativity also holds true for other TCR–CD8–pMHC systems, we conducted the same analysis using activated CD8⁺ T cells from P14 transgenic mice, which recognizes H2-D^b presenting gp33 peptide from LCMV. An improved protocol that tests the same T cell against three randomized RBCs coated with either single or mixed ligands was adopted to minimize the cell-cell variation among

groups (Figures 5.2A & C). This also enabled comparison of predicted versus measured bond number on a per-cell basis. Similar as in the OT-I system, P14 T cells show no statistical difference between predicted and measured bond number at short contact duration ($t_c = 0.5$ sec, Figure 5.2B), but significantly reduced bond formation at long contact duration ($t_c = 5$ sec, Figure 5.2C). The averaged percentage of reduction is $\sim 20\%$ at 5 sec (Figure 5.2E), which is about the same as using another ligand, PD-L2 (Figure



5.2F).

Figure 5.2: 2D kinetic analysis reveals reduced bond number with the co-engagement of TCR-CD8 and PD-1 in the P14/gp33 system. A) & C) Representative adhesion frequency (P_a) of individual activated P14 CD8⁺ T cells binding to RBCs coated with WT H2-D^b:gp33, PD-L1, or a mixture of WT H2-D^b:gp33 and PD-L1 at contact duration of 0.5 sec (A) or 5 sec (C). The same T cell tested against three types of RBCs is connected with dashed lines. B) & D) Comparison of predicted and measured average bond number $\langle n \rangle$ from A) and C), respectively. E) Normalized bond reduction ($\Delta \langle n \rangle / \langle n \rangle_{total}$) from B) and D). F) Normalized bond reduction from cooperativity analysis using WT H2-D^b:gp33 and PD-L1 vs WT H2-D^b:gp33 and PD-L2. For box-whisker plot, the center line labels median, the box contains the two middle quantiles, and the whiskers mark the min and the max.

To confirm that the reduction of bond number is mediated by PD-1 ligand interactions instead of increased complexity of co-presentation and co-detection of both ligands, we tested CD8⁺ T cell from PD-1 KO P14 mice against RBCs with the same ligand coatings as in analysis above. As expected, PD-L1 coated RBCs generated only negligible level of binding at $t_c = 5$ sec (Figure 5.3A), confirming the specific presentation of PD-L1 to PD-1. Moreover, no statistical significance was found between predicted and measured bond number when PD-1–PD-L1 interaction was abolished (Figure 5.3B & C). Together these data demonstrate a negative cooperativity between TCR, CD8, and PD-1 at the level of molecular binding.

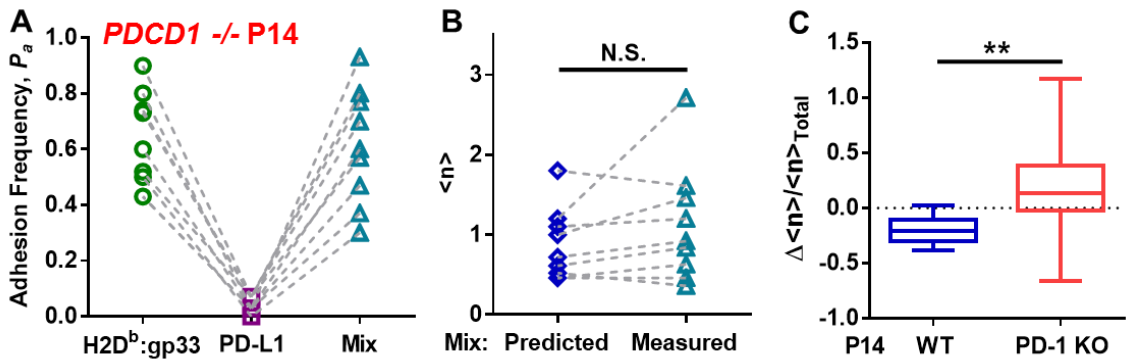


Figure 5.3: The TCR–CD8 and PD-1 negative cooperativity depends on PD-1. **A)** Representative adhesion frequency (P_a) of individual activated *PDCD1*^{-/-} P14 CD8⁺ T cells binding to RBCs coated with WT H2-D^b:gp33, PD-L1, or a mixture of WT H2-D^b:gp33 and PD-L1 at contact duration of 5 sec. **B)** Comparison of predicted and measured average bond number $\langle n \rangle$ from A). **C)** Comparison of normalized bond reduction of T cells from WT P14 vs *PDCD1*^{-/-} P14 mice.

5.2.2 The negative cooperativity depends on PD-1 negative signals

Different from the conventional binding cooperativity, where binding of a second molecule (pair) is physically affected by that of the first molecule (pair), 2D cooperative binding of T cell surface molecules can represent direct physical interplay on the cell membrane, and/or inside-out regulation of molecular binding by the signaling events downstream of these interactions (“binding-signaling-binding”). The fact that the negative

cooperativity was observed with long contact duration suggests a temporal requirement most likely involving the crosstalk of these two signaling axis. To test the signaling dependency on PD-1, we perturbed the system with pharmacological inhibition of SHP-1 and SHP-2, the two major signaling candidates downstream of PD-1.

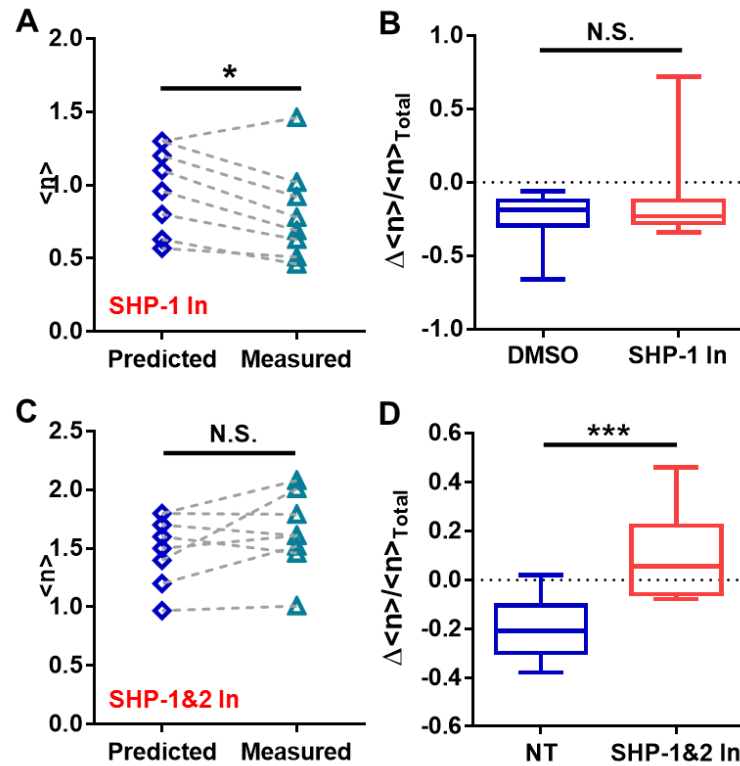


Figure 5.4: The TCR–CD8 and PD-1 negative cooperativity is mediated by SHP-2 not SHP-1. A) & C) Comparison of predicted and measured average bond number $\langle n \rangle$ under treatment with 50 μ M PTP inhibitor I (A) or 20 μ M NSC87877 (C). **B) & D)** Comparison of normalized bond reduction ($\Delta \langle n \rangle / \langle n \rangle_{total}$) in control vs drug treated groups.

Inhibition of SHP-1 with 50 μ M PTP inhibitor I did not affect the observation of the negative cooperativity (Figure 5.4A). There is also no significant difference in the percentage of bond reduction comparing with DMSO control (Figure 5.4B). In contrast, inhibiting both SHP-1 and SHP-2 with 20 μ M NSC87877 eliminated the negative cooperativity by restoring the measured bond number to a similar level as predicted (Figures 5.4C & D). Moreover, neither of the two treatments affected the 2D

avidity/affinity of TCR–CD8 binding to pMHC or PD-1 binding to PD-L1 alone, as assessed from RBCs coated with individual ligand species (Figure 5.5). Therefore, the negative cooperativity is more likely to be a “binding-signaling-binding” process, which at least in part, relies on the PD-1 negative signaling mediated by SHP-2.

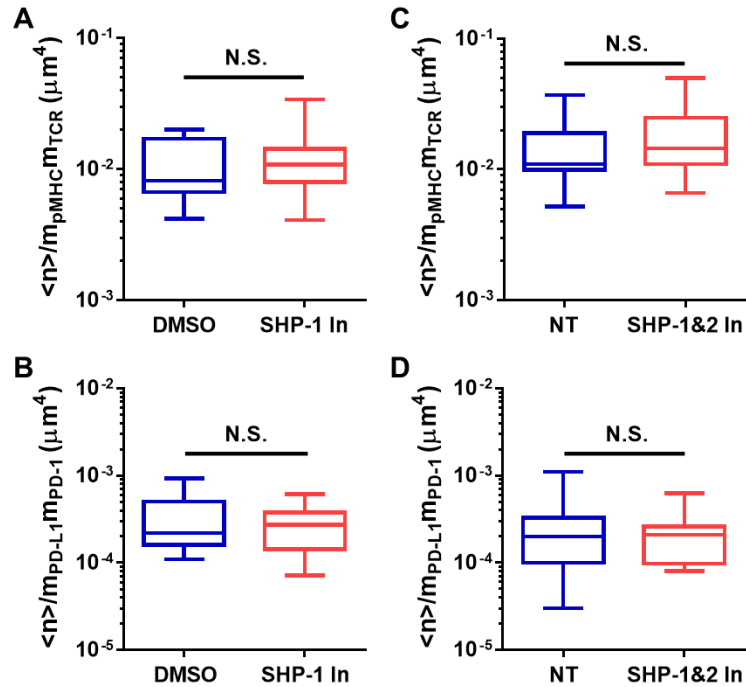


Figure 5.5: TCR–CD8 binding to pMHC and PD-1 binding to PD-L1 were not affected by SHP-1 or SHP-2 inhibition. A) & C) Normalized bond number $\langle n \rangle / m_{TCR} m_{pMHC}$ for TCR–CD8–pMHC interactions in control vs drug-treated groups. B) & D) Normalized bond number $\langle n \rangle / m_{PD-1} m_{PD-L1}$ for PD-1–PD-L1 interactions in control vs drug-treated groups.

The initiation of PD-1 signaling depends on the phosphorylation of its ITIM and/or ITSM [67, 68], possibly by Src family kinases, such as Lck and Fyn. The phosphorylation and subsequent SHP-2 recruitment can be greatly enhanced with the presence of TCR activating signals, reflecting the negative feedback nature of the PD-1 pathway. To block the activating input, we inhibited Lck with 2 μM 7-Cyclopentyl-5-(4-phenoxyphenyl)-7H-pyrrolo[2,3-d]pyrimidin-4-ylamine. This treatment abolished the difference between predicted and measured bond number and thus eliminated the negative cooperativity

(Figures 5.6A & B). Moreover, inhibition of Lck reduced T cell binding to WT H2-Db:gp33 by ~47%, while leaving PD-1–PD-L1 binding unaffected (Figures 5.6C & D). This is consistent with our previous observation that TCR–CD8 cooperative binding to cognate pMHC is Lck and/or Fyn dependent. Therefore, the elimination of negative cooperativity by Lck inhibition could be attributed to either the impaired positive input on PD-1, or the reduced TCR–CD8–pMHC trimolecular bonds, or both.

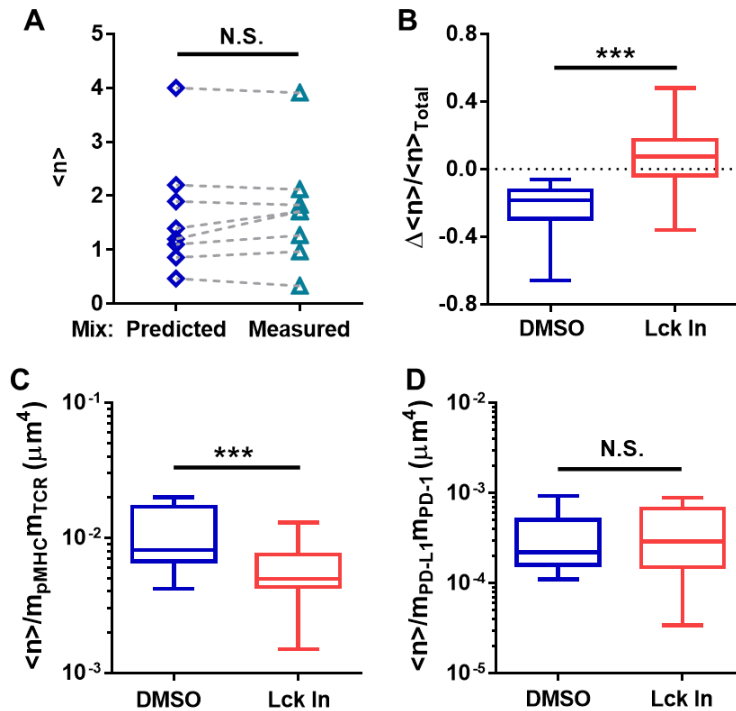


Figure 5.6: The TCR–CD8 and PD-1 negative cooperativity depends on Lck activity. A) Predicted vs measured average bond number $\langle n \rangle$ with Lck inhibition. B) Normalized bond reduction ($\Delta \langle n \rangle / \langle n \rangle_{total}$) in control vs drug-treated group. C) & D) Normalized bond number $\langle n \rangle / m_r m_l$ for TCR–CD8–pMHC (C) and PD–PD-L1 (D) interactions in control and drug-treated groups.

5.2.3 The negative cooperativity depends on CD8 binding to pMHC

The absence of negative cooperativity when using $\alpha 3A2$ H2-K^b:OVA or inhibiting Lck suggests an underlying mechanism involving CD8–pMHC binding, and especially the TCR–CD8–pMHC trimolecular bond formation. To confirm this, we analyzed the binding

cooperativity using P14 T cells and $\alpha 3A2$ H2-D^b:gp33, the same mutation that abolishes CD8 binding (Figure 5.7). The normalized bond number was reduced by ~57% comparing to using WT H2-D^b:gp33, further confirming the significant contribution of TCR-CD8-pMHC in the total number of bonds formed (Figure 5.7A). Similar as in the OT-I system, negative cooperativity was not observed with the mutant H2-D^b (Figures 5.7B & C).

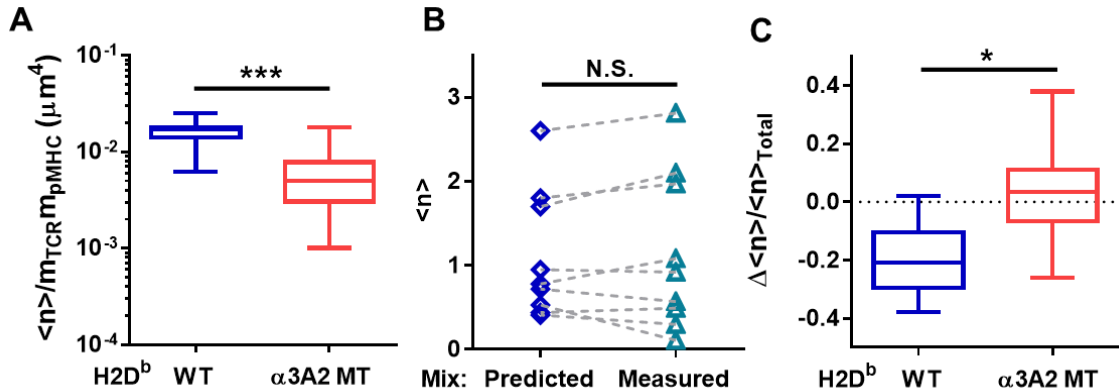


Figure 5.7: The negative cooperativity is eliminated when CD8-pMHC interaction is abolished. **A)** Normalized bond number $\langle n \rangle / m_{TCR} m_{pMHC}$ measured from using WT H2-D^b:gp33 vs $\alpha 3A2$ H2-D^b:gp33. **B)** Predicted vs measured average bond number $\langle n \rangle$ in binding cooperativity analysis of $\alpha 3A2$ H2-D^b:gp33 and PD-L1. **C)** Comparison of normalized bond reduction ($\Delta \langle n \rangle / \langle n \rangle_{total}$) in cooperativity analysis using WT H2-D^b:gp33 and PD-L1 vs $\alpha 3A2$ H2-D^b:gp33 and PD-L1.

5.2.4 Force spectroscopy reveals distinct force-lifetime responses of TCR-pMHC, TCR-CD8-pMHC and PD-1-PD-L1 bonds of the P14/gp33 system

Although the dependence of negative cooperativity on PD-1, CD8-pMHC binding, and the positive and negative signaling was confirmed, the detailed mechanism is masked by the incapability of the binding frequency-based analysis to dissect the molecular bonds involved. To improve the resolution, we applied biomembrane force probe-based force spectroscopic analysis, where additional bond signatures (e.g. force-lifetime response) are examined [115, 119, 130]. Similar as in the cooperativity analysis of bond number, force-

lifetime responses of individual interactions were characterized first with beads presenting single ligand species.

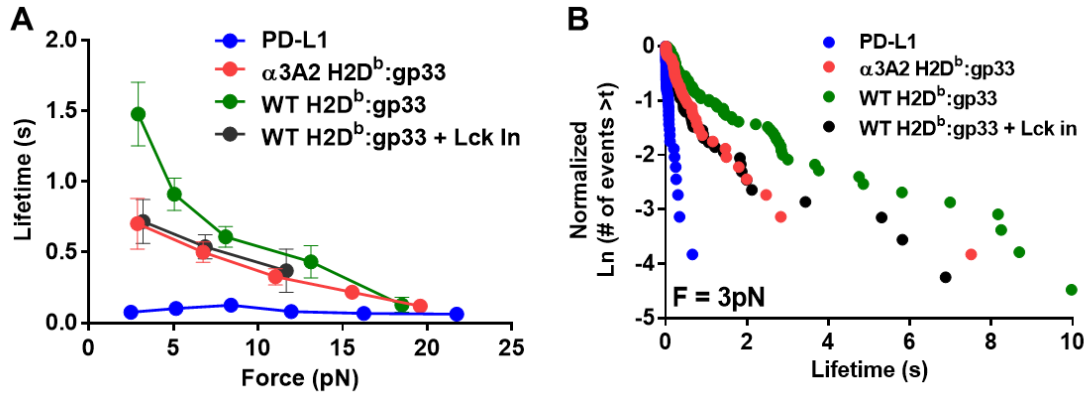


Figure 5.8: Force spectroscopy reveals distinct force-lifetime responses of TCR–pMHC, TCR–CD8–pMHC and PD–1–PD–L1 bonds of the P14/gp33 system. A) Force-lifetime spectra of PD–1–PD–L1, P14 TCR– $\alpha 3A2$ H2–D^b:gp33 and P14 TCR–WT H2–D^b:gp33 molecular bonds with or without Lck inhibition measured using biomembrane force probe. **B)** Bond lifetime distributions of the molecular interactions in A) at 3 pN.

The overall lifetime response to forces applied on single P14 TCR– $\alpha 3A2$ H2–D^b:gp33 bonds displays a monotonic decay with increasing force level ranging from ~ 1 pN to ~ 25 pN (Figure 5.8A). The average bond lifetime is 0.70 sec at a mean clamping force of ~ 3 pN. Comparing with this TCR–pMHC interaction alone, adding CD8 binding by using the WT H2–D^b:gp33 significantly prolongs bond lifetime especially at low forces (1.48 sec vs 0.70 sec at 3pN, Figure 5.8A), which corresponds to the shift of the histogram towards longer lifetime (Figure 5.8B). The mean lifetime in this case represents the weighted sum of three bond species: TCR–pMHC, CD8–pMHC, and TCR–CD8–pMHC, with the weight determined by their binding kinetics and molecular densities. Since the 2D affinity of CD8 binding to H2–D^b is 4 logs lower than that of P14 TCR– $\alpha 3A2$ H2–D^b:gp33, its contribution to the overall mean lifetime is negligible. This is further supported by the observation that Lck inhibition reduced the bond lifetime to the level of P14 TCR– $\alpha 3A2$ H2–D^b:gp33 interaction alone, as shown in both the identical mean lifetimes across multiple

levels of force, as well as the overlapping histogram at 3 pN. Assuming a ~1:1 mixture of TCR-pMHC and TCR-CD8-pMHC bonds as suggested by the kinetic measurement in the binding frequency assay, the mean lifetime of TCR-CD8-pMHC trimolecular bond at 3 pN is estimated to be ~2.26 sec, a great enhancement (>3 fold) of the TCR-pMHC interaction alone. Overall, the enhancement decreases with increasing force, suggesting the dominance of TCR-pMHC dissociation in the rupture of the trimolecular bonds. In sharp contrast, the bond lifetime for PD-1-PD-L1 is much shorter than that of P14 TCR- α 3A2 H2-D^b:gp33 across a range of forces, with the largest differences seen at low forces (0.08 sec vs 0.70 sec at 3 pN, Figure 5.8A). Such force-lifetime responses would serve as ideal signatures to estimate the altered occurrence of short vs long bond lifetime events in the case where both ligands are allowed to engage.

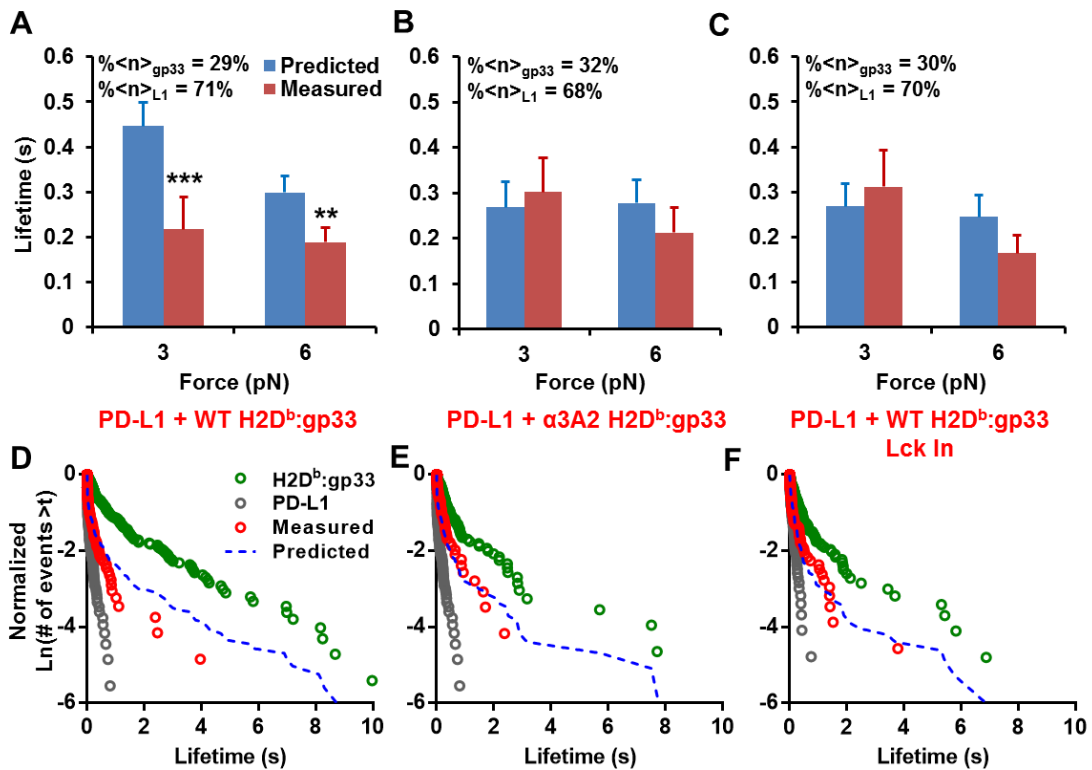


Figure 5.9: The average bond lifetime is reduced when PD-L1 is co-engaged with WT H2-D^b:gp33 not the α 3A2 mutant. Predicted vs measured average bond lifetime $\langle t \rangle$ (A,

B, & C) and their distributions (D, E, & F) at 3 pN in binding cooperativity analysis of the interactions indicated. Data are presented as mean \pm SEM.

5.2.5 Force-lifetime spectroscopy reveals TCR–CD8–pMHC as the missing bond species

We then extended the cooperativity analysis to the lifetime events collected with mixture coating. Similar as in the bond number cooperativity analysis, the predicted mean bond lifetime (distribution) is the weight sum of bond lifetimes (distributions) from single ligand presentation assuming the occurrence of each receptor-ligand species does not affect the other(s). Therefore, altered fractions of mixed long and short bond species is discernable from the changes in the measured mean lifetime (distribution) comparing with prediction. Indeed, when WT H2-D^b:gp33 and PD-L1 were mixed giving a bond ratio of 29% vs 71% as determined by their binding kinetics and molecular densities, the measured mean lifetimes are significantly shorter than predicted ones (0.45 sec vs 0.22 sec at 3 pN, and 0.30 sec vs 0.19 sec at 6 pN, Figure 5.9A). The histogram of measured lifetime events were also left-shifted comparing to the predicted distribution (Figure 5.9D). Considering the dramatic lifetime differences of the bond species involved, the reduced mean bond lifetime suggests that the actual fraction of long lifetime events (TCR–pMHC and/or TCR–CD8–pMHC) is lower than the predicted. Applying the same analysis to the mixture of α 3A2 H2-D^b:gp33 and PD-L1 shows no significant difference between predicted and measure mean bond lifetimes or their distributions (Figures 5.9B & E), implying that the reduced fraction of long lifetime events is most likely attributed to the TCR–CD8–pMHC trimolecular bonds. This is further supported by co-presentation of WT H2-D^b:gp33 and PD-L1 with Lck inhibition. Consistent with its abolishment of TCR–CD8–pMHC trimolecular bond formation and the negative cooperativity in bond number, the differences

in mean bond lifetime and lifetime distributions are also eliminated (Figures 5.9C & F). Together, these data further reveal that the cooperative binding of TCR and CD8 to pMHC is suppressed with the co-engagement of PD-1 by PD-L1.

5.3 Discussion

Lying in the center of T-cell activation is the triggering of TCR by antigenic peptide-bound MHC, which, according to our and others' studies, is largely determined by the *in situ* kinetic and mechanical properties of this interaction [10, 13, 115, 119, 120]. However, the balance between its sensitivity and robustness embedded in the molecular structures at single receptor level is insufficient to achieve the nearly perfect solution optimized over evolution, as atomicity of single receptors is subjected to various perturbations/noise that could easily overwhelm the default kinetic and mechanical modes. Therefore, collective behaviors are required to process the information flow with entangled crosstalk. CD8, as a co-receptor of TCR in pMHC binding, is one of such key coordinated events in TCR triggering, and also one of the earliest [11, 129]. CD8 binding stabilizes TCR–pMHC interaction and also brings Lck to the proximity of TCR–CD3 complex, which amplifies TCR signaling [129, 131]. In a finer temporal resolution, this event is a consequence of the initial TCR triggering: it displays a positive cooperativity depending on TCR–pMHC interaction and Lck activities [12, 13]. In this study, we have recapitulated this cooperative binding using activated CD8⁺ OT-I and P14 T cells. The enhancement manifests as ~1-fold increase in average bond number and ~2-fold increase in average bond lifetime, both were eliminated under Lck inhibition. Such signaling-dependent enhancement is wired to TCR antigen recognition as a significant component subject to the potential regulations of costimulatory/coinhibitory signals from other pathways.

Albeit the promising outcome of targeting PD-1–PD-L1 in treating tumor and other diseases [33, 42], the fundamental mechanisms of PD-1 function remain unclear. Previous studies reveal the essential role of the phosphorylation of its ITSM and the subsequent recruitment of SHP-1 and SHP-2, which attenuates the TCR signaling by dephosphorylating a panel of its downstream signaling molecules [41, 67-69], and thereby suppresses the overall cellular function, such as proliferation and cytokine production [59]. In this study, we further analyzed such interplay at the level of ligand binding and observed reduced bond formation when PD-1 and TCR–CD8 were co-engaged with their respective ligand, an apparent “negative cooperativity”. By using PD-1 KO P14 T cells while keeping the same ligand complexity of RBC coating, we confirmed that the negative cooperativity is mediated by the PD-1–PD-L1 interaction. Moreover, it also depends on the engagement of CD8 by pMHC, according to its absence when CD8 binding to pMHC was abolished by either using $\alpha 3A2$ mutant MHC or Lck inhibition. To further dissect the underlying mechanism, we applied force spectroscopic analysis of single bonds from individual interactions and mixed interactions. Quite surprisingly, dramatic differences were observed in their force-bond lifetime responses: 0.08 sec@3 pN for PD-1–PD-L1 vs 0.70 sec @ 3 pN for P14 TCR– $\alpha 3A2$ H2-D^b:gp33 vs 1.48 sec @ 3 pN with additional CD8 contribution. Cooperativity analysis of average bond lifetime reveals that the fraction of long lifetime events became lower than predicted when PD-1 and TCR–CD8 were co-engaged, but unaffected when CD8 contribution was abolished by mutant MHC or Lck inhibition. The skewed occurrence of more short lifetime events suggests the suppression of TCR–CD8–pMHC trimolecular interaction by PD-1.

It has been suggested that PD-1 inhibition of TCR signaling occurs at very early stage with fast responses. PD-1 suppresses the CD3 ζ phosphorylation and ZAP-70 microcluster formation and its phosphorylation [68, 69, 132], the upstream signaling steps that could be detected within 10 sec upon TCR stimulation [133]. Co-localization of PD-1 to TCR microclusters was observed as early as 20 sec following AND-Tg CD4⁺ T cells landing onto lipid bilayer containing both I-E^k:MCC₈₈₋₁₀₃ and PD-L1 [69]. The recruitment of SHP-2 by PD-1 was also detected at 8 sec upon DC stimulation [69]. These events shed light to the spatiotemporal pattern of the upstream negative regulation of the TCR pathway by PD-1. Considering the very short experimental timescale precisely controlled to the initiation and early accumulation of positive and negative signals, the negative cooperativity between PD-1 and TCR–CD8 represents an immediate feedback circuit targeting the very first step of T cell activation – the antigen recognition. The mechanism of this suppression, which is partially uncovered by this study as SHP-2 dependent, still remain elusive. A key target in the proximal signalosome might be Lck, whose activity is highly variable among auto-inhibited, primed, and activated states, and whose localization is dynamically transited among cytosol, membrane-associated pool and co-receptor-associated pool [134]. We have reported that the TCR–CD8 cooperative binding not only depends on Lck enzymatic activity, but its association with CD8 as well [14]. Moreover, the TCR–CD8 cooperative binding is also associated with the recruitment of CD8 to TCR–CD3 [14]. Therefore, one possible explanation involves 1) initial TCR triggering and signaling involving non-CD8 associated Lck, 2) activation of CD8-associated Lck (and other signaling/adaptor molecules) and/or binding of activated Lck to CD8, 3) translocation of CD8 to CD3 via Lck bridge that allows for its engagement with MHC with high affinity,

and 4) SHP-2 mediated PD-1 negative signals suppress this process by dephosphorylating Lck or CD3 ITAMs. It is unlikely that colocalization of PD-1 and TCR-CD8 is required, since PD-1 suppression was observed with both diffusible and immobilized ligand, and also very low level of PD-1 expression is able to suppress the TCR-triggered Ca^{2+} flux and cytokine production [75]. From a kinetic perspective it is an efficient and safe means of suppression, because decreasing the capability of CD8 binding could significantly reduce the quantity (bond number) and quality (bond lifetime) of antigen stimulation, but still keep the TCR-determined specificity unaffected. Biologically, this represents a new mechanism of PD-1 function and an example of fine-tuning of antigen recognition via a “binding-signaling-binding” process integrating positive and negative signals triggered by TCR and coinhibitory receptors, respectively.

CHAPTER 6

IDENTIFICATION OF CD222 AS A NOVEL BINDING PARTNER FOR HUMAN PD-L1

6.1 Introduction

It has long been proposed that PD-L1 and PD-L2 may have additional receptors other than PD-1. Back to as early as their discoveries, PD-L1 and PD-L2 were reported to have both costimulatory [34, 39] and coinhibitory [35, 38] functions. As increasing evidences indicating the coinhibitory role of PD-1 on T cells and B cells [41, 135, 136], the costimulatory functions were attributed to interactions of these two ligands with unknown molecules, a hypothesis strongly supported by the fact that mutant forms of PD-L1 or PD-L2 that fail to interact with PD-1 can still costimulate T cells from normal or PD-1-deficient mice [48]. Hunting for tentative binding partners ever since has added new members and interactions to the B7-CD28 family. Interaction between PD-L1 and B7-1 was reported to deliver bidirectional inhibitory signals to T cells, which was also a result of searching for additional receptors of B7-1/B7-2 [82]. Bioinformatics analysis for PD-1 homologs lead to the discovery of PD-1H [137] (also named VISTA in an independent finding [138]), although it does not interact with either PD-L1 or PD-L2. The most recent one was PD-L2 binding to RGMb, an interaction promotes respiratory tolerance by facilitating the initial T cell expansion in draining lymph nodes [86].

In this study, we discovered unknown molecule(s) on PD-1 and B7-1 negative cells that bind to hPD-L1 but not hPD-L2, which was then identified and validated to be CD222. Interaction between hPD-L1 and CD222 consists of both carbohydrate-lectin binding and protein-protein binding components with the apparent 3D affinity and 2D avidity both

stronger than that of hPD-L1–PD-1. Most importantly, direct competition between CD222 and PD-1 was observed for hPD-L1 binding, suggesting a potential role of CD222 in modulating the PD-1–hPD-L1 axis. This novel interaction will lead to vast opportunities to explore its functions in various cell types and context, especially in cancer immunotherapy, where the interaction could be blocked by anti-PD-L1 therapeutic antibodies.

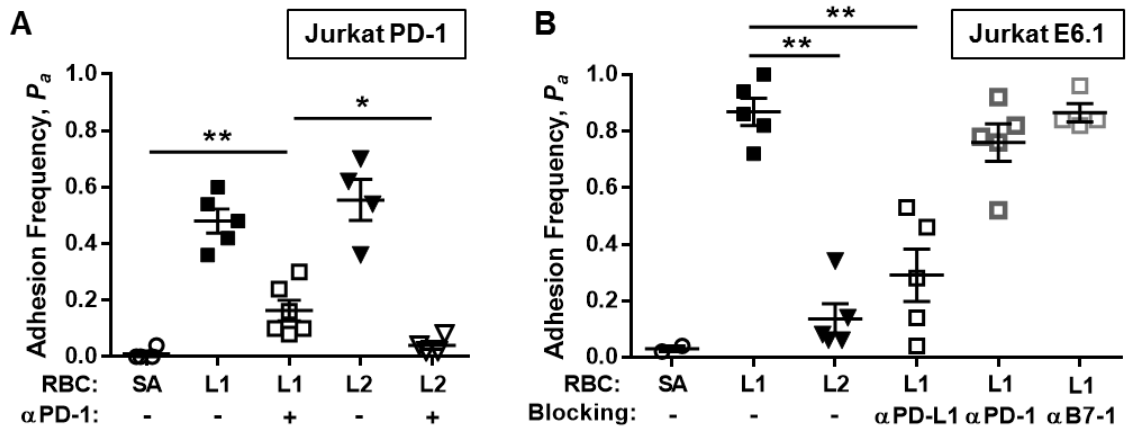


Figure 6.1: Specific binding between hPD-L1 and Jurkat cells is independent of PD-1 or B7-1. A) Anti-PD-1 abolished PD-1 Jurkat cells binding to hPD-L2 but not hPD-L1. **B)** Plain Jurkat cells (clone E6.1) binds specifically to hPD-L1. Binding was suppressed by anti-PD-L1 but not anti-PD-1 or anti-B7-1.

6.2 Results

6.2.1 The existence of additional binding partner(s) for hPD-L1

In the 2D kinetic analysis of hPD-1-PD-ligand interactions, we detected PD-1 overexpressing Jurkat cells binding to hPD-L1 coated RBCs even with the presence of anti-PD-1 blocking antibody, which abolished the binding between the same Jurkat cells and hPD-L2 coated RBCs (Figure 6.1A). The hPD-L1-specific binding was also detected for plain Jurkat E6.1 cells that do not express PD-1 or B7-1, and was blocked by anti-PD-L1 but not anti-PD-1 or anti-B7-1 antibodies (Figure 6.1B). The interaction was strong enough

to be captured in staining of these two cell lines using tetramers made from biotinylated PD-L1/PD-L2 and fluorophore-conjugated SA (Figures 6.2A & B). Tetramer staining of other immune cell lines identified THP-1 cells but not Raji B cells showing the same specific binding to hPD-L1, although they both express B7-1 (Figures 6.2C & D).

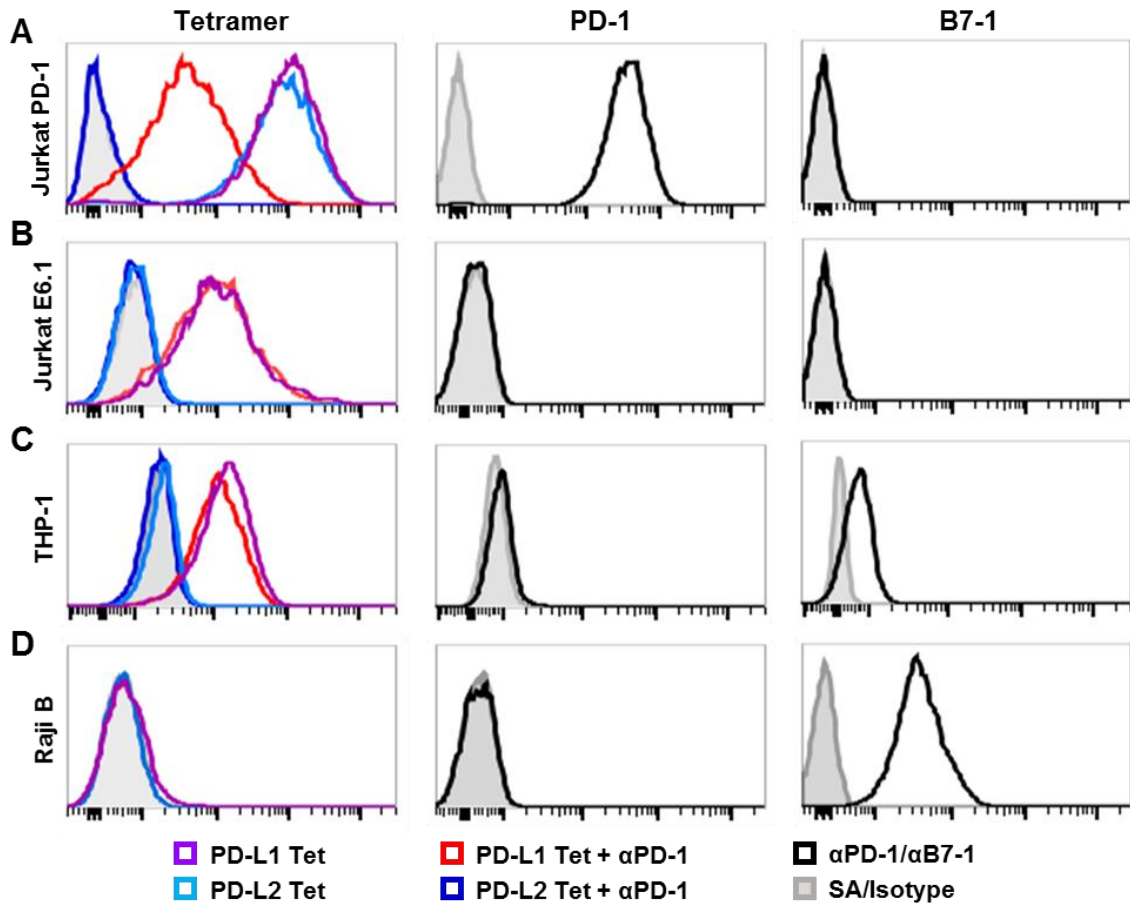


Figure 6.2: hPD-L1 tetramer positively stains Jurkat, THP-1, but not Raji B cells. Staining of Jurkat PD-1 (A), Jurkat E6.1 (B), THP-1 (C), and Raji B (D) cells with hPD-ligand tetramer (left), anti-PD-1 (middle), or anti-B7-1 (right) antibodies.

The positive staining is unlikely resulted from the non-specific phagocytic behavior of the cell lines, because 1) only hPD-L1 tetramer but not hPD-L2 tetramer or SA alone shows positive staining on Jurkat and THP-1 cells, 2) hPD-L1 tetramer positive staining does not rely on the fluorophore conjugated with SA (Figure 6.3), and 3) the fluorescence intensity of hPD-L1 tetramer staining at 4 °C is still significantly higher than the

background defined by SA alone (Figure 6.4). Neither does the positive staining represent non-physiological and non-specific stickiness of cell lines, since staining of whole blood from healthy donor identified the entire population of CD14⁺ monocytes with undetectable PD-1 or B7-1 expression showing specific binding to hPD-L1 tetramer but not hPD-L2 tetramer or SA (Figure 6.5). Again, the hPD-L1 tetramer positive staining on this population was not affected by anti-PD-1 blocking. These data suggest the existence of additional binding partner(s) for hPD-L1 other than PD-1 and B7-1.

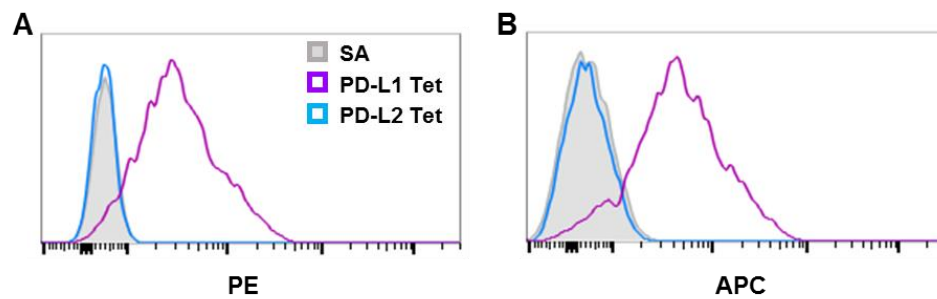


Figure 6.3: hPD-L1 tetramer staining does not depend on fluorophore. Jurkat E6.1 cells were stained with hPD-ligand tetramers conjugated with PE (A) or APC (B).

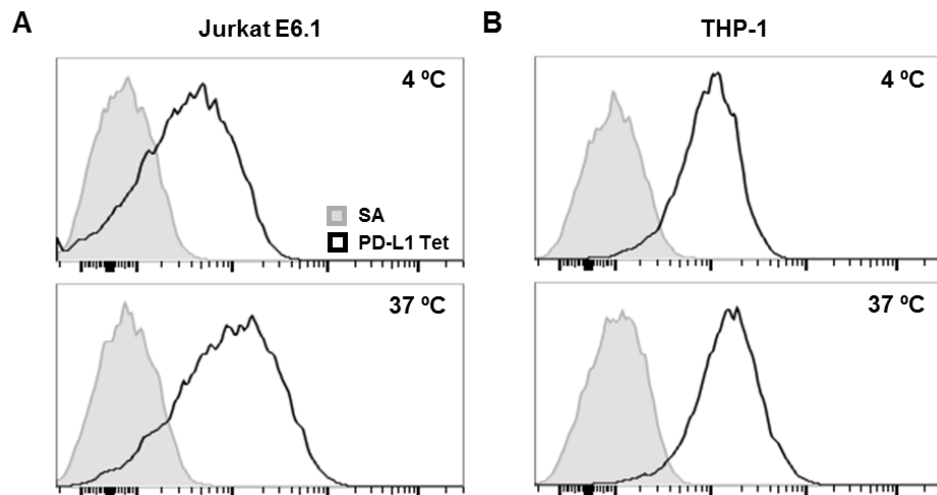


Figure 6.4 The effect of temperature on hPD-L1 tetramer staining. Jurkat E6.1 (A) or THP-1 (B) cells were stained with hPD-L1 tetramers at 4 °C (upper) and 37 °C (lower).

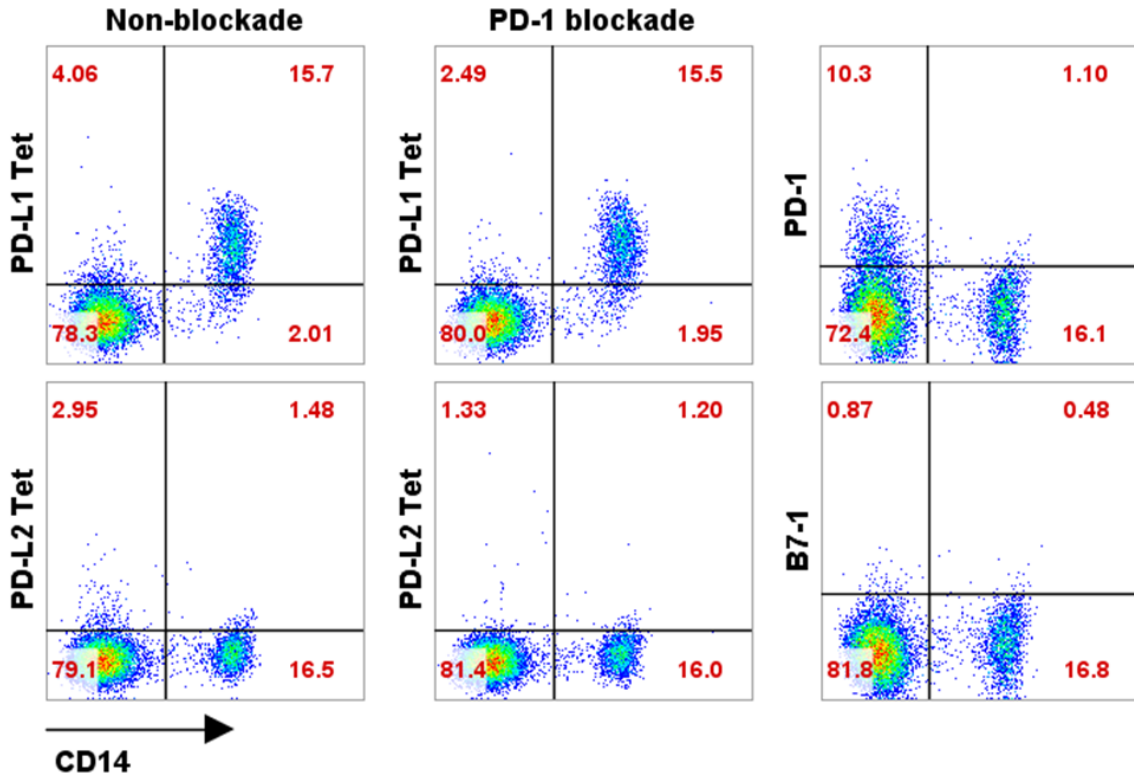


Figure 6.5: hPD-L1 tetramer positively stains CD14⁺ cells in human peripheral blood. cells were gated on lymphocyte population based on FSC vs SSC.

6.2.2 Identification of CD222 as a tentative binding partner for hPD-L1

To identify the tentative molecular interacting with hPD-L1, we conducted direct pulldown from Jurkat membrane lysate with hPD-L1/hPD-L2 coupled SA beads. The 1st elution of beads using low pH buffer released significant amount of protein from hPD-L1 beads but not hPD-L2, as shown by the presence of multiple bands in PD-L1 lane vs their absence in PD-L2 lane (Figure 6.6). Most of these bands are of high molecular weight, with the most intensive one around 270 kD. 2nd elution by boiling beads in laemmli buffer confirms the ligand coupling and also no other proteins escaped from the 1st elution (Figure 6.6). Therefore, the multiple bands in PD-L1 lane for the 1st elution most likely contain the molecule(s) responsible for the hPD-L1 tetramer staining of Jurkat cells.

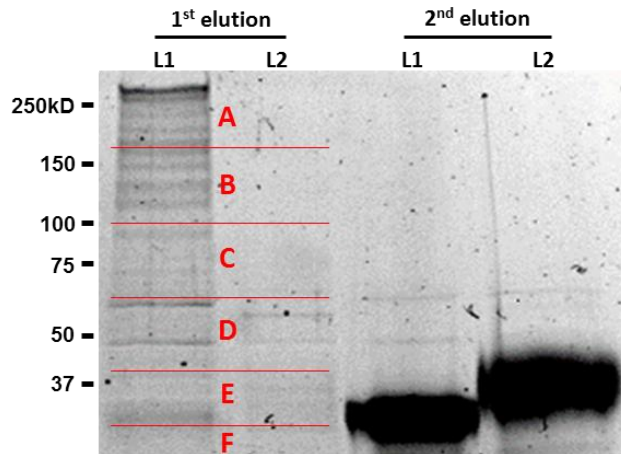


Figure 6.6 Pulldown from Jurkat membrane lysate using hPD-L1/hPD-L2 coupled SA beads. Crude membrane lysate of Jurkat E6.1 cells were clarified and incubated with hPD-L1/hPD-L2 coated SA Dynabeads overnight, followed by 3x washes in lysis buffer, 1st elution with low pH buffer, and 2nd elution with boiling in laemmli buffer. Eluates were analyzed by SDS-PAGE and displayed with Sypro-ruby staining. Gel of the 1st elution was divided into A – F segments as labeled for each lane, followed by trypsin digestion and mass spectrometry analysis.

We then performed in-gel trypsin digestion of the PD-L1 and PD-L2 lanes each in six sections (A-F) and analyzed the enriched peptides using LTQ OrbiTrap tandem mass spectrometer. Searching against non-redundant database identified a series of peptide spectrum matches, with CD222 the most significant one in PD-L1 samples but absent in all PD-L2 samples (Figure 6.7A). The number of PSMs is the highest in section A (MW > 170 kD), and decreases as the molecular weight goes lower, a similar pattern as the distribution of protein bands in the gel (Figures 6.6, 6.7A & B). Mapping the detected peptides in each section to their position on the protein reveals a random pattern across the whole length of the protein (Figure 6.7C), suggesting that the lighter bands represent at least in part, the fragments of CD222.

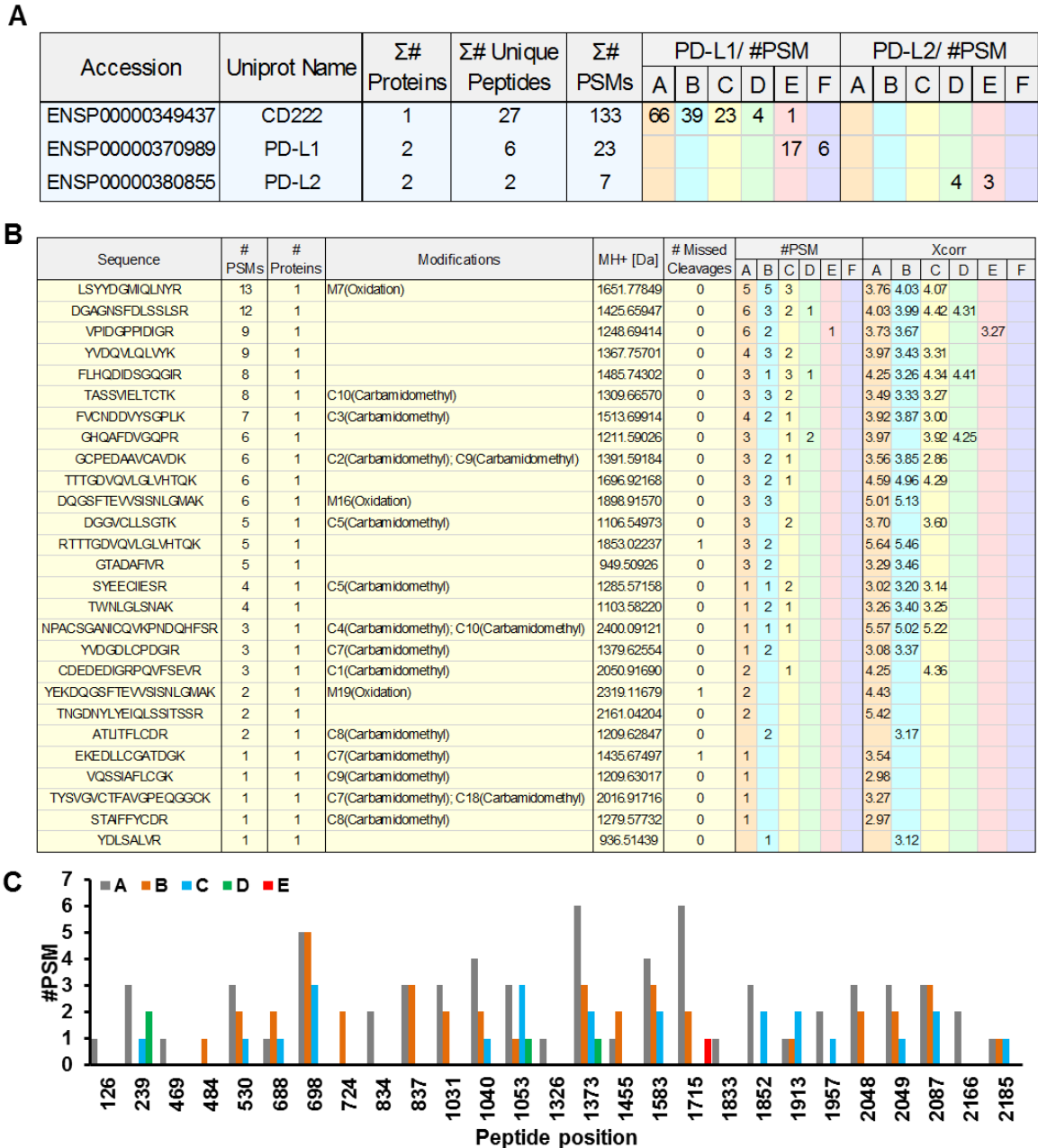


Figure 6.7: Mass spectrometry analysis identified CD222 as a tentative binding partner for hPD-L1. A) Peptide spectrum matches of CD222, PD-L1, and PD-L2 in all samples analyzed. B) Detailed matching parameters for each matched peptide of CD222 in searching against non-redundant database. C) The amino acid position of each matched CD222 peptide.

6.2.3 Validation of hPD-L1–CD222 interaction

We first examined the CD222 surface expression on the hPD-L1 Tet⁺ cell lines/populations using a monoclonal antibody (clone MEM-238). Both Jurkat and THP-1 cells were stained positive for CD222 on their plasma membrane comparing with isotype control (Figures 6.8A & B). CD222 surface staining of whole blood also matches the pattern of hPD-L1 tetramer staining, with a nice correlation in their fluorescence intensities on CD14⁺ population (Figures 6.8C & D). Moreover, hPD-L1 tetramer staining were abolished by blocking with the domain 1 – domain 9 fragment (D1-9, AA43-1365) of recombinant CD222, but not the domain 10 – domain 13 fragment (D10-13, AA1510-2108), suggesting the binding site(s) most likely located within D1-9 (Figure 6.9). The interaction was further confirmed by the hPD-L1 tetramer positive staining on CHO cells expressing hCD222-GFP. Despite the intracellular accumulation of the majority CD222-GFP molecules, surface staining using anti-CD222 or hPD-L1 tetramer strongly correlates with GFP expression (Figure 6.10). These data confirm CD222 as another binding partner for hPD-L1.

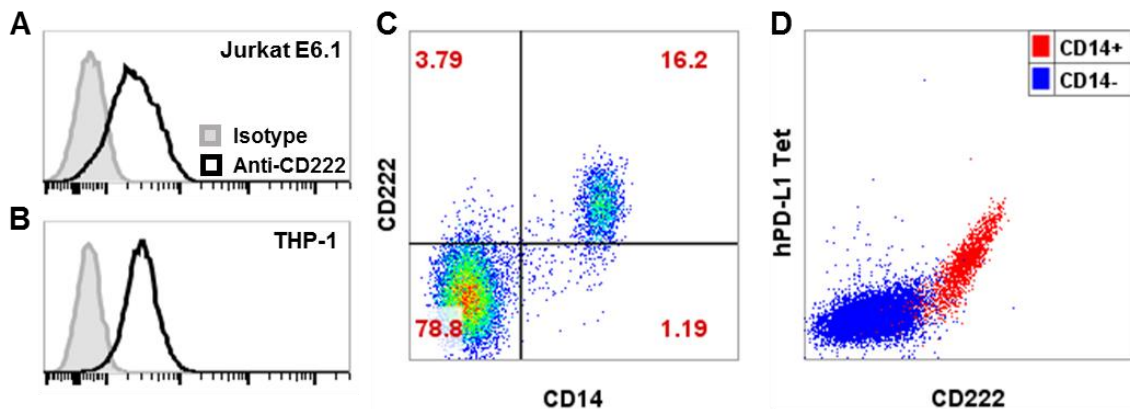


Figure 6.8: CD222 surface expression correlates with hPD-L1 tetramer staining. A) – C) CD222 staining of Jurkat E6.1 (A), THP-1 (B), and human peripheral blood (C) using monoclonal antibody MEM-238. D) MEM-238 staining correlates with hPD-L1 tetramer staining on CD14⁺ cells from (C).

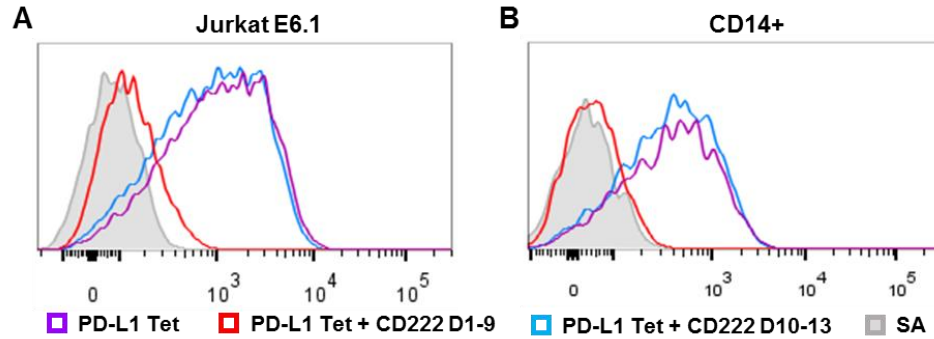


Figure 6.9: hPD-L1 tetramer staining was blocked by recombinant CD222 D1-9. Jurkat E6.1 cells and human peripheral blood were stained with hPD-L1 tetramer without or with the presence of CD222 D1-9, or D10-13.

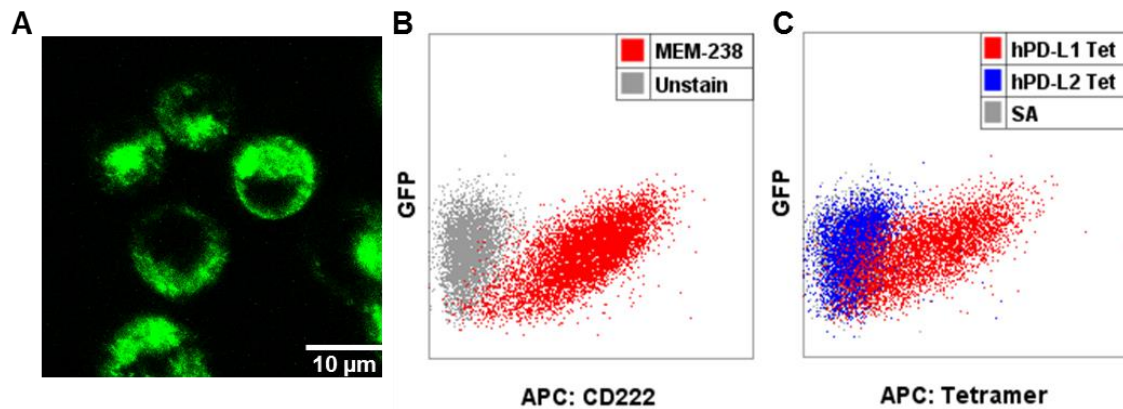


Figure 6.10: hPD-L1 binds to CD222-GFP transfected CHO cells. A) Confocal imaging of CD222-GFP. B) & C) CD222-GFP expression correlates with surface staining using anti-CD222 (MEM-238), or hPD-L1 tetramer.

6.2.4 3D and 2D binding kinetics of hPD-L1–CD222

We then performed SPR analysis to characterize the 3D affinity and kinetics of hPD-L1–CD222 interaction. Figure 6.11A shows corrected sensorgrams of increasing concentrations of CD222 D1-9 injected over hPD-L1 surface. The binding reaches equilibrium within 15 s after injection and the dissociation takes ~ 10 s, indicating very fast on and off rate. Fitting the binding-concentration curve to 1:1 Langmuir binding model yields a K_d value of 1.07 μM (Figure 6.11B). Yet, Scatchard plot suggests multivalent binding with the two slopes translated into apparent K_d values of 1.04 μM and 0.3 μM

(Figure 6.11C). Also, global fitting of the sensorgram curves to heterogeneous ligand model yielded similar K_d values of $1.35 \mu\text{M}$ ($R_{max} = 125.9$) and $0.13 \mu\text{M}$ ($R_{max} = 12.13$), while fitting to 1:1 binding model failed to converge. As both hPD-L1 and CD222 D1-9 are monomers (analyzed by native PAGE, data not shown), the SPR analysis suggests a binding mode involving two sites, with the dominant one with a $K_d = 1.35 \mu\text{M}$, which is 5-fold higher than hPD-L1–PD-1 ($K_d = 7.68 \mu\text{M}$) and 18-fold higher than hPD-L1–B7-1 ($K_d = 25.44 \mu\text{M}$).

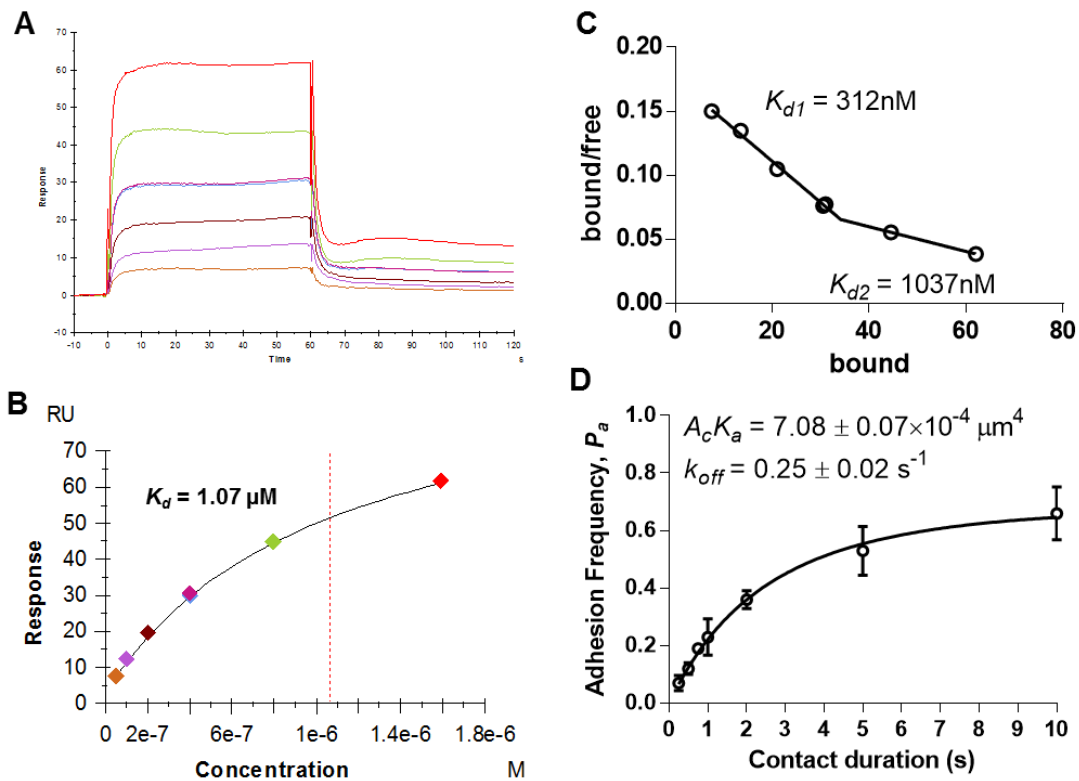


Figure 6.11: 3D and 2D kinetics of hPD-L1–CD222 interaction. **A)** SPR sensorgrams of increasing concentrations (from 50 nM to $1.6 \mu\text{M}$) of CD222 D1-9 injected over hPD-L1 immobilized surface. Responses of reference surface and blank solution were subtracted. **B)** Nonlinear fitting for steady-state affinity analysis. **C)** Scatchard plot show a two-slope pattern. **D)** 2D kinetics analysis of CD222-GFP CHO cell binding to hPD-L1 coated RBCs.

2D kinetic analysis using CD222-GFP CHO cells and hPD-L1 coated RBCs (Figure 6.11D) reveals a 2D affinity/avidity slightly higher than hPD-L1–PD-1 ($7.08 \pm$

$0.07 \times 10^{-4} \mu\text{m}^4$ vs $4.47 \pm 0.30 \times 10^{-4} \mu\text{m}^4$). This is largely attributed to the slower 2D k_{off} (0.26 s^{-1} vs 0.50 s^{-1}), which may partially due to the multivalent binding to the suggested non-covalent dimers of CD222 on the plasma membrane.

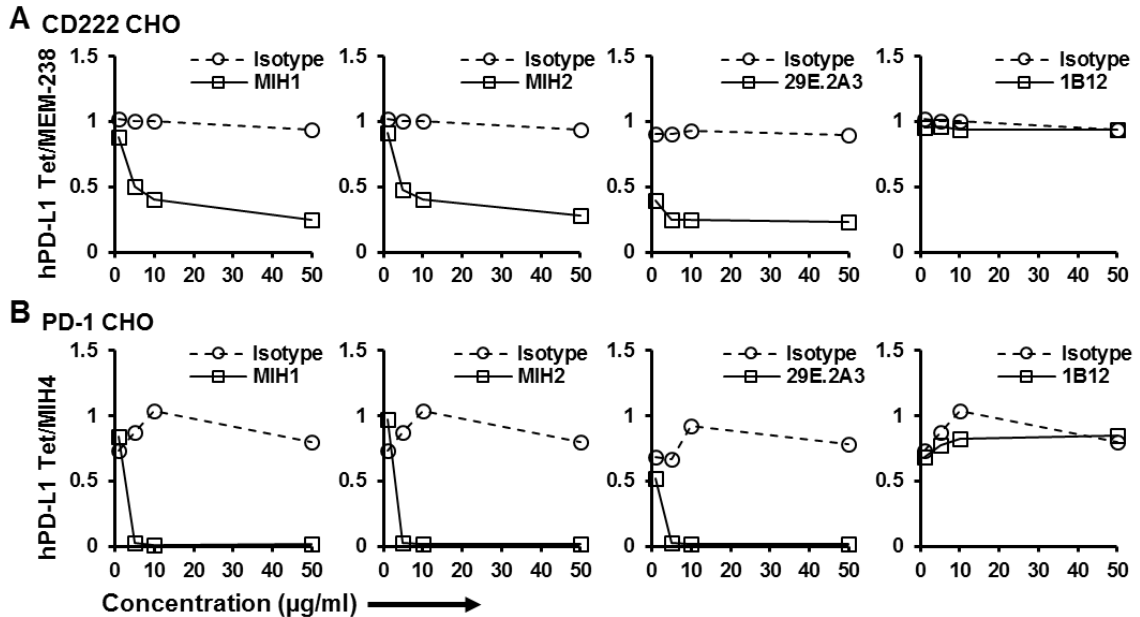


Figure 6.12 Binding site mapping with anti-PD-L1 monoclonal antibodies. CD222-GFP CHO cells (A) or PD-1 CHO cells (B) were stained with hPD-L1 tetramer with the presence of increasing concentration of MIH1 (1st column), MIH2 (2nd column), 29E.2A3 (3rd column), and 1B12 (4th column), as well as their respective isotype Ig. MEM-238 staining of CD222-GFP CHO cells and MIH4 staining of PD-1 CHO cells were included as a control for surface receptor densities.

6.2.5 CD222 competes with PD-1 in PD-L1 binding

To further compare the binding sites of CD222 and PD-1 on PD-L1, we then tested four monoclonal anti-PD-L1 antibodies their ability to block CD222 binding and also PD-1 binding as a reference. CD222-GFP or PD-1 CHO cells were stained with hPD-L1 tetramer in the presence of various concentrations of these anti-PD-L1 antibodies or their corresponding isotype Ig. The MFI of hPD-L1 tetramer was normalized by that of anti-CD222 (clone MEM-238) or anti-PD-1 (clone MIH4) done under the same condition, which serves as a baseline control for the changes in CD222 or PD-1 densities on the

plasma membrane. Clones MIH1, MIH2, and 29E.2A3 reduced hPD-L1 tetramer binding to CD222-GFP CHO by 50% or more at a concentration of 5 $\mu\text{g/ml}$ and achieved the maximum inhibition of $\sim 70\%$ (Figure 6.12A). These clones also completely abolished hPD-L1 tetramer binding to PD-1 CHO at a concentration of 10 $\mu\text{g/ml}$ (Figure 6.12B). The fourth clone, 1B12, did not affect hPD-L1 tetramer binding to either of the CHO cells. The coincidence of blocking effects by the same antibodies implies close or overlapping regions on hPD-L1 are involved in binding to CD222 and PD-1.

To directly test this competitive binding model, we stained CD222-GFP CHO cells with hPD-L1 tetramer in the presence of various concentrations of PD-1-Fc chimeric protein or isotype Ig. As expected, hPD-L1 tetramer binding to CD222 CHO cells was reduced by 40% at a PD-1-Fc concentration as low as 1 $\mu\text{g/ml}$ with the largest reduction of 60% at plateau (Figure 6.13A). In the opposite case, hPD-L1 tetramer staining of PD-1 CHO cells were reduced by 30% with the presence of 20 $\mu\text{g/ml}$ CD222 D1-9 fragment (Figure 6.13B), confirming the competition of PD-1 and CD222 in binding to hPD-L1.

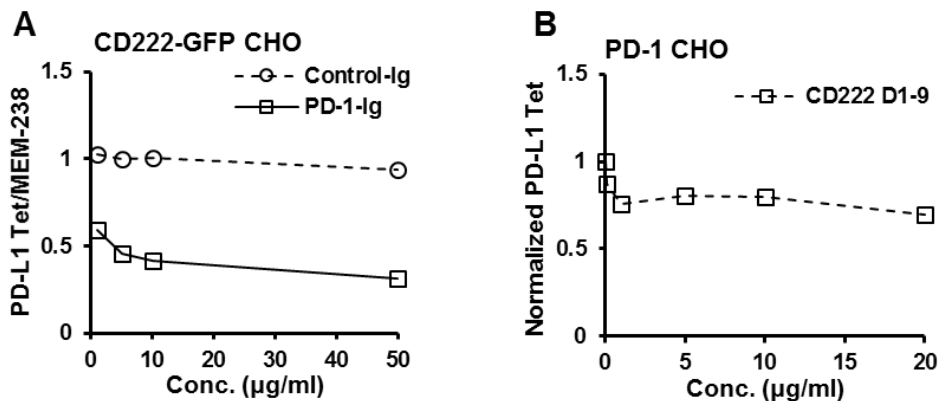


Figure 6.13 Competitive binding of CD222 and PD-1 to hPD-L1. **A)** CD222-GFP CHO cells were stained with hPD-L1 tetramer or MEM-238 in the presence of increasing concentration of PD-1-Fc or control Ig. **B)** PD-1 CHO cells were stained with hPD-L1 tetramer in the presence of CD222 D1-9 fragment.

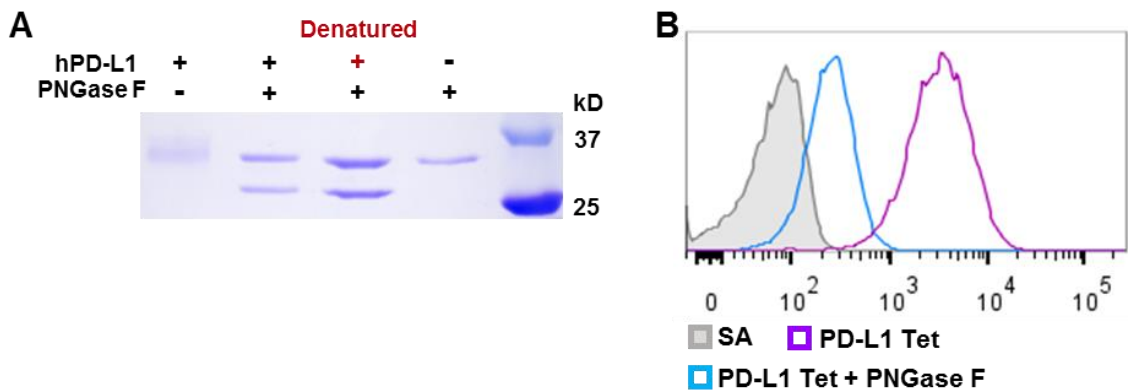


Figure 6.14: hPD-L1 binding to CD222 is largely influenced by its N-glycans. A) Validation of hPD-L1 deglycosylation by PNGase F treatment for 3.5 hr. Samples were analyzed by SDS-PAGE followed by coomassie blue staining. Native hPD-L1 were used except for the denatured sample. B) Tetramer staining of CD222-GFP CHO cells using untreated or PNGase F treated hPD-L1.

6.2.6 hPD-L1 binding to CD222 is largely influenced by its N-glycans

The residual binding between hPD-L1 and CD222 with the presence of anti-PD-L1 antibodies or PD-1-Fc suggests other components contributing significantly to hPD-L1–CD222 interaction. CD222 is known to bind multiple ligands falling into two categories: M6P containing ligand (e.g. TGF- β 1 precursor and granzyme B) and non-M6P containing ligand (e.g. IGF-II and uPAR). The binding of M6P containing ligands is mediated by the two high-affinity binding sites on domain 3 and 9, as well as a low-affinity binding site on domain 5. Non-M6P ligand binding was found on domain 11 and 13 for IGF-II and domain 1 for plasminogen/uPAR [87, 139]. Our results showing hPD-L1 binds to CD222 D1-9 not D10-13 implies potential involvement of the M6P moiety or related glycan structures in this interaction. To examine whether the N-glycans of hPD-L1 would impact its binding to CD222, we treated native hPD-L1 with PNGase F for 6.5 hr at 37 °C, which reduced its molecular weight from ~35 kD to ~27 kD with a sharper band reflecting a more

homogeneous composition (Figure 6.14A). No difference was found in terms of molecular weight or band pattern comparing PNGase F treated native vs denatured hPD-L1, confirming the complete removal of N-glycans from the native protein. Tetramer staining using PNGase F treated hPD-L1 largely reduced the fluorescence intensity but did not completely abolish it (Figure 6.14B), suggesting that N-glycosylation or possibly the M6P moieties of hPD-L1 greatly influences its binding to CD222.

6.2.7 Dual binding site model for hPD-L1–CD222

The fact that either anti-PD-L1 blocking or PNGase F treatment of hPD-L1 reduced but did not abolish binding suggests a binding mode involving these two components. A detailed visualization of PD-L1 structure demonstrates the distant distribution of PD-1 binding site and the N-glycosylation sites: 3 of the 4 N-glycosylation sites on hPD-L1 are located in the IgC domain, while the only one on IgV domain is on the opposite side of the hPD-L1–PD-1 binding site (Figure 6.15A). Such distant distribution presumably excludes possibilities where reduced hPD-L1 binding by one perturbation is a result of allosteric effects on the other binding components, and thereby suggests a cooperation of the two instead. To directly test this hypothesis, we stained CD222-GFP CHO cells with PNGase F treated hPD-L1 with or without additional anti-PD-L1 blocking. Indeed, combining PNGase F treatment with anti-PD-L1 blocking achieved the maximum level of inhibition of hPD-L1 tetramer binding, which was close to the background staining (Figure 6.15B). Together these data indicate a dual binding site model for hPD-L1–CD222 consisting of both protein-protein binding and lectin-carbohydrate binding components.

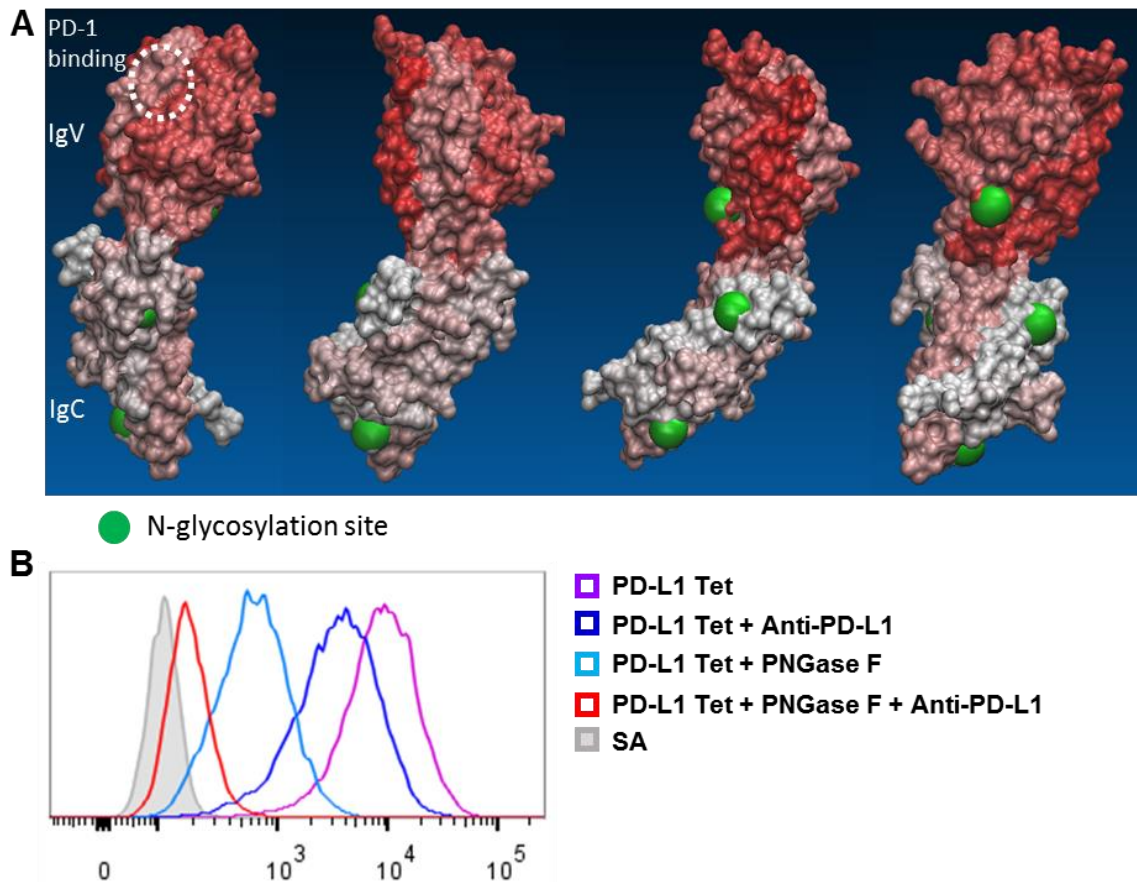


Figure 6.15: Dual binding site model for hPD-L1-CD222 interaction. A) Structure of hPD-L1 showing the PD-1 binding site and N-glycosylation sites (green spheres). B) Tetramer staining of CD222-GFP CHO cells using untreated or PNGase F treated hPD-L1 with or without anti-PD-L1 blocking.

6.2.8 Screening for blocking reagents targeting CD222

We then focused on CD222 side screening for antibodies and chemicals that could block this interaction. Figure 6.16 shows hPD-L1 tetramer staining of CD222-GFP CHO cells with the presence of various concentrations of anti-CD222 monoclonal antibodies (clone MEM-238, NEM-239, NFN-349, and 2G11) and their respective isotype Ig. Mild decreases in hPD-L1 tetramer staining was observed for all four antibodies tested starting from a concentration of 1 $\mu\text{g/ml}$ and reached plateaus of 20% - 40% inhibition at a concentration of 50 $\mu\text{g/ml}$. Although the binding sites of these antibodies are not fully

mapped, the synchronized mild inhibition of hPD-L1 tetramer staining is less likely due to direct inhibition, but instead non-specific effects such as steric hindrance, allosteric changes, or internalization of CD222 triggered by antibody crosslinking.

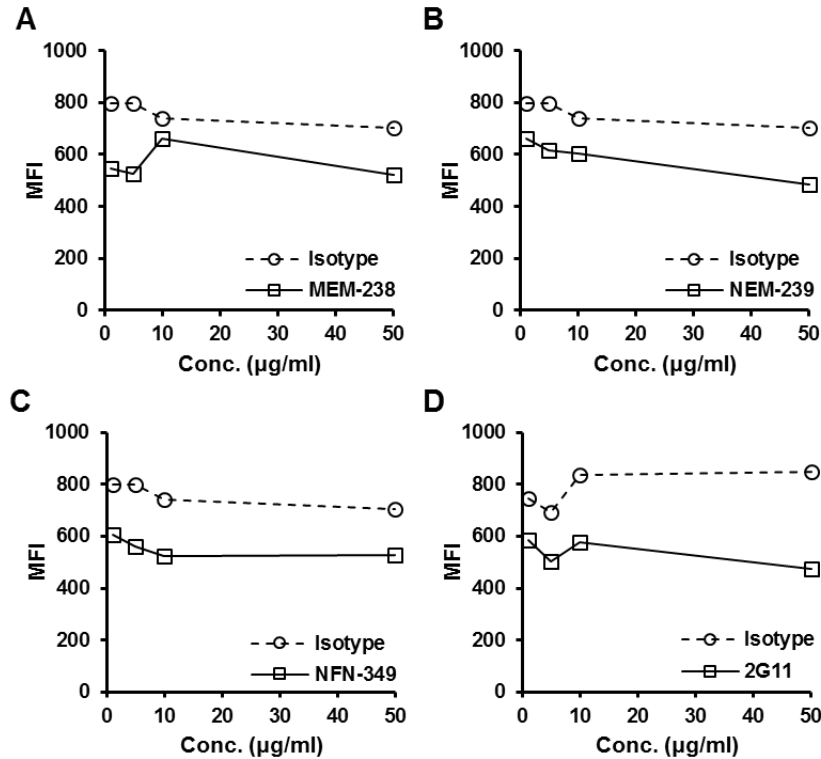


Figure 6.16: Screening of anti-CD222 monoclonal antibodies. CD222-GFP CHO cell were stained with hPD-L1 tetramer with the presence of increasing concentration of MEM-238 (A), NEM-239 (B), NFN-349 (C), and 2G11 (D), as well as their respective isotype Ig.

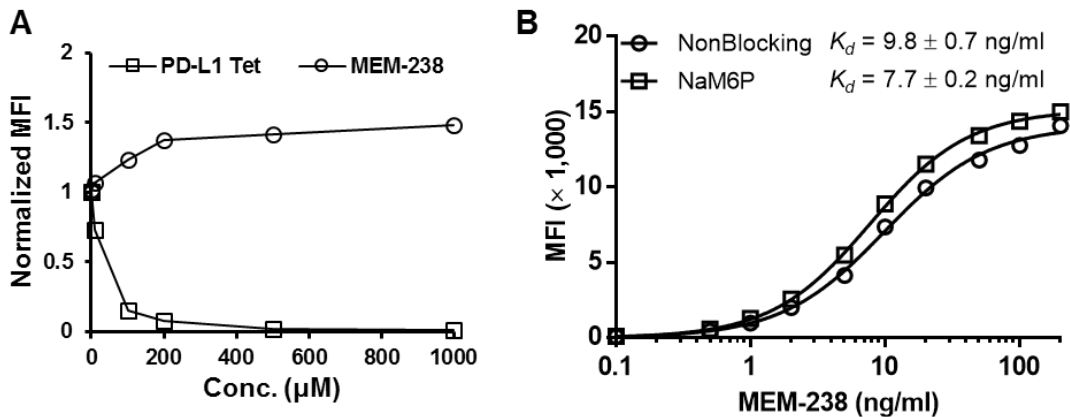


Figure 6.17: Effect of NaM6P on hPD-L1 and MEM-138 binding to CD222. A) CD22-GFP CHO cells were stained with hPD-L1 tetramer or MEM-238 in the presence of

increasing concentration of NaM6P. **B)** CD222-GFP CHO cells were stained with increasing concentrations of MEM-238 antibody with or without 500 μ M NaM6P.

In contrast, hPD-L1 tetramer staining of CD222-GFP CHO cells was completely abolished by NaM6P blocking with an IC₅₀ value of 50 μ M at PD-L1 concentration of 50 nM (Figure 6.17A). The inhibition was not due to internalization triggered by NaM6P, since MEM-238 antibody staining of CD222 did not decrease and was even enhanced by 50% (Figure 6.17A). One possibility for the increased MEM-238 staining is that M6P binding to CD222 increases its surface display while directly inhibits hPD-L1 binding. Yet, this could be ruled out by the fact that the enhancement of MEM-238 staining with increasing NaM6P concentration mirrors perfectly the decrease of hPD-L1 tetramer intensity, which is unlikely attributed to processes with different kinetics - receptor trafficking vs receptor-ligand binding. Moreover, titration of MEM-238 staining with the presence of 500 μ M NaM6P shows enhanced binding affinity (Figure 6.17B), suggesting the better recognition of CD222 by MEM-238 as due to other factors such as NaM6P-induced allosteric changes of CD222 or pH changes of the buffer. Therefore, the complete inhibition of hPD-L1–CD222 interaction with high concentration of NaM6P suggests a disruption of interactions at both binding sites.

6.2.9 Characterization of CD222 expression on T cells

Despite the absence of CD222 on majority of cell populations but CD14⁺ monocytes in the whole blood staining, expression of CD222 on T cell plasma membrane was detected upon activation [107, 140]. Given the critical role of PD-1–PD-L1 interaction in suppressing T cell responses and the competitive binding of PD-1 and CD222, it is important as how this newly identified interaction would add to the current understanding of PD-1–PD-L1 in regulating T cell function.

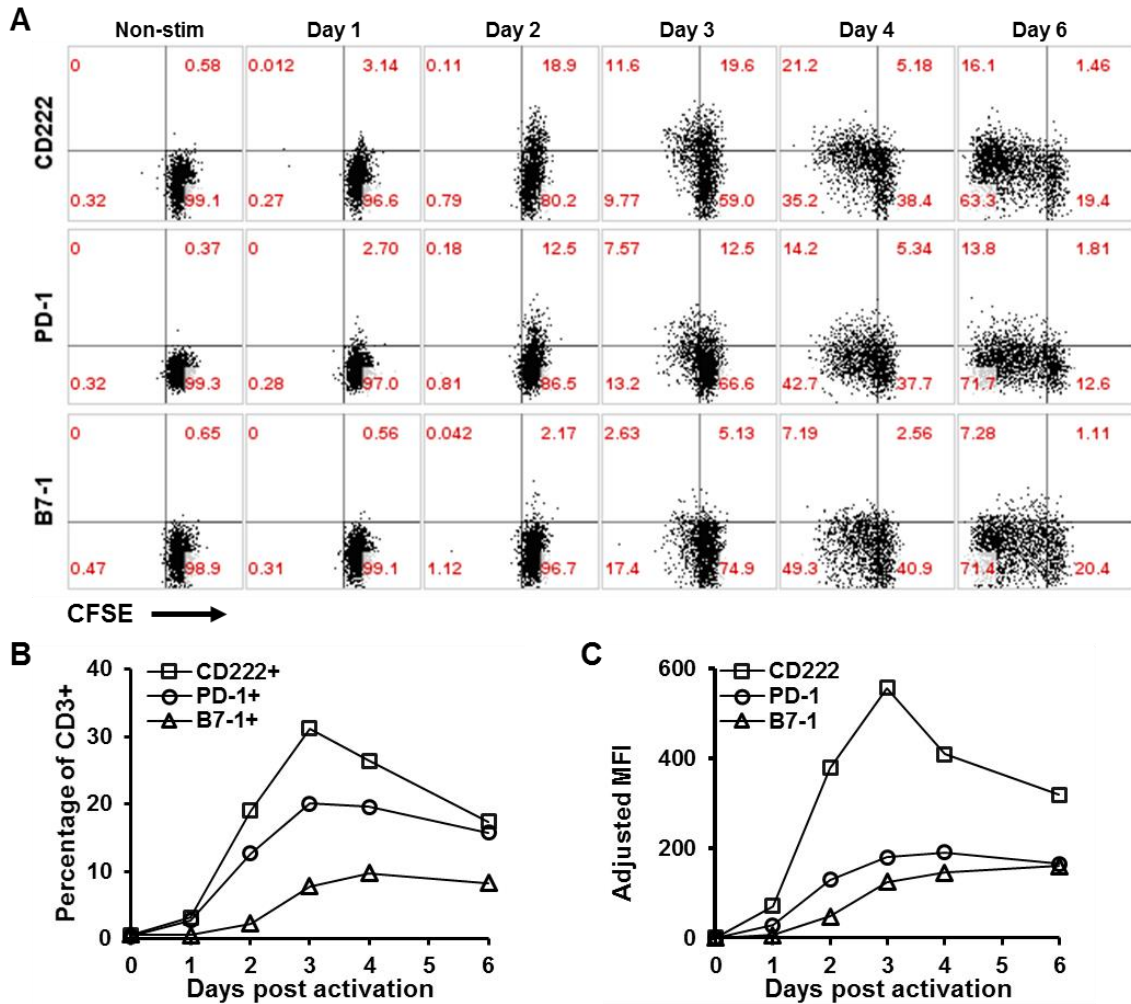


Figure 6.18: Expression of CD222 on activated T cell surface. **A)** CFSE loaded human PBMC were activated by plate-bound anti-CD3 (clone OKT3) and stained for CD222, PD-1, and B7-1 expression. **B)** Frequencies of CD222+, PD-1+, or B7-1+ cells over CD3+ upon anti-CD3 stimulation shown in (A). **C)** CD222, PD-1, or B7-1 MFI of CD3+ population upon anti-CD3 stimulation shown in (A).

We then set to first characterize the expression kinetics of CD222, PD-1, and B7-1 on T cell surface upon activation by plate-bound anti-CD3 (Figure 6.18). Both CD222 and PD-1 expression was upregulated at as early as 1 day following activation, whereas B7-1 expression was slightly delayed. CD222 upregulation was associated with cell proliferation and reached a maximum of 31% positive rate at day 3, higher than that of PD-1 (20% at day 3) and B7-1 (10% at day 4). The MFI was also higher than that of PD-1 and B7-1 over the 6 days with a 3-4-fold difference at day 3 (Figure 6.18C). The advantages of CD222 in

expression and binding avidity predict significant level of hPD-L1–CD222 interaction could exist at the surface of activated T cells, and may perturb the PD-1–PD-L1 functions at least in part by competing for hPD-L1 binding.

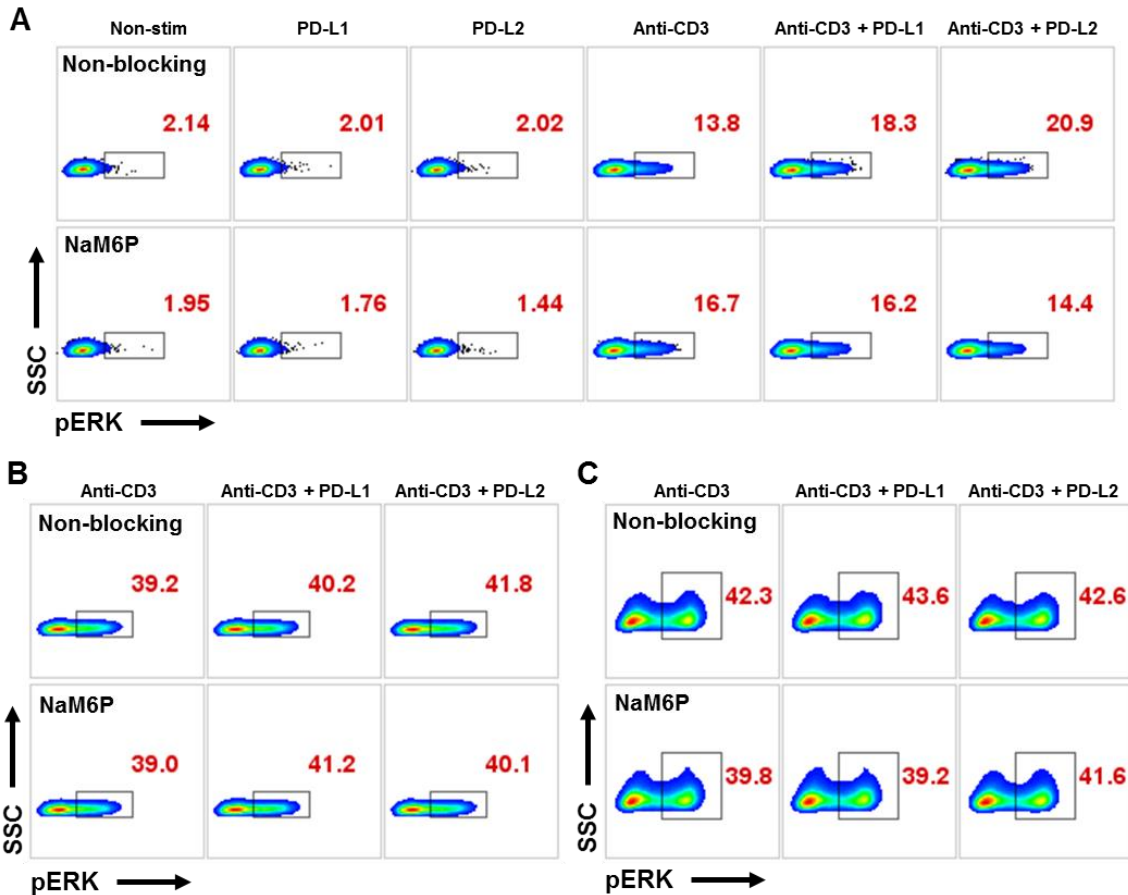


Figure 6.19: hPD-L1-CD222 failed to modulate ERK phosphorylation in Jurkat E6.1 cells. **A) & B)** Jurkat E6.1 cells were stimulated with soluble hPD-L1/hPD-L2 tetramer (2.5 $\mu\text{g/ml}$), OKT3 0.1 $\mu\text{g/ml}$), or a mixture of OKT3 with hPD-L1/hPD-L2 tetramer for 4 min (A) or 6 min (B) in the absence or presence of 1 mM NaM6P, followed by fixation and intracellular staining of pERK. **C)** Jurkat E6.1 cells were stimulated with OKT3, or a mixture of OKT3 with hPD-L1/hPD-L2 coated beads for 4 min in the absence or presence of 1 mM NaM6P, followed by fixation and intracellular staining of pERK.

Due to the complexity of hPD-L1 interactions on activated T cell membrane and a lack of specific and non-toxic blocking reagent for hPD-L1–CD222, studying the long term function of hPD-L1–CD222 on activated T cells is limited. As an alternative, we tend to focus on the short-timescale effects where PD-1 and B7-1 are absent from the plasma

membrane, such as ERK phosphorylation of Jurkat cells. Unlike anti-CD3, stimulation of Jurkat cells with soluble hPD-L1 or hPD-L2 tetramer alone did not affect ERK phosphorylation at 4 min as shown by the intracellular staining of pERK (Figure 6.19A). Also comparing with anti-CD3 stimulation alone, the percentage of pERK⁺ cells was increased by 5-7% when using anti-CD3 mixed with either hPD-L1 or hPD-L2 at 4 min. The enhancement diminished at 6 min and also could be abolished by NaM6P blocking (Figures 6.19A & B). The fact that both hPD-L1 and hPD-L2 triggered such an enhancement of early phosphorylation of ERK differs from the specific binding of hPD-L1 but not hPD-L2 to Jurkat cells, and thus unlikely to be a consequence of hPD-L1–CD222 interaction. We then further examined ERK phosphorylation under the stimulation of immobilized anti-CD3 with or without hPD-1 ligands. However, no significant differences were found in anti-CD3 stimulation alone vs co-stimulation with hPD-L1 or hPD-L2 (Figure 6.19C). Together these data demonstrated that hPD-L1 binding to CD222 on Jurkat cells is unable to induce ERK phosphorylation or alter that triggered by anti-CD3.

6.3 Discussion

The large difference (~60%) in amino acid sequence between PD-L1 and PD-L2, as well as their distinct expression patterns, make it not surprising that overlapping but also distinguished functions may be originated from interactions with the shared (PD-1) or different molecules in various contexts. Indeed, B7-1 was identified to interact with PD-L1, limiting T cell function through bidirectional inhibitory signals [82]. PD-L2 also interacts with RGMb and plays an important role in respiratory tolerance [86]. Here we observed the specific binding of PD-L1 but not PD-L2 to Jurkat, THP-1, and resting human

CD14⁺ monocytes from periphery blood that do not express PD-1. B7-1 expression is undetectable on Jurkat cells, and is also too low on THP-1 or CD14⁺ monocytes to generate the strong binding we observed, according to the weak affinity of PD-L1–B7-1 interaction. Neither was the binding affected by anti-PD-1 or anti-B7-1 blocking, suggesting the existence of additional binding partner(s) specific for hPD-L1. Using Jurkat membrane lysate we have successfully pulled down the target molecule with PD-L1 coated beads and identified it to be CD222 by mass spectrometry. The interaction was further validated by the specific binding of hPD-L1 to CD222-GFP expressing CHO cells and also to a recombinant protein fragment (D1-9) of CD222.

The following question as how hPD-L1 and CD222 interact is critical in several ways. First, affinity and kinetic analysis would allow the comparison with known interactions between these molecules with other counter parts. Second, CD222 is a multifunctional molecule binding to various ligands via either M6P or non-M6P interactions. Determining the mode of hPD-L1–CD222 binding (sugar-lectin vs protein-protein) would set a basis for its relevance and possible regulatory mechanisms in physiological and pathological contexts. Finally, screening for effective blocking reagents would enable perturbations for studies of both interaction and function. All these aspects were covered by this study and related to hPD-L1–PD-1, which has known important functions and clinical applications.

SPR measurement indicates that the monomeric binding of hPD-L1–CD222 is stronger than hPD-L1–PD-1 (3D $K_d = 1.07 \mu\text{M}$ vs $7.68 \mu\text{M}$) [18]. When expressed on CHO cells, CD222 also shows a higher 2D avidity than PD-1 ($7.08 \times 10^{-4} \mu\text{m}^4$ vs $4.47 \times 10^{-4} \mu\text{m}^4$). This is distinct from the much lower 3D and 2D affinities of PD-L1–B7-1 interaction,

and could argue a potentially significant interaction *in vivo*. Most importantly, we found a direct competition between PD-1 and CD222 in binding to hPD-L1, further strengthening the significance of hPD-L1–CD222 interaction. Moreover, CD222 is detected on the surface of a higher percentage of activated T cells and also with a higher level of expression. These results suggest that CD222 could potentially regulate T cell function at least in part through interference with the hPD-L1–PD-1 coinhibitory signals at the level of competing for hPD-L1 binding.

Our data also suggest that hPD-L1–CD222 interaction involves both sugar-lectin and protein-protein binding modes. SPR analysis with immobilized hPD-L1 and soluble CD222 D1-9 displays biphasic kinetics that failed to fit to the 1:1 Langmuir binding model. The better fitting to the heterogeneous ligand model along with the two-slope pattern of the Scatchard plot suggest two binding sites on hPD-L1 for CD222. Indeed, hPD-L1 tetramer binding to CD222-GFP CHO cells was largely reduced but not abolished by either removing its N-glycans with PNGase F, or blocking with PD-1-Fc or monoclonal antibodies that recognize the PD-L1–PD-1 binding interface. In consistency, the PD-1 binding site on hPD-L1 and its N-glycosylation sites are distantly separated. Moreover, PD-L1 tetramer staining of PD-1 CHO cells were not affected by PNGase F treatment. Finally, we observed a further significant reduction in PNGase F-treated hPD-L1 tetramer staining with anti-PD-L1 blocking. Therefore, hPD-L1–CD222 binding is more likely a cooperative interaction of at least two binding interfaces: one is close or partially overlaps with the hPD-L1–PD-1 binding site representing protein-protein binding; the other is mediated by its N-glycan(s) and can work as a regulatory component for adjusting the magnitude of hPD-L1–CD222 interaction in various cell types and contexts.

hPD-L1 binding to CD222 is also subjected to the competition of other CD222 ligands, according to the way how the corresponding two binding interfaces are perturbed. Of interest, hPD-L1 binding to recombinant CD222 is limited to domain 1-9, which contains two M6P binding sites (domain 3 and 9) and one M6PGlcNAc site (domain 5) responsible for binding of other M6P-containing ligands. One possible binding mode consists of the docking a particular N-glycan of hPD-L1 to one of these carbohydrate binding sites (possibly domain 3 or 5 considering the limit set by the dimension of hPD-L1) and the IgV A'GFCC' β -sheet to the adjacent domain. Cooperative docking of these two sites across different domains could render the hPD-L1-CD222 interaction very sensitive to CD222 allosteric changes, which, we believe, is reflected by the elimination of hPD-L1 tetramer staining by NaM6P alone. Large scale conformation changes upon M6P binding has been reported for Cation-dependent mannose-6-phosphate receptor, where loop D switch from "closed" to "open" state [92]. Structure-based sequence alignment suggests the same recognition mechanism although the loop D for CD222 domain 3 is shorter [92]. Therefore, allosteric changes may account for the enhanced recognition of CD222 by monoclonal antibody MEM-238 and also the elimination of hPD-L1 binding with NaM6P blocking.

The signaling capacity of CD222 remains unclear despite its multifaceted ligand binding and functions. While the phosphorylation and palmitoylation of the cytoplasmic tail are mainly responsible for the routing and trafficking purposes [141, 142], the ability in recruiting and activating G_i and triggering downstream signaling also remains elusive [98-100]. Focusing on T cell costimulation/coinhibition, we first attempted to investigate the potential signaling consequences in short time scale using Jurkat cells with undetectable

PD-1 and B7-1. However, we failed to observed any changes in ERK phosphorylation induced by hPD-L1–CD222 alone or co-stimulation with anti-CD3. Future efforts need to be made with efficient and specific blocking strategies to dissect the specific function of this interaction alone from the binding to the other two receptors (PD-1 and B7-1) on T cell surface. Moreover, careful attention need to be paid in choosing anti-PD-1 vs anti-PD-L1 immunotherapies, as anti-PD-L1 blocking antibodies would presumably block both hPD-L1–PD-1 and hPD-L1–CD222 interactions [58].

CHAPTER 7

CONCLUSION AND FUTURE DIRECTIONS

7.1 Conclusion

We presented in this thesis the study of *in situ* PD-1 interaction and its inhibition of the antigen recognition by TCR-CD8 in a kinetic perspective. The identification of the novel interaction between hPD-L1 and CD222 also opens new venues for investigating their functions *in vivo*. With detailed conclusions discussed in each chapter, here we summarize the highlights as below.

- The first systemic 2D kinetic characterization of the human and murine PD-1 systems, the B7-1–PD-L1, B7-1–CD28, and B7-1–CTLA-4 interactions.
 - 2D affinities align in the same trend with 3D affinities.
 - The PD-1 systems display enhanced 2D affinities than 3D ones spanning from middle to strong.
 - Similar as measured in 3D, 2D B7-1–PD-L1 interactions are much weaker than PD-1–PD-L1.
- The first 2D kinetic analysis of crosstalk between activating receptors (TCR and CD8) and inhibitory receptors on activated T cell surface.
 - CD8 contributes to TCR–pMHC interaction by increasing both bond number and bond lifetime – a process that depends on Lck.
 - PD-1–PD-L1 and P14 TCR–H2-D^b:gp33 display distinct force-lifetime spectrum.
 - PD-1 suppresses the CD8 enhancement via SHP-2 signaling, suggesting a “binding-signaling-binding” model to fine-tune antigen recognition.

- Identification and characterization of a novel interaction between hPD-L1 and CD222.
 - hPD-L1, not hPD-L2, binds to CD222.
 - hPD-L1–CD222 interaction consists of both lectin-carbohydrate and protein-protein binding components.
 - CD222 competes with PD-1 in binding to hPD-L1 with higher 3D and 2D affinity/avidity.

7.2 In the near future

The findings in this study raise more questions than they answer. We point out some of the important ones to be potentially continued from this point.

What are the mechanisms underlying the differential regulation of 2D binding kinetics by the cellular environment for different molecules? How are these mechanisms exploited *in vivo* to modulate their interactions and functions under various physiological and pathological contexts? Dissecting these mechanisms will advance our understanding of such cellular-based interactions and their functional consequences. Published and ongoing studies of TCR 2D interactions suggest critical roles of post translational modification (PTM) and its organization on the cell membrane [10, 118]. We also have preliminary data showing that 2D binding of PD-1 can be largely affected by mutations outside of the initial ligand binding interface. These observations further highlight the complexity and significance of cellular regulations of membrane receptor interactions.

How do the kinetic and mechanical properties contribute to PD-1 triggering? In the case of TCR triggering, binding kinetics is a critical component in all the models proposed [143]. The importance of its response under force is also becoming more appreciated [115,

119, 144-147]. Despite the significance of PD-1, the mechanism of its triggering has not been explored. Different from the triggering of TCR, which is an activating receptor, initiation of PD-1 signaling requires input from both ligand binding and TCR signaling. Addressing how the kinetic and mechanical properties of these two receptors are coupled to their conformational and/or spatial regulations is key to understand the mechanism of PD-1 signaling. In particular, imaging PD-1 triggered SHP-2 activities with controlled surface presentation of PD-L1 and pMHC will be informative for the spatiotemporal dynamics and regulation of such triggering events.

What is the detailed molecular mechanism of TCR–CD8 cooperative binding? This study suggests that the TCR–CD8 cooperative binding can serve as a tunable component to adjust the strength of antigen stimulation. However, the molecular mechanism of this process itself is not well understood. Considering the elimination of this process by inhibiting Lck activities or its association with CD8 [12, 14], the recruitment of CD8 to TCR-CD3 [14, 15, 148, 149], the kinase-independent role of ZAP-70 [150], as well as the non-redundant roles of highly complex ITAM architecture of CD3, a bold hypothesis is that binding of Lck SH2 domain to pITAM would serve as an adaptor to recruit CD8 to the proximity. An alternative model involves the binding of ZAP-70 to pITAM, which then recruits CD8 via Lck. Mutations abolishing such adaptor properties would possibly delineate the contribution of the enzymatic activities and adaptor functions for TCR–CD8 cooperative binding.

Finally, what is the function of hPD-L1–CD222 interaction? One important question to be answered first is that whether this interaction is significant for hPD-L1 expressed *in vivo*? We have shown that the hPD-L1–CD222 interaction consists of both

protein-protein and lectin-carbohydrate binding components. The former one is considered specific, whereas the latter one is less specific, especially given that the hPD-L1 protein were made in CHO cells where the glycan structures are different from human cells. Therefore, examination of hPD-L1–CD222 interaction with native hPD-L1 would allow for a more in-depth understanding of the regulation of binding by glycosylation *in vivo*. This would also set a basis for probing the functions of this interaction in various contexts. Other than the regulation of expression and glycosylation of hPD-L1, the membrane display of CD222 also varies by cell types or even the same cell types at distinct differentiation stages. For example, CD222 is detectable on resting monocytes and granulocytes but not on T cells until activation. It is also upregulated on multiple types of malignant cells. Therefore, although this study focused mainly on T cells, the possible functions of hPD-L1–CD222 are more likely cell type-dependent.

7.3 In the far future

亢龙有悔，盈不可久也。(The dragon exceeds the proper limits; there will be occasion for repentance.' – a state of fulness, that is, should not be indulged in long [151].)

—— *I Ching*

PD-1 emerges, thrives and will do, but will not escape the fate of waning to the close. So will go the next PD-1. We try to understand how these molecules work. We then harness them to treat diseases and improve our lives. We then create new molecules, cells or lifeforms. The gifts endowed to us in that ancient “accident” have never been shown so magnificent, making the question “where these researches would ultimately lead us to” far beyond our imagination.

It's perhaps all about time and evolution. But have we evolved to equip with enough "regulatory mechanisms" for a "human response" at the proper time and location, with the optimal "magnitude" and "duration"? In the book "*The impact of science on society*" by Bertrand Russel in 1952, he foresaw the major challenge to a stable scientific society to be the "population problem", which (coincidentally?) converges to the main theme of evolution. Alexander Fleming, who discovered penicillin, predicted the post-antibiotic era in 1945 saying "the thoughtless person playing with penicillin treatment is morally responsible for the death of a man who succumbs to infection with a penicillin-resistant organism. I hope this evil can be averted."

But can we avert it? As we are enjoying the benefits of harnessing the nature to advance every bit of what we call our civilization, the evils are inevitably accelerating their paces. That is co-evolution.

And centrality is the key.

REFERENCES

1. Tu, W., *Centrality and commonality : an essay on Confucian religiousness*. A rev. and enl. ed. SUNY series in Chinese philosophy and culture. 1989, Albany, N.Y.: State University of New York Press. x, 165 p.
2. Darwin, C., *On the origin of species by means of natural selection*. 1859, London,: J. Murray. ix, 1 , 502 p.
3. Rudolph, M.G., R.L. Stanfield, and I.A. Wilson, *How TCRs bind MHCs, peptides, and coreceptors*. *Annu Rev Immunol*, 2006. **24**: p. 419-66.
4. Cole, D.K., et al., *The molecular determinants of CD8 co-receptor function*. *Immunology*, 2012. **137**(2): p. 139-48.
5. Leishman, A.J., et al., *T cell responses modulated through interaction between CD8alphaalpha and the nonclassical MHC class I molecule, TL*. *Science*, 2001. **294**(5548): p. 1936-9.
6. Alam, S.M., et al., *Qualitative and quantitative differences in T cell receptor binding of agonist and antagonist ligands*. *Immunity*, 1999. **10**(2): p. 227-37.
7. Boulter, J.M., et al., *Potent T cell agonism mediated by a very rapid TCR/pMHC interaction*. *European Journal of Immunology*, 2007. **37**(3): p. 798-806.
8. Moody, A.M., et al., *The CD8alphabeta co-receptor on double-positive thymocytes binds with differing affinities to the products of distinct class I MHC loci*. *Eur J Immunol*, 2001. **31**(9): p. 2791-9.
9. Huang, J., et al., *Kinetics of MHC-CD8 Interaction at the T Cell Membrane*. *The Journal of Immunology*, 2007. **179**(11): p. 7653-7662.
10. Huang, J., et al., *The kinetics of two-dimensional TCR and pMHC interactions determine T-cell responsiveness*. *Nature*, 2010. **464**(7290): p. 932-6.
11. O'Rourke, A.M., J. Rogers, and M.F. Mescher, *Activated CD8 binding to class I protein mediated by the T-cell receptor results in signalling*. *Nature*, 1990. **346**(6280): p. 187-9.
12. Jiang, N., et al., *Two-stage cooperative T cell receptor-peptide major histocompatibility complex-CD8 trimolecular interactions amplify antigen discrimination*. *Immunity*, 2011. **34**(1): p. 13-23.
13. Liu, B., et al., *2D TCR-pMHC-CD8 kinetics determines T-cell responses in a self-antigen-specific TCR system*. *Eur J Immunol*, 2014. **44**(1): p. 239-50.

14. Casas, J., et al., *Ligand-engaged TCR is triggered by Lck not associated with CD8 coreceptor*. Nat Commun, 2014. **5**: p. 5624.
15. Yachi, P.P., et al., *Altered peptide ligands induce delayed CD8-T cell receptor interaction--a role for CD8 in distinguishing antigen quality*. Immunity, 2006. **25**(2): p. 203-11.
16. Ishida, Y., et al., *Induced expression of PD-1, a novel member of the immunoglobulin gene superfamily, upon programmed cell death*. EMBO J, 1992. **11**(11): p. 3887-95.
17. Shinohara, T., et al., *Structure and chromosomal localization of the human PD-1 gene (PDCD1)*. Genomics, 1994. **23**(3): p. 704-6.
18. Cheng, X., et al., *Structure and interactions of the human programmed cell death 1 receptor*. J Biol Chem, 2013. **288**(17): p. 11771-85.
19. Lazar-Molnar, E., et al., *Crystal structure of the complex between programmed death-1 (PD-1) and its ligand PD-L2*. Proc Natl Acad Sci U S A, 2008. **105**(30): p. 10483-8.
20. Lin, D.Y., et al., *The PD-1/PD-L1 complex resembles the antigen-binding Fv domains of antibodies and T cell receptors*. Proc Natl Acad Sci U S A, 2008. **105**(8): p. 3011-6.
21. Greenwald, R.J., G.J. Freeman, and A.H. Sharpe, *The B7 family revisited*. Annu Rev Immunol, 2005. **23**: p. 515-48.
22. Agata, Y., et al., *Expression of the PD-1 antigen on the surface of stimulated mouse T and B lymphocytes*. Int Immunol, 1996. **8**(5): p. 765-72.
23. Nishimura, H., et al., *Developmentally regulated expression of the PD-1 protein on the surface of double-negative (CD4-CD8-) thymocytes*. Int Immunol, 1996. **8**(5): p. 773-80.
24. Keir, M.E., et al., *PD-1 and Its Ligands in Tolerance and Immunity*. Annual Review of Immunology, 2008. **26**(1): p. 677-704.
25. Schildberg, F.A., et al., *Coinhibitory Pathways in the B7-CD28 Ligand-Receptor Family*. Immunity, 2016. **44**(5): p. 955-72.
26. Chang, W.-S., et al., *Cutting Edge: Programmed Death-1/Programmed Death Ligand 1 Interaction Regulates the Induction and Maintenance of Invariant NKT Cell Anergy*. The Journal of Immunology, 2008. **181**(10): p. 6707-6710.
27. Said, E.A., et al., *Programmed death-1-induced interleukin-10 production by monocytes impairs CD4+ T cell activation during HIV infection*. Nat Med, 2010. **16**(4): p. 452-9.

28. Kleffel, S., et al., *Melanoma Cell-Intrinsic PD-1 Receptor Functions Promote Tumor Growth*. Cell, 2015. **162**(6): p. 1242-56.
29. Bally, A.P., J.W. Austin, and J.M. Boss, *Genetic and Epigenetic Regulation of PD-1 Expression*. J Immunol, 2016. **196**(6): p. 2431-7.
30. Barber, D.L., et al., *Restoring function in exhausted CD8 T cells during chronic viral infection*. Nature, 2006. **439**(7077): p. 682-7.
31. Youngblood, B., et al., *Chronic virus infection enforces demethylation of the locus that encodes PD-1 in antigen-specific CD8(+) T cells*. Immunity, 2011. **35**(3): p. 400-12.
32. Attanasio, J. and E.J. Wherry, *Costimulatory and Coinhibitory Receptor Pathways in Infectious Disease*. Immunity, 2016. **44**(5): p. 1052-68.
33. Baumeister, S.H., et al., *Coinhibitory Pathways in Immunotherapy for Cancer*. Annu Rev Immunol, 2016. **34**: p. 539-73.
34. Dong, H., et al., *B7-H1, a third member of the B7 family, co-stimulates T-cell proliferation and interleukin-10 secretion*. Nat Med, 1999. **5**(12): p. 1365-9.
35. Freeman, G.J., et al., *Engagement of the PD-1 immunoinhibitory receptor by a novel B7 family member leads to negative regulation of lymphocyte activation*. J Exp Med, 2000. **192**(7): p. 1027-34.
36. Yamazaki, T., et al., *Expression of programmed death 1 ligands by murine T cells and APC*. J Immunol, 2002. **169**(10): p. 5538-45.
37. Dong, H., et al., *Tumor-associated B7-H1 promotes T-cell apoptosis: a potential mechanism of immune evasion*. Nat Med, 2002. **8**(8): p. 793-800.
38. Latchman, Y., et al., *PD-L2 is a second ligand for PD-1 and inhibits T cell activation*. Nat Immunol, 2001. **2**(3): p. 261-268.
39. Tseng, S.Y., et al., *B7-DC, a new dendritic cell molecule with potent costimulatory properties for T cells*. J Exp Med, 2001. **193**(7): p. 839-46.
40. Nishimura, H., et al., *Development of lupus-like autoimmune diseases by disruption of the PD-1 gene encoding an ITIM motif-carrying immunoreceptor*. Immunity, 1999. **11**(2): p. 141-51.
41. Nishimura, H., et al., *Autoimmune dilated cardiomyopathy in PD-1 receptor-deficient mice*. Science, 2001. **291**(5502): p. 319-22.
42. Okazaki, T. and T. Honjo, *PD-1 and PD-1 ligands: from discovery to clinical application*. Int Immunol, 2007. **19**(7): p. 813-24.

43. Tamura, H., et al., *B7-H1 costimulation preferentially enhances CD28-independent T-helper cell function*. *Blood*, 2001. **97**(6): p. 1809-16.
44. Liu, X., et al., *B7DC/PDL2 promotes tumor immunity by a PD-1-independent mechanism*. *J Exp Med*, 2003. **197**(12): p. 1721-30.
45. Shin, T., et al., *Cooperative B7-1/2 (CD80/CD86) and B7-DC costimulation of CD4+ T cells independent of the PD-1 receptor*. *J Exp Med*, 2003. **198**(1): p. 31-8.
46. Karwacz, K., et al., *PD-L1 co-stimulation contributes to ligand-induced T cell receptor down-modulation on CD8+ T cells*. *EMBO Mol Med*, 2011. **3**(10): p. 581-92.
47. Xu, D., et al., *A potential new pathway for PD-L1 costimulation of the CD8-T cell response to Listeria monocytogenes infection*. *PLoS One*, 2013. **8**(2): p. e56539.
48. Wang, S., et al., *Molecular modeling and functional mapping of B7-H1 and B7-DC uncouple costimulatory function from PD-1 interaction*. *J Exp Med*, 2003. **197**(9): p. 1083-91.
49. Chen, L., *Co-inhibitory molecules of the B7-CD28 family in the control of T-cell immunity*. *Nat Rev Immunol*, 2004. **4**(5): p. 336-47.
50. Day, C.L., et al., *PD-1 expression on HIV-specific T cells is associated with T-cell exhaustion and disease progression*. *Nature*, 2006. **443**(7109): p. 350-4.
51. Grakoui, A., et al., *Turning on the off switch: regulation of anti-viral T cell responses in the liver by the PD-1/PD-L1 pathway*. *J Hepatol*, 2006. **45**(4): p. 468-72.
52. Petrovas, C., et al., *PD-1 is a regulator of virus-specific CD8+ T cell survival in HIV infection*. *J Exp Med*, 2006. **203**(10): p. 2281-92.
53. Trautmann, L., et al., *Upregulation of PD-1 expression on HIV-specific CD8+ T cells leads to reversible immune dysfunction*. *Nat Med*, 2006. **12**(10): p. 1198-202.
54. Golden-Mason, L., et al., *Upregulation of PD-1 Expression on Circulating and Intrahepatic Hepatitis C Virus-Specific CD8+ T Cells Associated with Reversible Immune Dysfunction*. *Journal of Virology*, 2007. **81**(17): p. 9249-9258.
55. Radziewicz, H., et al., *Liver-Infiltrating Lymphocytes in Chronic Human Hepatitis C Virus Infection Display an Exhausted Phenotype with High Levels of PD-1 and Low Levels of CD127 Expression*. *Journal of Virology*, 2007. **81**(6): p. 2545-2553.
56. Wherry, E.J., *T cell exhaustion*. *Nat Immunol*, 2011. **12**(6): p. 492-9.

57. Wherry, E.J. and M. Kurachi, *Molecular and cellular insights into T cell exhaustion*. Nat Rev Immunol, 2015. **15**(8): p. 486-99.
58. Callahan, M.K., M.A. Postow, and J.D. Wolchok, *Targeting T Cell Co-receptors for Cancer Therapy*. Immunity, 2016. **44**(5): p. 1069-78.
59. Jin, H.T., R. Ahmed, and T. Okazaki, *Role of PD-1 in regulating T-cell immunity*. Curr Top Microbiol Immunol, 2011. **350**: p. 17-37.
60. Tumeh, P.C., et al., *PD-1 blockade induces responses by inhibiting adaptive immune resistance*. Nature, 2014. **515**(7528): p. 568-71.
61. Dahan, R., et al., *FcγR3 Modulate the Anti-tumor Activity of Antibodies Targeting the PD-1/PD-L1 Axis*. Cancer Cell, 2015. **28**(3): p. 285-95.
62. Wang, L., et al., *Programmed death 1 ligand signaling regulates the generation of adaptive Foxp3+CD4+ regulatory T cells*. Proc Natl Acad Sci U S A, 2008. **105**(27): p. 9331-6.
63. Francisco, L.M., et al., *PD-L1 regulates the development, maintenance, and function of induced regulatory T cells*. J Exp Med, 2009. **206**(13): p. 3015-29.
64. Park, H.J., et al., *PD-1 upregulated on regulatory T cells during chronic virus infection enhances the suppression of CD8+ T cell immune response via the interaction with PD-L1 expressed on CD8+ T cells*. J Immunol, 2015. **194**(12): p. 5801-11.
65. Crotty, S., *Follicular helper CD4 T cells (TFH)*. Annu Rev Immunol, 2011. **29**: p. 621-63.
66. Baruch, K., et al., *PD-1 immune checkpoint blockade reduces pathology and improves memory in mouse models of Alzheimer's disease*. Nat Med, 2016. **22**(2): p. 135-7.
67. Chemnitz, J.M., et al., *SHP-1 and SHP-2 associate with immunoreceptor tyrosine-based switch motif of programmed death 1 upon primary human T cell stimulation, but only receptor ligation prevents T cell activation*. J Immunol, 2004. **173**(2): p. 945-54.
68. Sheppard, K.A., et al., *PD-1 inhibits T-cell receptor induced phosphorylation of the ZAP70/CD3zeta signalosome and downstream signaling to PKCθ*. FEBS Lett, 2004. **574**(1-3): p. 37-41.
69. Yokosuka, T., et al., *Programmed cell death 1 forms negative costimulatory microclusters that directly inhibit T cell receptor signaling by recruiting phosphatase SHP2*. J Exp Med, 2012. **209**(6): p. 1201-17.

70. Parry, R.V., et al., *CTLA-4 and PD-1 receptors inhibit T-cell activation by distinct mechanisms*. Mol Cell Biol, 2005. **25**(21): p. 9543-53.
71. Patsoukis, N., et al., *Selective effects of PD-1 on Akt and Ras pathways regulate molecular components of the cell cycle and inhibit T cell proliferation*. Sci Signal, 2012. **5**(230): p. ra46.
72. Fife, B.T., et al., *Interactions between PD-1 and PD-L1 promote tolerance by blocking the TCR-induced stop signal*. Nat Immunol, 2009. **10**(11): p. 1185-92.
73. Honda, T., et al., *Tuning of antigen sensitivity by T cell receptor-dependent negative feedback controls T cell effector function in inflamed tissues*. Immunity, 2014. **40**(2): p. 235-47.
74. Patsoukis, N., et al., *PD-1 alters T-cell metabolic reprogramming by inhibiting glycolysis and promoting lipolysis and fatty acid oxidation*. Nat Commun, 2015. **6**: p. 6692.
75. Wei, F., et al., *Strength of PD-1 signaling differentially affects T-cell effector functions*. Proc Natl Acad Sci U S A, 2013. **110**(27): p. E2480-9.
76. Zhang, X., et al., *Structural and functional analysis of the costimulatory receptor programmed death-1*. Immunity, 2004. **20**(3): p. 337-47.
77. Stamper, C.C., et al., *Crystal structure of the B7-1/CTLA-4 complex that inhibits human immune responses*. Nature, 2001. **410**(6828): p. 608-11.
78. Zak, K.M., et al., *Structure of the Complex of Human Programmed Death 1, PD-1, and Its Ligand PD-L1*. Structure, 2015. **23**(12): p. 2341-8.
79. Youngnak, P., et al., *Differential binding properties of B7-H1 and B7-DC to programmed death-1*. Biochemical and Biophysical Research Communications, 2003. **307**(3): p. 672-677.
80. Butte, M.J., et al., *Interaction of human PD-L1 and B7-1*. Mol Immunol, 2008. **45**(13): p. 3567-72.
81. Ghiotto, M., et al., *PD-L1 and PD-L2 differ in their molecular mechanisms of interaction with PD-1*. Int Immunol, 2010. **22**(8): p. 651-60.
82. Butte, M.J., et al., *Programmed death-1 ligand 1 interacts specifically with the B7-1 costimulatory molecule to inhibit T cell responses*. Immunity, 2007. **27**(1): p. 111-22.
83. van der Merwe, P.A., et al., *CD80 (B7-1) binds both CD28 and CTLA-4 with a low affinity and very fast kinetics*. J Exp Med, 1997. **185**(3): p. 393-403.

84. Park, J.J., et al., *B7-H1/CD80 interaction is required for the induction and maintenance of peripheral T-cell tolerance*. *Blood*, 2010. **116**(8): p. 1291-8.
85. Paterson, A.M., et al., *The programmed death-1 ligand 1:B7-1 pathway restrains diabetogenic effector T cells in vivo*. *J Immunol*, 2011. **187**(3): p. 1097-105.
86. Xiao, Y., et al., *RGMB is a novel binding partner for PD-L2 and its engagement with PD-L2 promotes respiratory tolerance*. *J Exp Med*, 2014.
87. Gupta, G.S., *Animal Lectins: Form, Function and Clinical Applications*.
88. Byrd, J.C., et al., *Dimerization of the insulin-like growth factor II/mannose 6-phosphate receptor*. *J Biol Chem*, 2000. **275**(25): p. 18647-56.
89. Kreiling, J.L., J.C. Byrd, and R.G. MacDonald, *Domain interactions of the mannose 6-phosphate/insulin-like growth factor II receptor*. *J Biol Chem*, 2005. **280**(22): p. 21067-77.
90. Gary-Bobo, M., et al., *Mannose 6-phosphate receptor targeting and its applications in human diseases*. *Curr Med Chem*, 2007. **14**(28): p. 2945-53.
91. Brown, W.J. and M.G. Farquhar, *The distribution of 215-kilodalton mannose 6-phosphate receptors within cis (heavy) and trans (light) Golgi subfractions varies in different cell types*. *Proc Natl Acad Sci U S A*, 1987. **84**(24): p. 9001-5.
92. Roberts, D.L., et al., *Molecular basis of lysosomal enzyme recognition: three-dimensional structure of the cation-dependent mannose 6-phosphate receptor*. *Cell*, 1998. **93**(4): p. 639-48.
93. Coutinho, M.F., M.J. Prata, and S. Alves, *Mannose-6-phosphate pathway: a review on its role in lysosomal function and dysfunction*. *Mol Genet Metab*, 2012. **105**(4): p. 542-50.
94. Brown, J., et al., *Structure and functional analysis of the IGF-II/IGF2R interaction*. *EMBO J*, 2008. **27**(1): p. 265-76.
95. Brown, J., E.Y. Jones, and B.E. Forbes, *Keeping IGF-II under control: lessons from the IGF-II-IGF2R crystal structure*. *Trends Biochem Sci*, 2009. **34**(12): p. 612-9.
96. Nishimoto, I., et al., *Possible direct linkage of insulin-like growth factor-II receptor with guanine nucleotide-binding proteins*. *J Biol Chem*, 1989. **264**(24): p. 14029-38.
97. Murayama, Y., et al., *Distinctive Regulation of the Functional Linkage between the Human Cation-Independent Mannose 6-Phosphate Receptor and Gtp-Binding Proteins by Insulin-Like Growth Factor-Ii and Mannose 6-Phosphate*. *Journal of Biological Chemistry*, 1990. **265**(29): p. 17456-17462.

98. Okamoto, T., et al., *A simple structure encodes G protein-activating function of the IGF-II/mannose 6-phosphate receptor*. Cell, 1990. **62**(4): p. 709-17.
99. Ikezu, T., et al., *In vivo coupling of insulin-like growth factor II/mannose 6-phosphate receptor to heteromeric G proteins. Distinct roles of cytoplasmic domains and signal sequestration by the receptor*. J Biol Chem, 1995. **270**(49): p. 29224-8.
100. Korner, C., et al., *Mannose 6-phosphate/insulin-like growth factor II receptor fails to interact with G-proteins. Analysis of mutant cytoplasmic receptor domains*. J Biol Chem, 1995. **270**(1): p. 287-95.
101. Purchio, A.F., et al., *Identification of mannose 6-phosphate in two asparagine-linked sugar chains of recombinant transforming growth factor-beta 1 precursor*. J Biol Chem, 1988. **263**(28): p. 14211-5.
102. Dennis, P.A. and D.B. Rifkin, *Cellular activation of latent transforming growth factor beta requires binding to the cation-independent mannose 6-phosphate/insulin-like growth factor type II receptor*. Proc Natl Acad Sci U S A, 1991. **88**(2): p. 580-4.
103. Groskopf, J.C., et al., *Proliferin induces endothelial cell chemotaxis through a G protein-coupled, mitogen-activated protein kinase-dependent pathway*. Endocrinology, 1997. **138**(7): p. 2835-2840.
104. Kang, J.X., et al., *Retinoic acid alters the intracellular trafficking of the mannose-6-phosphate/insulin-like growth factor II receptor and lysosomal enzymes*. Proc Natl Acad Sci U S A, 1998. **95**(23): p. 13687-91.
105. Kang, J.X., Y. Li, and A. Leaf, *Mannose-6-phosphate/insulin-like growth factor-II receptor is a novel receptor for retinoic acid*. Faseb Journal, 1998. **12**(4): p. A433-A433.
106. Kang, J.X., et al., *Mannose 6-phosphate/insulin-like growth factor II receptor mediates the growth-inhibitory effects of retinoids*. Cell Growth Differ, 1999. **10**(8): p. 591-600.
107. Pfisterer, K., et al., *The late endosomal transporter CD222 directs the spatial distribution and activity of Lck*. J Immunol, 2014. **193**(6): p. 2718-32.
108. Ikushima, H., et al., *Internalization of CD26 by mannose 6-phosphate/insulin-like growth factor II receptor contributes to T cell activation*. Proc Natl Acad Sci U S A, 2000. **97**(15): p. 8439-44.
109. Ahmed, K.A., et al., *Differential expression of mannose-6-phosphate receptor regulates T cell contraction*. J Leukoc Biol, 2015. **98**(3): p. 313-8.

110. Motyka, B., et al., *Mannose 6-Phosphate/Insulin-like Growth Factor II Receptor Is a Death Receptor for Granzyme B during Cytotoxic T Cell–Induced Apoptosis*. *Cell*, 2000. **103**(3): p. 491-500.
111. Davis, S.J., et al., *High level expression in Chinese hamster ovary cells of soluble forms of CD4 T lymphocyte glycoprotein including glycosylation variants*. *J Biol Chem*, 1990. **265**(18): p. 10410-8.
112. Collins, A.V., et al., *The interaction properties of costimulatory molecules revisited*. *Immunity*, 2002. **17**(2): p. 201-10.
113. Chesla, S.E., P. Selvaraj, and C. Zhu, *Measuring Two-Dimensional Receptor-Ligand Binding Kinetics by Micropipette*. *Biophysical Journal*, 1998. **75**(3): p. 1553-1572.
114. Chen, W., et al., *Measuring Receptor-Ligand Binding Kinetics on Cell Surfaces: From Adhesion Frequency to Thermal Fluctuation Methods*. *Cell Mol Bioeng*, 2008. **1**(4): p. 276-288.
115. Liu, B., et al., *Accumulation of Dynamic Catch Bonds between TCR and Agonist Peptide-MHC Triggers T Cell Signaling*. *Cell*, 2014. **157**(2): p. 357-68.
116. Williams, T.E., P. Selvaraj, and C. Zhu, *Concurrent Binding to Multiple Ligands: Kinetic Rates of CD16b for Membrane-Bound IgG1 and IgG2*. *Biophysical Journal*, 2000. **79**(4): p. 1858-1866.
117. Zhu, C. and T.E. Williams, *Modeling Concurrent Binding of Multiple Molecular Species in Cell Adhesion*. *Biophysical Journal*, 2000. **79**(4): p. 1850-1857.
118. Liu, B., et al., *The cellular environment regulates in situ kinetics of T-cell receptor interaction with peptide major histocompatibility complex*. *Eur J Immunol*, 2015. **45**(7): p. 2099-110.
119. Hong, J., et al., *Force-Regulated In Situ TCR-Peptide-Bound MHC Class II Kinetics Determine Functions of CD4+ T Cells*. *J Immunol*, 2015. **195**(8): p. 3557-64.
120. Huppa, J.B., et al., *TCR-peptide-MHC interactions in situ show accelerated kinetics and increased affinity*. *Nature*, 2010. **463**(7283): p. 963-7.
121. Adams, J.J., et al., *T cell receptor signaling is limited by docking geometry to peptide-major histocompatibility complex*. *Immunity*, 2011. **35**(5): p. 681-93.
122. Zhang, F., et al., *Two-dimensional Kinetics Regulation of $\alpha(L)\beta(2)$ -ICAM-1 Interaction by Conformational Changes of the $\alpha(L)$ -Inserted Domain*. *The Journal of biological chemistry*, 2005. **280**(51): p. 42207-42218.

123. Chen, W., et al., *Monitoring receptor-ligand interactions between surfaces by thermal fluctuations*. Biophys J, 2008. **94**(2): p. 694-701.
124. Bhatia, S., et al., *Different cell surface oligomeric states of B7-1 and B7-2: implications for signaling*. Proc Natl Acad Sci U S A, 2005. **102**(43): p. 15569-74.
125. Bhatia, S., et al., *Dynamic equilibrium of B7-1 dimers and monomers differentially affects immunological synapse formation and T cell activation in response to TCR/CD28 stimulation*. J Immunol, 2010. **184**(4): p. 1821-8.
126. Zhang, Y., et al., *P-selectin glycoprotein ligand-1 forms dimeric interactions with E-selectin but monomeric interactions with L-selectin on cell surfaces*. PLoS One, 2013. **8**(2): p. e57202.
127. Ikemizu, S., et al., *Structure and dimerization of a soluble form of B7-1*. Immunity, 2000. **12**(1): p. 51-60.
128. Bell, G.I., M. Dembo, and P. Bongrand, *Cell adhesion. Competition between nonspecific repulsion and specific bonding*. Biophys J, 1984. **45**(6): p. 1051-64.
129. Luescher, I.F., et al., *CD8 Modulation of T-Cell Antigen Receptor-Ligand Interactions on Living Cytotoxic T-Lymphocytes*. Nature, 1995. **373**(6512): p. 353-356.
130. Liu, B., W. Chen, and C. Zhu, *Molecular force spectroscopy on cells*. Annu Rev Phys Chem, 2015. **66**: p. 427-51.
131. Arcaro, A., et al., *CD8 beta endows CD8 with efficient coreceptor function by coupling T cell receptor/CD3 to raft-associated CD8/p56(lck) complexes*. Journal of Experimental Medicine, 2001. **194**(10): p. 1485-1495.
132. Zinselmeyer, B.H., et al., *PD-1 promotes immune exhaustion by inducing antiviral T cell motility paralysis*. J Exp Med, 2013. **210**(4): p. 757-74.
133. Yokosuka, T., et al., *Newly generated T cell receptor microclusters initiate and sustain T cell activation by recruitment of Zap70 and SLP-76*. Nat Immunol, 2005. **6**(12): p. 1253-62.
134. Rossy, J., et al., *Conformational states of the kinase Lck regulate clustering in early T cell signaling*. Nat Immunol, 2013. **14**(1): p. 82-9.
135. Carter, L., et al., *PD-1:PD-L inhibitory pathway affects both CD4(+) and CD8(+) T cells and is overcome by IL-2*. Eur J Immunol, 2002. **32**(3): p. 634-43.
136. Iwai, Y., et al., *PD-1 inhibits antiviral immunity at the effector phase in the liver*. J Exp Med, 2003. **198**(1): p. 39-50.

137. Flies, D.B., et al., *Cutting edge: A monoclonal antibody specific for the programmed death-1 homolog prevents graft-versus-host disease in mouse models*. J Immunol, 2011. **187**(4): p. 1537-41.
138. Wang, L., et al., *VISTA, a novel mouse Ig superfamily ligand that negatively regulates T cell responses*. J Exp Med, 2011. **208**(3): p. 577-92.
139. Ghosh, P., N.M. Dahms, and S. Kornfeld, *Mannose 6-phosphate receptors: new twists in the tale*. Nat Rev Mol Cell Biol, 2003. **4**(3): p. 202-12.
140. Hindmarsh, E.J., et al., *Cell surface expression of the 300 kDa mannose-6-phosphate receptor by activated T lymphocytes*. Immunol Cell Biol, 2001. **79**(5): p. 436-43.
141. Meresse, S. and B. Hoflack, *Phosphorylation of the cation-independent mannose 6-phosphate receptor is closely associated with its exit from the trans-Golgi network*. J Cell Biol, 1993. **120**(1): p. 67-75.
142. Rosorius, O., et al., *Characterization of phosphorylation sites in the cytoplasmic domain of the 300 kDa mannose-6-phosphate receptor*. Biochem J, 1993. **292** (Pt 3): p. 833-8.
143. van der Merwe, P.A. and O. Dushek, *Mechanisms for T cell receptor triggering*. Nat Rev Immunol, 2011. **11**(1): p. 47-55.
144. Das, D.K., et al., *Force-dependent transition in the T-cell receptor beta-subunit allosterically regulates peptide discrimination and pMHC bond lifetime*. Proc Natl Acad Sci U S A, 2015. **112**(5): p. 1517-22.
145. Kim, S.T., et al., *The alphabeta T cell receptor is an anisotropic mechanosensor*. J Biol Chem, 2009. **284**(45): p. 31028-37.
146. Hu, K.H. and M.J. Butte, *T cell activation requires force generation*. J Cell Biol, 2016. **213**(5): p. 535-42.
147. Basu, R., et al., *Cytotoxic T Cells Use Mechanical Force to Potentiate Target Cell Killing*. Cell, 2016. **165**(1): p. 100-10.
148. Doucey, M.A., et al., *CD3 delta establishes a functional link between the T cell receptor and CD8*. J Biol Chem, 2003. **278**(5): p. 3257-64.
149. Mallaun, M., et al., *The T Cell Receptor's -Chain Connecting Peptide Motif Promotes Close Approximation of the CD8 Coreceptor Allowing Efficient Signal Initiation*. The Journal of Immunology, 2008. **180**(12): p. 8211-8221.
150. Au-Yeung, B.B., et al., *A genetically selective inhibitor demonstrates a function for the kinase Zap70 in regulatory T cells independent of its catalytic activity*. Nat Immunol, 2010. **11**(12): p. 1085-92.

151. Legge, J., *The I ching*. 2d ed. The Sacred books of the East., 1899, New York,: Dover Publications. xxi, 448 p.